

CHEMICAL EVOLUTION LIBRARY FOR GALAXY FORMATION SIMULATION

TAKAYUKI R. SAITOH¹
Draft version July 27, 2018

ABSTRACT

We have developed a software library for chemical evolution simulations of galaxy formation under the simple stellar population (SSP) approximation. In this library, all of the necessary components concerning chemical evolution, such as initial mass functions, stellar lifetimes, yields from type II and Ia supernovae, asymptotic giant branch stars, and neutron star mergers, are compiled from the literature. Various models are pre-implemented in this library so that users can choose their favorite combination of models. Subroutines of this library return released energy and masses of individual elements depending on a given event type. Since the redistribution manner of these quantities depends on the implementation of users' simulation codes, this library leaves it up to the simulation code. As demonstrations, we carry out both one-zone, closed box simulations and three-dimensional simulations of a collapsing gas and dark matter system using this library. In these simulations, we can easily compare the impact of individual models on the chemical evolution of galaxies, just by changing the control flags and parameters of the library. Since this library only deals with the part of chemical evolution under the SSP approximation, any simulation codes that use the SSP approximation – namely particle-base and mesh codes, as well as semi-analytical models – can use it. This library is named “CELlib” after the term “Chemical Evolution Library” and is made available to the community.

Subject headings: galaxies:evolution—galaxies:ISM—methods:numerical

1. INTRODUCTION

Our Universe starts with hydrogen (H), helium (He) and a small amount of Lithium (Li). These elements are synthesized during the Big Bang and all the other elements equal to or heavier than carbon (C) are synthesized in stars and during supernovae. In astrophysics, the history of heavy element generation via the nucleosynthesis in stars and succeeding pollution of the interstellar medium (ISM) are expressed as “chemical evolution”.

During stellar evolution, nucleosynthesis progresses from H to iron (Fe) where the final products depend on the mass of a star. The massive stars heavier than $8 M_{\odot}$ are thought to explode as type II supernovae (hereafter SNe II). In this phase, heavy elements ($> \text{Fe}$) are synthesized. If a star is not so massive, say $\leq 8 M_{\odot}$, it experiences an asymptotic giant branch (AGB) phase after the main sequence phase. During the AGB phase, the neutron capture process takes place with a slow speed (slow means that the timescale of the β decay, τ_{β} , is comparable to that of the neutron capture, τ_n). This slow process (*s*-process) generates elements heavier than Fe efficiently. In addition, a part of the intermediate mass stars' binary systems is thought to explode as a type Ia SNe (hereafter SNe Ia). SNe Ia are triggered by the Roche-lobe overflows or the final coalescences of binary systems. In the former situation, one of the progenitor star in a binary is a degenerated star and, in the latter, both are degenerated stars. Thus, these two scenarios are called single-degenerate or double-degenerate scenarios (Whelan & Iben 1973; Nomoto 1982; Iben & Tutukov 1984; Webbink 1984). Again, heavier elements are synthesized, such as Fe and nickel (Ni). Numerical studies tell us that neu-

tron star-neutron star mergers (NSMs) could be a possible site of *r*-process ($\tau_{\beta} \gg \tau_n$) elements, in particular, the heavier *r*-process elements (e.g., Freiburghaus et al. 1999; Goriely et al. 2011; Wanajo et al. 2014).

Each process has its own characteristic time-scale and abundance pattern. Thus, they work as the chronometer for the formation history of the galactic stellar system. For instance, in an early phase ($< 10^8$ yr), the chemical evolution progresses mainly through the pollution by SNe II. With this process, the α elements of which the masses are multiples of He, such as oxygen (O), magnesium (Mg), silicon (Si), and calcium (Ca), are ejected to the interstellar medium (ISM). On the other hand, in SNe Ia, Fe, and Ni are efficiently released to the ISM. The combination of these events makes the observed features of the plateau (flat part) of the $[\alpha/\text{Fe}]$ as a function of $[\text{Fe}/\text{H}]^2$ in a low metallicity part, and causes the distribution of $[\alpha/\text{Fe}]$ as a function of $[\text{Fe}/\text{H}]$ (e.g., Tinsley 1980). The flat part represents the abundance pattern of SNe II. The decreasing part is composed of the mixture of SNe II and SNe Ia where the contribution of SNe II is gradually decreasing, reflecting its time-scale, and that of SNe Ia is gradually increasing. The breaking point of the flat part reflects the time scale of the enrichment of the chemical composition in the ISM. The breaking point is $[\text{Fe}/\text{H}] = -1 \sim -0.5$ in the Milky Way galaxy (e.g., Hayden et al. 2015), whereas it is much lower in the local dwarf galaxies (e.g., Tolstoy et al. 2009). AGBs do not mainly contribute to the distributions of $[\alpha/\text{Fe}]$ - $[\text{Fe}/\text{H}]$ relations while they can contribute rather low mass elements such as C and nitrogen (N).

There are many galactic surveys which resolve the chemical compositions and kinematic information of a lot of stars, e.g., RAVE (Steinmetz et al. 2006), APOGEE

saitoh@elsi.jp

¹ Earth-Life Science Institute, Tokyo Institute of Technology, 2-12-1, Ookayama, Meguro, Tokyo, 152-8551, Japan

² $[A/B] \equiv \log_{10}(n_A/n_B) - \log_{10}(n_A/n_B)_{\odot}$, where n_A and n_B are the number abundance of element A and B, respectively.

(Majewski et al. 2016), Gaia-ESO (Gilmore et al. 2012), HERMES (GRASH) (De Silva et al. 2015). The data obtained by these surveys can make a strong constraint on the formation and evolution of the Milky Way galaxy and thus, it becomes a clue to understanding the formation and evolution of galaxies in general.

It has been almost a quarter of a century since the first 3-dimensional simulations of galaxy formation, including dark matter and baryon. The first galaxy formation simulation including chemical evolution was carried out by Steinmetz & Mueller (1994); Steinmetz & Muller (1995). In this simulation, they only solved the evolution of the metallicity Z , the mass fraction of the heavy elements, synthesized by SNe II. Then, Raiteri et al. (1996) introduced both SNe II and Ia. The models have improved further and the current concordance simulations include about 10 elements (e.g., Mosconi et al. 2001; Kawata & Gibson 2003; Scannapieco et al. 2005; Okamoto et al. 2005, 2008; Wiersma et al. 2009b; Kobayashi & Nakasato 2011; Rahimi et al. 2011; Few et al. 2012; Vogelsberger et al. 2013; Brook et al. 2014; Few et al. 2014; Snaith et al. 2016), as well as the mixing of them in the ISM (Greif et al. 2009; Shen et al. 2010). Semi-analytical models are also considered, in which various elements are released from different feedback models (e.g., Nagashima et al. 2005; Cora 2006; Arrighi et al. 2010; Yates et al. 2013; Gargiulo et al. 2015). Unlike solving the evolution of individual stars, simulations of galaxy formation use a simple stellar populations (SSP) approximation, where star particles consist of a cluster of stars sharing the same age and metallicity, and whose mass function follows a certain initial mass function (hereafter IMF).

In order to solve chemical evolution, the amount of newly synthesized elements in stars, “yields”, and the return mass fraction of SSP particles are necessary. These data are obtained from the studies of stellar evolution and explosions. There are flexibilities to choose yields tables as well as the functional forms of IMF and its mass range. The most popular yields for SNe II are Woosley & Weaver (1995) and its improved version supplied by Portinari et al. (1998). For SNe Ia, the yields of Nomoto et al. (1997) and its updated version given by Iwamoto et al. (1999) are well-used. For AGBs, the yields tables of van den Hoek & Groenewegen (1997), Portinari et al. (1998), and Marigo (2001) are widely used. The combinations of yields tables can lead to different chemical abundance patterns and thus it is intensively studied (e.g., François et al. 2004; Wiersma et al. 2009b; Romano et al. 2010; Few et al. 2012).

It is pointed out by the galactic chemical evolution model of Timmes et al. (1995) that the Fe yields of Woosley & Weaver (1995) are slightly large in order to obtain good agreement with observations.³ Usually the Fe yield is reduced by a factor of 2 from the original values (e.g., Timmes et al. 1995; Gibson 1997; Gibson et al. 1997). The yields tables of Portinari et al. (1998), which

is an extended version of Woosley & Weaver (1995), also have the same problem. Sometimes ad hoc modifications are used to halve the yield of Fe and double those of Mg and C in order to fit the observations (see Wiersma et al. 2009b). Since these yield tables are widely used in simulations of galaxy formation, these modifications are commonly used.

An essential solution to solve this problem is to update the yields tables following the progress of stellar evolution models and reaction rates. However, it might be difficult to update yields tables frequently since, in simulation code, the chemical evolution part is deeply connected to them. Moreover, the size and range of mass and metallicity grids of the yields tables are generally different from each other. This inhibits the smooth replacement of yields tables, although it is a theoretically straightforward task.

If the chemical evolution part is implemented separately in a software library which can be linked from simulation codes directly and it has clearly defined application interfaces (APIs), the chemical evolution part is developed independently and it becomes easy to take the latest models. Insofar as we know, such software library does not exist.

There are several softwares which can generate stellar yields tables. `Starburst99`⁴ is a widely-used software to model spectrophotometric properties of star-forming galaxies (Leitherer et al. 1999; Vázquez & Leitherer 2005; Leitherer et al. 2010, 2014). This software contains a huge database of stellar evolutions and thus, it can output yields. Since this software is not designed to link from other codes, it is necessary to pre-generate a yields table if one uses it in one’s simulation code. Thus, when parameters change, e.g., the functional form and the mass range of IMF, the reconstruction of the yields table is necessary. The NuGrid collaboration⁵ has developed a Python code, `SYGMA`, which can deal with the yields of the NuGrid project and can be used in chemical evolution of galaxies (Côté et al. 2016). Since this is implemented as an iPython notebook, users need to pre-generate yields in order to use the outcomes from `SYGMA`.

The aim of this paper is to describe a software library which deals with chemical evolution via APIs and to demonstrate the capability of this library. This library is named “`CELib`” after the term “Chemical Evolution Library”. Since the primary purpose of this library is to use it with simulation codes of galaxy formation, this library works under the SSP approximation. Note that its main function is to return yields (and energy) of various feedback types from SSP particles. Redistribution of these quantities is not within its scope because there are a number of redistribution manners and the implementation of them is deeply coupled with simulation codes. Models and parameters of this library are selectable at the runtime and the IMF weighted yields are automatically generated in the initialization process.

`CELib` is an open-source software library and is released under the MIT license. The whole source codes including some examples are distributed through the following website: <https://bitbucket.org/tsaitoh/celib>. A

³ Nomoto et al. (2013) summarized the problems of Portinari et al. (1998)’s yields tables as (1) the Fe yield is overestimated, (2) the mass loss affects the final C+O core structure, but they ignored the evolution effects, (3) the Mg yield with a mass of $40 M_{\odot}$ is too small.

⁴ <http://www.stsci.edu/science/starburst99/>

⁵ <http://nugridstars.org/>

documentation is also available in this site.

The structure of this paper is as follows. First, we briefly describe the design concept of this library in §2. Then we describe the notations and definitions in §3 and we introduce components which this library consists of in §4. The reference feedback models of SNe II/Ia, AGBs and NSMs are described in §5. In §6, we explain our implementation of this library. In §7, we show the results of the simple one-zone model and galaxy simulation using this library. Finally, we provide the summary in §8.

2. DESIGN CONCEPT

The key concepts of the design of CELib are as follows.

- CELib returns yields and energy from SSP particles, based on the adopted IMF and yields tables. All returned quantities are IMF weighted ones. Useful data, such as the functional form of IMF and stellar lifetimes, are also implemented.
- CELib supplies reference feedback models of SNe II/Ia, AGBs and NSMs. Reference feedback models can provide the event time and the amount of released mass, metal and energy. A redistribution manner of these quantities is outside its scope.
- The functional form of the IMF, its mass ranges, yields tables, etc. are changed by using control flags and parameters. All changes of flags and parameters are reflected when the initializer of CELib is called.
- All communication between a user simulation code and CELib is carried out through CELib APIs.

Figure 1 shows the schematic picture of the relation between a user’s simulation code and CELib. The simulation code deals with the time integration of a system solving gravitational interactions among DM, gas, and star (SSP) particles and hydrodynamics, involving baryon physics such as radiative cooling/heating, star formation, and feedbacks. CELib is responsible for the chemical evolution part. Event time, released energy and ejected metals are evaluated when the simulation code sends data of an SSP particle to CELib via APIs. What the simulation code needs to do is to add the released energy and the ejected metals to the surrounding ISM and to reduce the mass of the SSP particle so that the mass is conserved.

3. NOTATIONS AND DEFINITIONS

Before explaining details of CELib, we need to confirm the notations and what quantities are used and obtained by using the library. We describe them in this section.

The primary purpose of this library is to calculate the stellar yields from various evolution phases of stars under the SSP approximation. The stellar yield, the ejected mass of the i -th element from a star whose mass is m , is expressed as

$$Y_i(m) = y_i(m) + Z_i^0 m_{\text{ej}}(m), \quad (1)$$

where $y_i(m)$ is the *net yield* which represents that the newly synthesized mass of i -th element, Z_i^0 is the metallicity of the i -th element originally presented in the progenitor star and $m_{\text{ej}}(m)$ is the total ejecta mass of the

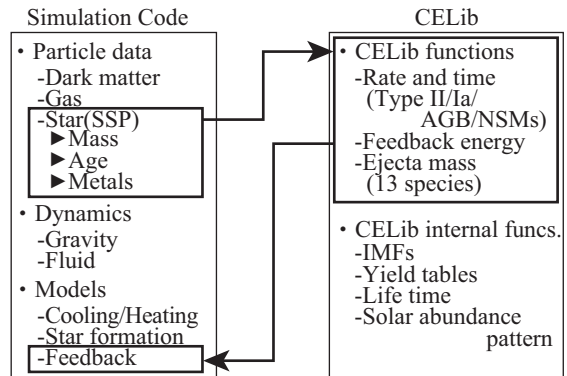


FIG. 1.— Relation between a user’s simulation code and this chemical evolution library, CELib. The left rectangular box with the thin line represents the simulation code. It has particles data, functions which evaluate dynamical interactions, and models for the baryon physics. The right rectangular box with the thin line is CELib. CELib consists of functions for chemical evolution and they can use via APIs. For instance, when an SSP particle is born in the simulation code, it asks CELib to get the time of SNe II. When the SSP particle reaches the event epoch, the simulation code sends information regarding the SSP particles and gets the amount of released energy and ejected metals of 13 elements. When these event times come, the code again sends information of the SSP particle in order to obtain feedback results. The procedures of feedback from SNe Ia, AGB and NSMs are identical.

star. This quantity, $Y_i(m)$, is always larger than or equal to zero. The total ejecta mass is

$$m_{\text{ej}}(m) = m - m_{\text{rem}}(m), \quad (2)$$

where $m_{\text{rem}}(m)$ is the remnant mass of a star whose mass is m .

It is essential to use the net yields for the study of the galactic chemical evolution. Rearranging Eq. (1), we can obtain

$$y_i(m) = Y_i(m) - Z_i^0 m_{\text{ej}}(m). \quad (3)$$

We gather this quantity from the literature. However, some studies provide not $y_i(m)$ but $Y_i(m)$ or $Y_i(m) - m_{\text{sw},i}(m)$ where $m_{\text{sw},i}(m)$ is the ejected mass of the i -th element via stellar winds. In such cases, we reconstruct y carefully with several reasonable assumptions. This quantity can be positive and negative, unlike the stellar yield Y . We use y for SNe II and AGBs, whereas we adopt Y for SNe Ia and NSMs.

Since this library is used under the SSP approximation, the IMF weighted yield is useful. Here, we use

$$p_i(m_L < m < m_U) = \int_{m_L}^{m_U} y_i(m) \frac{\xi(\log_{10} m)}{m} dm, \quad (4)$$

where $\xi(\log_{10} m)$ is the IMF function (see below for the concrete functional forms). With this quantity and the return mass fraction,

$$E_{\text{ret}}(m_L < m < m_U) = \int_{m_L}^{m_U} m_{\text{ej}}(m) \frac{\xi(\log_{10} m)}{m} dm, \quad (5)$$

we can evaluate the yield of an SSP particle as

$$E_i(m_L < m < m_U) = p_i(m_L < m < m_U) + Z_i^0 E_{\text{ret}}(m_L < m < m_U). \quad (6)$$

By multiplying the mass of the SSP particle to Eq. (6), we can obtain the amount of the released mass of i -th

element from a feedback event.

The IMF weighted released amount of energy from massive stars can be evaluated by the following equation:

$$E_{\text{en}}(m_{\text{L}} < m < m_{\text{U}}) = \int_{m_{\text{L}}}^{m_{\text{U}}} e_{\text{en}}(m) \frac{\xi(\log_{10} m)}{m} dm, \quad (7)$$

where, $e_{\text{en}}(m)$ is the released energy from a star whose mass is m .

Strictly speaking, the released mass of i -th element changes depending on the amount of the other elements. The Q_{ij} formulation (Talbot & Arnett 1973; Ferrini et al. 1992) is known as a model which considers the effect of the change in amounts of other elements. We do not implement the Q_{ij} formulation here in CELib, for simplicity.

4. COMPONENTS

In this section, we describe key components of CELib. IMFs which are pre-implemented are shown in §4.1. The metallicity dependent stellar lifetimes are explained in §4.2. Then, thirteen elements in CELib are explained in §4.3. Yields for SNe II/Ia, AGBs and NSMs are described in §4.4, §4.5, §4.6, and §4.7, respectively. Released energy and return mass from an SSP particle with various IMFs are summarized in §4.8. In §4.9, the implemented solar abundance patterns are shown.

4.1. Selectable IMFs in this library

CELib pre-implements seven popular IMFs for ordinary population stars (population I/II; hereafter Pop I/II) and users can choose which one to use. Moreover, CELib supports an IMF for population III (hereafter Pop III) stars, which is utilized only for extremely low metal SSPs. CELib does not allow the functional form of the IMF to be changed depending on the situation in a single simulation, except for the case using a Pop III IMF. When the contribution of Pop III stars is adopted, the functional form of the IMF and mass range are changed depending on metallicity.

The definition of the IMF is

$$\xi(\log_{10} m) = \frac{dN}{d \log_{10} m}, \quad (8)$$

where N is the number of stars in a given mass bin ($d \log_{10} m$). The explicit functional forms of the IMF users can choose will be explained below.

The normalization of the IMF is done by the following equation:

$$\int_{m_{\text{IMF,L}}}^{m_{\text{IMF,U}}} \xi(\log_{10} m) dm = 1. \quad (9)$$

Here, $m_{\text{IMF,L}}$ and $m_{\text{IMF,U}}$ are the lower and upper mass boundaries of the IMF. Substituting Eq. (8) into Eq. (9), we have

$$\int_{m_{\text{IMF,L}}}^{m_{\text{IMF,U}}} \xi(\log_{10} m) dm = \int_{m_{\text{IMF,L}}}^{m_{\text{IMF,U}}} \frac{dN}{d \log_{10} m} dm, \quad (10)$$

$$= 1. \quad (11)$$

Thus, the normalization is ‘‘the mass weighted number of stars’’. Because of this definition, the number of stars

per $1 M_{\odot}$ of a given mass range ($m_{\text{L}} < m < m_{\text{U}}$) can be calculated as

$$N = \int_{m_{\text{L}}}^{m_{\text{U}}} \frac{\xi(\log_{10} m)}{m} dm = \int_{m_{\text{L}}}^{m_{\text{U}}} dN. \quad (12)$$

The current version of CELib supports seven well used IMFs for Pop I/II and one IMF for Pop III stars. They are the Salpeter, Diet Salpeter, Miller-Scalo, Kennicutt, Kroupa(2001 & 1993), Chabrier, and Susa IMFs. We describe the functional form of each IMF below.

The Salpeter IMF (Salpeter 1955) is the most fundamental one which has a power law form with a single segment:

$$\xi(\log_{10} m) \propto m^{-1.35} \quad 0.1 M_{\odot} < m < 120 M_{\odot}. \quad (13)$$

The second IMF is the diet Salpeter IMF. The lower part of the IMF is reduced to be a flat profile, whereas the higher part is the same as the original Salpeter IMF. This IMF is originally introduced in order to explain the observed mass-to-light ratio of disk galaxies (Bell & de Jong 2001). The form of the diet Salpeter IMF is

$$\xi(\log_{10} m) \propto \begin{cases} m^0 & 0.1 M_{\odot} < m < 0.6 M_{\odot}, \\ m^{-1.35} & 0.6 M_{\odot} < m < 120 M_{\odot}. \end{cases} \quad (14)$$

The Miller-Scalo IMF (Miller & Scalo 1979) has a power law form with three segments:

$$\xi(\log_{10} m) \propto \begin{cases} m^{-0.4} & 0.1 M_{\odot} < m < 1 M_{\odot}, \\ m^{-1.5} & 1 M_{\odot} < m < 10 M_{\odot}, \\ m^{-2.3} & 10 M_{\odot} < m < 120 M_{\odot}. \end{cases} \quad (15)$$

The high (low) mass end has a deeper (shallower) power index when we compare it with that of the Salpeter IMF.

The functional form of the Kroupa IMF (Kroupa 2001) CELib adopts is as follows:

$$\xi(\log_{10} m) \propto \begin{cases} m^{-0.3} & 0.1 M_{\odot} < m < 0.5 M_{\odot}, \\ m^{-1.3} & 0.5 M_{\odot} < m < 120 M_{\odot}. \end{cases} \quad (16)$$

Note that the minimum mass of a star which is followed by the original form of the Kroupa’s IMF is $0.01 M_{\odot}$, but we do not take them and adopt an IMF greater than $0.1 M_{\odot}$.

In addition to the Kroupa IMF (Kroupa 2001), CELib also has the IMF of Kroupa et al. (1993) (hereafter Kroupa1993 IMF). The functional form of this IMF is

$$\xi(\log_{10} m) \propto \begin{cases} m^{-0.3} & 0.1 M_{\odot} < m < 0.5 M_{\odot}, \\ m^{-1.2} & 0.5 M_{\odot} < m < 1.0 M_{\odot}, \\ m^{-1.7} & 1.0 M_{\odot} < m < 120 M_{\odot}. \end{cases} \quad (17)$$

As is obvious, the slope of this IMF in the mass regime at $> 1 M_{\odot}$ is steeper than that of the Kroupa (2001)’s IMF.

Kennicutt (1983) has provided the IMF with the following form:

$$\xi(\log_{10} m) \propto \begin{cases} m^{-0.4}, & 0.1 M_{\odot} < m < 1 M_{\odot} \\ m^{-1.5}. & 1 M_{\odot} < m < 120 M_{\odot} \end{cases} \quad (18)$$

The final IMF for ordinary populations of stars is the Chabrier IMF (Chabrier 2003). This IMF has a rather complicated form since the lower part of it is expressed by

a log-normal function. The values of the normalization parameters are given by Chabrier (2003). The functional form of the IMF is

$$\xi(\log_{10} m) \propto \begin{cases} m^0 \exp \left\{ -\frac{[\log_{10}(\frac{m}{m_{\text{crit}}})]^2}{2\sigma^2} \right\} & 0.1 M_{\odot} < m < 1 M_{\odot}, \\ m^{-1.3} & 1 M_{\odot} < m < 100 M_{\odot}, \end{cases} \quad (19)$$

where $m_{\text{crit}} = 0.079$ and $\sigma = 0.69$.

For the IMF of Pop III stars, we use the following function:

$$\xi(\log_{10} m) \propto \exp \left\{ -\frac{[\log_{10}(\frac{m}{m_{\text{popIII}}})]^2}{2\sigma_{\text{popIII}}^2} \right\} \quad (20)$$

$$0.7 M_{\odot} < m < 300 M_{\odot},$$

where $m_{\text{popIII}} = 22.0$ and $\sigma_{\text{popIII}} = 0.5$. This functional form is evaluated by using the eye-ball fitting of the mass distribution of Susa et al. (2014) (their figure 9). This IMF is used only when the Pop III mode turns on. It should be noted that there is no consensus on the shape of the Pop III IMF and other researchers obtain different functional forms of Pop III IMFs (e.g., Komiya et al. 2007; Greif et al. 2011; Hirano et al. 2014; Hartwig et al. 2015; Hirano et al. 2015; Fraser et al. 2015; Stacy et al. 2016). It is formally not difficult to extend this library to use other functional forms for Pop III stars.

The normalization coefficient of each IMF for the given mass range is evaluated at the initialization phase of the library following Eq. (9).

The contributions of the lower and upper mass boundaries of Pop I/II IMFs are not crucial for the whole evolution of a system. For the lower mass boundary, we adopted $0.1 M_{\odot}$ for all these IMFs for simplicity. There are some variations, but the contribution of the lower mass limit is almost negligible because of their long lifetimes (see §4.2). For the upper mass boundary, we assumed $100 M_{\odot}$ for the Chabrier IMF and $120 M_{\odot}$ for the others. This difference is, again, negligible, because the contribution of massive stars is insignificant due to steeply decreasing profiles. Note that the lower and upper mass ends of the IMF are changeable from the fiducial ones in this library.

For Pop III stars, we adopt an entirely different mass range, $0.7\text{--}300 M_{\odot}$, reflecting the potential difference in formation of Pop III stars from ordinary stars due to their inherent cooling processes (e.g., Omukai & Nishi 1998; Abel et al. 2002; Bromm et al. 2002; Yoshida et al. 2008; Omukai et al. 2010; Hosokawa et al. 2011; Bromm 2013; Glover 2013; Susa et al. 2014; Hirano et al. 2015).

In figure 2, we compare the shapes of these seven IMFs. For ordinary populations, we can see that stars with masses of $\sim 1 M_{\odot}$ dominate in the six IMFs except for the Salpeter IMF; it has many more low-mass stars. We also find a substantial variation at the high mass end; high mass end Pop I/II stars make the largest contribution in the Chabrier IMF, and the smallest in the Miller-Scalo and Kroupa1993 IMFs. These differences reflect the amount of energy released by SNe II (see §5.1 and table 4).

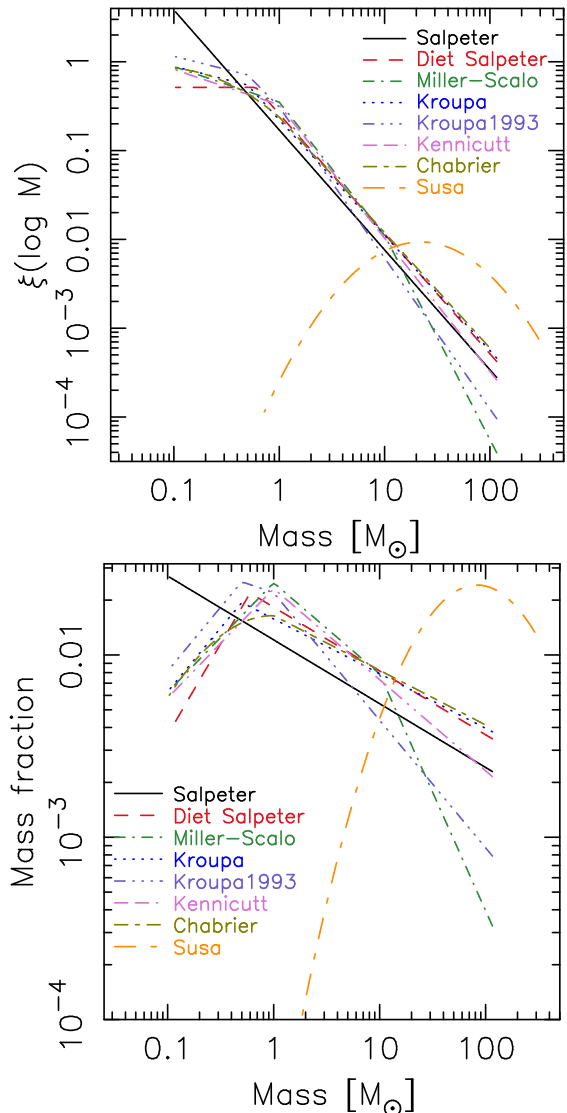


FIG. 2.— $\xi(\log_{10} m)$ (top panel) and mass fraction (bottom panel) of seven IMFs. The normalization of each IMF is carried out by using Eq. (9).

The Pop III IMF has a peak at $\sim 20 M_{\odot}$ which surely follows the mass spectrum of the Pop III in Susa et al. (2014). It is noted that the very massive stars ($> 140 M_{\odot}$) with $Z = 0$ results in pair-creation instability SNe (Barkat et al. 1967) and so far there is no clear relic which predicts the existence of the pair-creation instability SNe (Umeda & Nomoto 2002, 2005; Kobayashi et al. 2011b). With our Pop III IMF, the contribution of the pair-creation instability SNe is negligible and thus, there is no discrepancy.

There is a possibility that the IMF is not universal. For instance, the top-heavy IMF is favored to obtain a sufficient number of faint sub-mm galaxies in semi-analytical models (Baugh et al. 2005; Nagashima et al. 2005) (see also Hayward et al. 2013, which does not require a top-heavy IMF to reproduce the number count of sub-mm galaxies). Also, it is used in galaxy formation simulations (Okamoto et al. 2005). As is described in the above studies, the top-heavy IMF is utilized for a case with violent events such as mergers and

when strong shocks take place. Recent observations indicate that IMF slopes alter depending on host galaxy mass (Conroy & van Dokkum 2012; Kalirai et al. 2013; Spiniello et al. 2014). Suda et al. (2013) reported that there is a tension between binary population synthesis results and observed AGB stars in the galactic halo if the present-day IMF is applied. In the current version of CELib, the IMF does not allow situation-dependent changes to its slopes and mass range, except for in the case of extremely metal poor stars.

4.2. Stellar Lifetime

In this library, we adopt the metallicity dependent lifetime table provided by Portinari et al. (1998) (see their table 14). The definition of the lifetime in Portinari et al. (1998) is the sum of the H-burning and He-burning time scales of the stellar tracks of the Padova library. The lifetimes depend slightly on the stellar metallicity. Their table covers stars from $0.6 M_{\odot}$ to $120 M_{\odot}$ and from $Z = 0.0004$ to $Z = 0.05$. Note that we use the linear interpolation in Z and the lifetime of $Z = 0.0004$ ($Z = 0.05$) if the metallicity is below (above) the value. It is also worth noting that there are other stellar lifetime data: both analytical forms (e.g., Tinsley 1980; Greggio & Renzini 1983; Maeder & Meynet 1989; Hurley et al. 2000) and grid data (Schaller et al. 1992). The differences between them are not so large.

For Pop III stars, we need the lifetime of stars $> 120 M_{\odot}$. Unfortunately, the lifetime table of Portinari et al. (1998) did not provide the lifetime of this mass range. Here, we use the lifetime data obtained by Schaerer (2002). He calculated the lifetime of the Pop III stars within a mass range of $80 M_{\odot} \leq m \leq 1000 M_{\odot}$. To make the lifetime data of $Z = 0$ stars, we combine the Portinari et al. (1998)’s lifetime data of $Z = 0.0004$ and the Schaerer (2002)’s lifetime data of $Z = 0$. We employ the Portinari et al. (1998)’s lifetime data to less than $120 M_{\odot}$ stars whereas we adopt the Schaerer (2002)’s lifetime data of $150\text{--}300 M_{\odot}$ stars. With these two sets of data, we can cover the full range of Pop III stars ($0.7\text{--}300 M_{\odot}$).

Figure 3 shows the stellar lifetime as a function of mass. Here, we interpolate both mass and metallicity and the linear interpolation is used for this process. Apparently, the curve of the lifetime is not smooth. These ‘‘bumps’’ come from the original data, and they will propagate other quantities. Thus, instead of using this data, we make polynomial functions using the least square method and use them as the fiducial ones. The procedure is described below.

We assume that the lifetime distribution function can be described using the following polynomial function:

$$\log_{10}(t_*) = \sum_{k=0}^{k \leq 6} c_{\text{LF},k} [\log_{10}(m_*)]^k, \quad (21)$$

where m_* is the mass of stars in units of M_{\odot} , t_* is the lifetime of a star with m_* in the unit of year, and $c_{\text{LF},k}$ is the coefficient of k -th power of $\log_{10}(m_*)$. Coefficients are summarized in table 1. The first three coefficients for $Z = 0.02$ (9.99, -3.55, 2.60) are not far from those found in the other fitting formula for the stellar lifetime of Eq. (5) in Greggio & Renzini (1983) (10, -4.319, 1.543) which was based on Rood (1972) and Becker (1979).

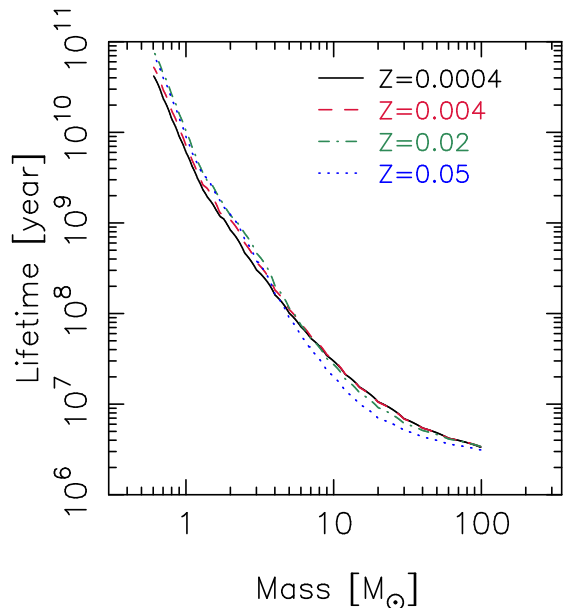


FIG. 3.— Stellar lifetime as a function of its mass. Curves represent the cases for five different metallicities, i.e., $Z = 0.0004, 0.004, 0.02,$ and 0.05 .

Using the five fitted functions and the results of their interpolations in the direction of the metallicity (we use the linear interpolation), we obtain smoothed lifetime distribution functions. We show the lifetime distributions of five representative metallicities in figure 4. The typical difference between the original and the smoothed lifetimes at a given mass is less than 10%. CELib adopts these smoothed lifetime distribution functions as the fiducial ones.

TABLE 1
COEFFICIENTS OF STELLAR LIFETIME DISTRIBUTION FUNCTIONS
USED IN EQ. (21).

| | Metallicity | | | | | |
|-------------------|-------------|--------|--------|-------|--------|-------|
| | 0.0 | 0.0004 | 0.004 | 0.008 | 0.02 | 0.05 |
| $c_{\text{LF},0}$ | 9.77 | 9.77 | 9.84 | 9.90 | 9.99 | 9.95 |
| $c_{\text{LF},1}$ | -3.40 | -3.40 | -3.40 | -3.47 | -3.55 | -3.41 |
| $c_{\text{LF},2}$ | 2.18 | 2.17 | 2.62 | 2.75 | 2.60 | 2.60 |
| $c_{\text{LF},3}$ | -2.05 | -1.95 | -3.51 | -3.84 | -3.60 | -5.39 |
| $c_{\text{LF},4}$ | 1.29 | 1.11 | 2.76 | 3.06 | 2.81 | 5.53 |
| $c_{\text{LF},5}$ | -0.362 | -0.250 | -0.973 | -1.08 | -0.911 | -2.35 |
| $c_{\text{LF},6}$ | 0.0353 | 0.0112 | 0.126 | 0.138 | 0.0988 | 0.358 |

It is convenient if we have an inverse function that can tell us the mass of a star which just died when we enter its lifetime. Again, we use the polynomial fitting so that we can obtain such functions,

$$\log_{10}(m_*) = \sum_{k=0}^{k \leq 6} c_{\text{MD},k} [\log_{10}(t_*)]^k, \quad (22)$$

where $c_{\text{MD},k}$ is the coefficients and they are listed in table 2. Figure 5 shows the functions of Eq. (22). In the metallicity direction, we again use the linear interpolation.

4.3. Elements considered in this library

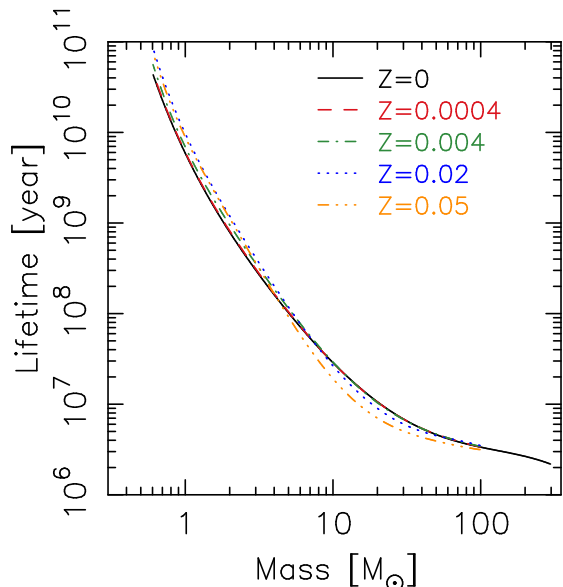


FIG. 4.— Same as figure 3, but reconstructed by the polynomial functions. The lifetime of zero metal stars, which is the combination of the Portinari et al. (1998)’s lifetime data ($\leq 120 M_{\odot}$) and the Schaerer (2002)’s lifetime data ($\geq 150 M_{\odot}$), are also shown.

TABLE 2
COEFFICIENTS OF MASS WHO DIED AT A GIVEN TIME USED IN EQ. 22.

| | Metallicity | | | | | |
|------------|-------------|---------|---------|---------|---------|---------|
| | 0.0 | 0.0004 | 0.004 | 0.008 | 0.02 | 0.05 |
| $c_{MD,0}$ | 2590 | 2560 | 2320 | 2470 | 2560 | 3640 |
| $c_{MD,1}$ | -1750 | -1740 | -1550 | -1650 | -1690 | -2460 |
| $c_{MD,2}$ | 493 | 492 | 430 | 454 | 466 | 688 |
| $c_{MD,3}$ | -73.7 | -73.8 | -63.4 | -66.6 | -68.0 | -102 |
| $c_{MD,4}$ | 6.17 | 6.21 | 5.23 | 5.47 | 5.55 | 8.53 |
| $c_{MD,5}$ | -0.274 | -0.277 | -0.229 | -0.238 | -0.240 | -0.377 |
| $c_{MD,6}$ | 0.00506 | 0.00514 | 0.00417 | 0.00430 | 0.00432 | 0.00692 |

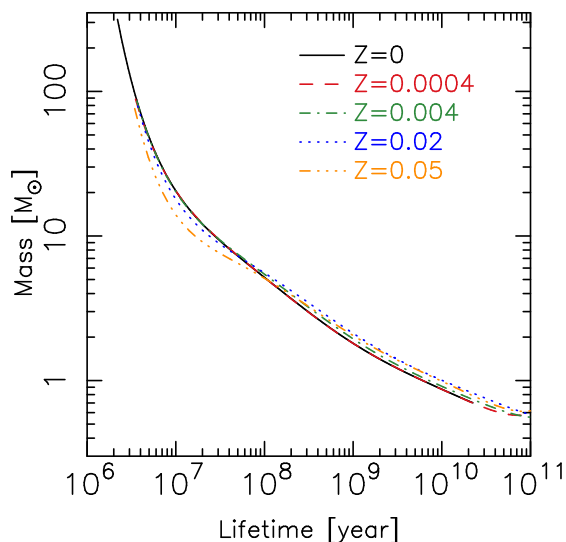


FIG. 5.— Mass of stars who just finished their lifetime as a function of time.

CELlib can follow the evolution of the thirteen representative elements. These are hydrogen (H), helium

(He), carbon (C), nitrogen (N), oxygen (O), neon (Ne), magnesium (Mg), silicon (Si), sulfur (S), calcium (Ca), iron (Fe), nickel (Ni) and europium (Eu). They cover the major products synthesized by SNe II (C, N, O, Mg, S, Ca, etc.), by SNe Ia (Fe, Ni, etc.) and by AGBs (C, N, O, etc.). The Eu is the tracer of the r -process in NSMs since most of the Eu in the solar neighborhood comes from the r -process (Burris et al. 2000). These elements, except Eu, dominate in the mass of the local ISM. Hence, these elements play a major role in the ISM as coolants (Wiersma et al. 2009a). For each element, all of the isotopes listed on yields tables are combined into one. For instance, carbon represents three isotopes, ^{12}C , ^{13}C and ^{14}C , and in this library, their masses are combined and expressed simply as “C”. Table 3 summarizes the yields tables and elements adopted in the current version of CELlib.

4.4. Yields for SNe II

There are a number of yields tables of SNe II (e.g., Maeder 1992; Woosley & Weaver 1995; Portinari et al. 1998; Rauscher et al. 2002; Hirschi et al. 2005; Nomoto et al. 2006; Kobayashi et al. 2006; Nomoto et al. 2013; Pignatari et al. 2016). In the current version of CELlib, two yields tables are implemented; those provided by Portinari et al. (1998) and Nomoto et al. (2013). These two yields tables are selectable, and users can choose one of them at the beginning of the simulation.

The yields table provided by Portinari et al. (1998) has been used very widely in galaxy formation simulations. It is based on the calculations of Woosley & Weaver (1995) and it took into account the effect of the pre-SN mass loss due to stellar winds. The original yields table covers the mass range of 1–1000 M_{\odot} and the metallicity range of $0.0004 < Z < 0.05$. Here, we only adopt the data of the mass range above 9–120 M_{\odot} as SNe II yields.

It is known that this yields table does not match the observations when one uses it for a galactic chemical evolution model, as is first described in the original paper (Portinari et al. 1998). To make it fit with observations, one generally applies ad hoc modifications to the yields, i.e., multiplying factors of 0.5, 2, and 0.5 for C, Mg, and Fe yields, respectively (see §A 3.2 in Wiersma et al. 2009b). We also follow this modification. Although we implemented these yields, we do not use them as the default yields for SNe II. We use them mainly for comparison.

The fiducial yields table for SNe II in this library is that of Nomoto et al. (2013). The yields table of Nomoto et al. (2013) for the high mass regime is based on Kobayashi et al. (2006) and Umeda & Nomoto (2002). The yields table covers the mass range of 13–40 M_{\odot} for $Z = 0.001, 0.004, 0.02$ and 0.05 .⁶ This yields table also has the data for Pop III stars. The mass range is 11–300 M_{\odot} . These data are used by combining the Pop III IMF. We use the Pop III yields when $Z_{\text{popIII}} = 10^{-5} Z_{\odot}$.

Since they also listed the yields of hypernovae (HNe) on their yields table, we adopted it and users can use

⁶ This yields table has the data at $Z = 0.008$. Since the data of this metallicity are obtained by the linear interpolation of their data of $Z = 0.004$ and $Z = 0.02$, we do not adopt it. CELlib can recompute the yields at $Z = 0.008$ internally.

TABLE 3
YIELDS AND ELEMENTS ADOPTED IN THE CURRENT VERSION OF CELIB.

| Reference | Type | H | He | C | N | O | Ne | Mg | Si | S | Ca | Fe | Ni | Eu |
|-----------------------------------|--------------|---|----|---|---|---|----|----|----|---|----|----|----|----|
| Portinari et al. (1998) | SNe II | ✓ | ✓ | ✓ | ✓ | ✓ | ✓ | ✓ | ✓ | ✓ | ✓ | ✓ | × | × |
| Nomoto et al. (2013) ^a | SNe II & HNe | ✓ | ✓ | ✓ | ✓ | ✓ | ✓ | ✓ | ✓ | ✓ | ✓ | ✓ | ✓ | × |
| Iwamoto et al. (1999) | SNe Ia | × | × | ✓ | ✓ | ✓ | ✓ | ✓ | ✓ | ✓ | ✓ | ✓ | ✓ | × |
| Travaglio et al. (2004) | SNe Ia | × | × | ✓ | ✓ | ✓ | ✓ | ✓ | ✓ | ✓ | ✓ | ✓ | ✓ | × |
| Maeda et al. (2010) | SNe Ia | × | × | ✓ | ✓ | ✓ | ✓ | ✓ | ✓ | ✓ | ✓ | ✓ | ✓ | × |
| Seitenzahl et al. (2013) | SNe Ia | × | × | ✓ | ✓ | ✓ | ✓ | ✓ | ✓ | ✓ | ✓ | ✓ | ✓ | × |
| Karakas (2010) | AGBs | ✓ | ✓ | ✓ | ✓ | ✓ | ✓ | ✓ | ✓ | ✓ | × | ✓ | ✓ | × |
| Doherty et al. (2014) | AGBs | ✓ | ✓ | ✓ | ✓ | ✓ | ✓ | ✓ | ✓ | ✓ | × | ✓ | ✓ | × |
| Campbell & Lattanzio (2008) | AGBs | ✓ | ✓ | ✓ | ✓ | ✓ | ✓ | ✓ | ✓ | ✓ | × | × | × | × |
| Gil-Pons et al. (2013) | AGBs | ✓ | ✓ | ✓ | ✓ | ✓ | ✓ | × | × | × | × | × | × | × |
| Wanajo et al. (2014) ^b | NSMs | × | × | × | × | × | × | × | × | × | × | × | × | ✓ |

^a The yields table of Nomoto et al. (2013) gives not only SNe II, but also AGBs and hypernovae. We do not adopt their AGB yields in this library.

^b In order to obtain the absolute yield value of the r -process elements, we follow the argument of Ishimaru et al. (2015); Hirai et al. (2015). See text for detail.

the HNe mode. The HNe are characterized by their large energy release (typically ten times more energy is released) and a significant amount of iron production (Nomoto et al. 2006). The HNe yields table covers 20–140 M_{\odot} for $Z = 0$ and 20–40 M_{\odot} for $Z > 0$. We introduce a parameter: the HN blending fraction f_{HN} . The definition of f_{HN} is that the number of HNe divided the number of SNe in the mass ranges of HNe. Thus, f_{HN} alters from zero to unity. If it has a value larger than zero, we blend the HNe yields to the normal SNe yields in the given mass range depending on metallicity. Since the mass range of HNe is limited, we only consider the contribution of the normal SNe when the mass range exceeds that of HNe. The remnant mass, ejecta mass, and released energy are also evaluated by taking into account the contribution of HNe.

In this paper, we show the results with $f_{\text{HN}} = 0.05$ and $f_{\text{HN}} = 0.5$, as well as $f_{\text{HN}} = 0$. The value of $f_{\text{HN}} = 0.5$ is based on Kobayashi et al. (2006). In Kobayashi et al. (2006), they used this value in order to reproduce the zinc abundance. We note that this value is one or two orders of magnitude larger than those evaluated by observations (Podsiadlowski et al. 2004; Guetta & Della Valle 2007). Moreover, there is another potential site of zinc synthesis (Wanajo et al. 2011) and thus, a high HN fraction ($f_{\text{HN}} = 0.5$) might not be necessarily required. We therefore adopt $f_{\text{HN}} = 0.05$ and CELib employs it as a fiducial value.

We pick up twelve elements (H, He, C, N, O, Ne, Mg, Si, S, Ca, Fe, and Ni) from these yields tables. The other elements listed in the original yields tables are ignored because of their minor contribution to the total amount of released metals. Note that Portinari et al. (1998) did not provide the yield of Ni. Therefore, we assume that the contribution of Ni is zero when we adopt the yields table of Portinari et al. (1998).

The yields table supplied by Portinari et al. (1998), table 10 in their paper, lists the stellar yields, Y s. Therefore, we need to convert Y s into y s in order to use galactic chemical evolution. Since the yields table also includes the remnant mass, we can evaluate y s if we know the chemical abundance pattern of the pre-existing materials using Eq. (3). For this purpose, we assume the solar abundance pattern of Anders & Grevesse (1989) and

simply change the total mass of heavy elements while keeping the original abundance ratios. The change in the total metal mass corresponds to the change in masses of H and He, while the mass ratio of H and He remains the same. We do not apply any correction to the H/He ratio to reproduce the cosmic primordial He fraction (Planck Collaboration et al. 2014) at $Z = 0$ in this process.

For the yields table of Nomoto et al. (2013), the data conversion procedure we used is rather complicated. The high mass regime of this yields table consists of the stellar yields from SNe II, HNe and remnant masses of each progenitor’s mass and metallicity. In this table, the amount of the lost mass due to pre-SNe stellar winds is not explicitly included. In other words, the sum of the total mass of the stellar yields by SNe II/HNe and the remnant mass is not equal to the progenitor’s mass. We, thus, need to complement the amount of pre-SNe mass loss. Based on Kobayashi et al. (2006), we assumed no enrichment in stellar winds and complemented the lost mass with heavy elements that have the solar abundance ratio of Anders & Grevesse (1989).⁷ From these reconstructed Y s and remnant masses, we derived net yields y s. For Pop III stars, we assumed the primordial composition of Planck Collaboration et al. (2014) for the progenitors’ chemical composition.

The IMF weighted yields per 1 M_{\odot} SSP particle with the yields table of Nomoto et al. (2013) are shown in figure 6. No contributions from HNe are assumed in this figure. Here, we assumed the Chabrier IMF of which the mass range is 0.1–100 M_{\odot} . The difference induced by the metallicity of the progenitor SSP particle is also shown in this figure. For the $Z = 0$ case, the Susa IMF is adopted. We used Eq. 4 to depict this figure. We note that the ejecta due to stellar winds are included in the SN ejecta, for simplicity. We can see that the oxygen release amount is the most prominent and other elements, such as He, Ne, Mg, and Si, follow it. When the SSP particle’s

⁷ There is another way to fill the stellar wind yields by using the data of pre-SNe yields of massive stars including metallicity dependent mass loss and rotation effects (see Romano et al. 2010). However, we do not adopt this mainly because they (models which give stellar yields and pre-supernova yields) are not generated by the same model and thus they might be inconsistent when we connect them without some tuning.

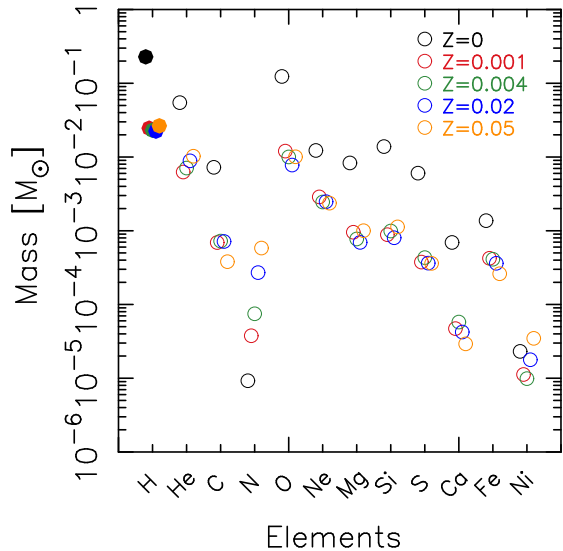


FIG. 6.— Yield of each element per $1 M_{\odot}$ SSP particle. The yields table of Nomoto et al. (2013) is used. Open circles are the positive yields whereas filled circles are the negative yields but their absolute values. The Chabrier IMF with the mass range of $0.1\text{--}100 M_{\odot}$ is assumed. Note that the yields table of Nomoto et al. (2013) provides the SNe II yields of $13\text{--}40 M_{\odot}$ stars for Pop I/II. For the case of $Z = 0$, the Susa IMF with a mass range of $0.7\text{--}300 M_{\odot}$ is adopted. The yields table of Nomoto et al. (2013) supplies the yields of $11\text{--}300 M_{\odot}$ stars for $Z = 0$. $f_{\text{HN}} = 0$ is assumed.

metallicity increases, the yields also increase. The IMF weighted yields of Pop III stars are typically a factor of five larger than those of Pop I/II stars. However, their contribution is rather limited (see §7).

In figure 7, we show the case with $f_{\text{HN}} = 0.5$. The most prominent difference is found in the yields of Fe and Ni. They increase several times when we compare those found in the case with $f_{\text{HN}} = 0$. Since the difference between the yields with $f_{\text{HN}} = 0$ and $f_{\text{HN}} = 0.05$ are almost identical, we do not show here.

Figure 8 shows the IMF weighted yields of Portinari et al. (1998). The modifications of Wiersma et al. (2009b) were applied. From these figures (figures 6, 7 and 8), we see that the differences between them are insignificant since we applied the modifications. We will investigate the difference between these two yields when applying simulations of chemical evolution in §7.

4.5. Yields for SNe Ia

For SNe Ia, CELib implemented four different yields tables based on one- (Iwamoto et al. 1999), two- (Travaglio et al. 2004; Maeda et al. 2010), and three- (Travaglio et al. 2004; Seitzzahl et al. 2013) dimensional simulations. In total, CELib holds six one-dimensional models, four two-dimensional models, and 17 three-dimensional models and it is possible to use any of them (users should select their preferred model before calling the initialization routine of CELib). An extra model which consists of metallicity dependent yields based on the three-dimensional models of Seitzzahl et al. (2013) can be selected. All models are of a thermonuclear explosion of a carbon-oxygen white dwarf that reaches the Chandrasekhar-mass. Thus, the yields tables consist of elements which are equal to or heavier than carbon.

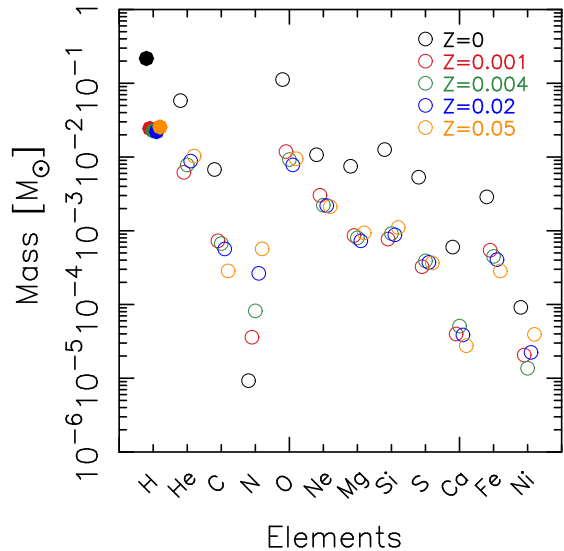


FIG. 7.— Same as figure 6, but $f_{\text{HN}} = 0.5$.

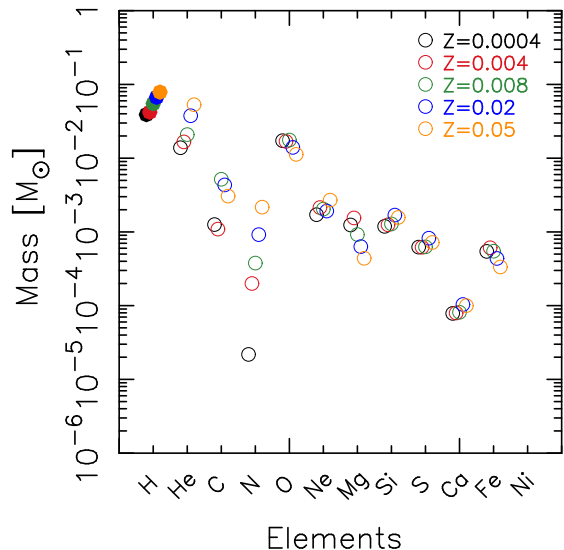


FIG. 8.— Same as figure 6, but with the yields of Portinari et al. (1998). The yields data of $8\text{--}100 M_{\odot}$ is used since the Chabrier IMF is used. The modifications of Wiersma et al. (2009b) are applied.

The first one is the yields table given by Iwamoto et al. (1999) which was computed by one-dimensional simulations. In their table, seven different models of SN Ia were listed. In their models, the W7 and the WDD2 (deflagration-detonation transition model with the transition density of $2.2 \times 10^7 \text{ g}$) models agree with the observational constraint on the ^{56}Ni production. In the literature, the W7 model is the most widely used. CELib takes all of the seven models listed in the table so that users can choose their preferred model. The original table includes 66 elements and isotopes (see table 3 in their paper). We adopted ten elements, i.e., C, N, O, Ne, Mg, Si, S, Ca, Fe and Ni. We summed up all isotopes of each element.

The second SN Ia yields table is that supplied by Travaglio et al. (2004), which was derived from their two- and three-dimensional simulations of thermonuclear burning. Unlike one-dimensional simulations where

the flame speed is a free parameter, there is no need to adjust this parameter in multi-dimensional simulations. Depending on the spatial resolution, model dimensions, and ignition configurations (centered v.s. multipoint ignition), there are five models (one two-dimensional model and four three-dimensional models). While all models satisfy the observed ^{56}Ni production rate (Stritzinger et al. 2006), they noted that the three-dimensional model with the highest spatial resolution, b30_3d_768, is the best one of which the synthesized amount of ^{56}Ni is the largest. Ten elements the same as those in the one-dimensional case are adopted.

The third is the yields of Maeda et al. (2010). They gave yields of four models such as the pure-deflagration explosion model (C-DEF) and the delayed detonation models with the center and off-center deflagration (C-DDT and O-DDT), as well as the standard W7 model. All four models are implemented in CELib. Note that their W7 model is essentially the one-dimensional model and is not important in this context. There are ~ 70 elements and isotopes, but we adopt ten elements which are the same as those adopted in Iwamoto et al. (1999). According to their comparisons between their yields and solar abundance ratios of Ni over Fe and Si over Fe, they remarked that O-DDT is the most favorable model.

The fourth and last one is the yields table evaluated by three-dimensional simulations of SN Ia provided by Seitenzahl et al. (2013). In their study, they mainly changed the number of ignition points and solved the nucleosynthesis using test particles. The number of ignition points tested is 1–1600. Moreover, they changed the central density and the initial metallicity of the progenitor star. Although the ejecta mass of ^{56}Ni in all these models is a factor of two more/less than the amount estimated from observations (Stritzinger et al. 2006), the model with 100 ignition points is almost the same as the observational estimate and is regarded as the fiducial model. As with previous yields tables, CELib adopts the ten primary elements.

In Seitenzahl et al. (2013), they also assessed the dependence of the progenitor metallicity. They employed the N100 model and changed the progenitor metallicity from 0.5 to 0.01 times of the canonical ^{22}Ne mass fraction of 0.025. These models are labeled as N100_Z0.5, N100_Z0.1, and N100_Z0.01. In CELib, the model, which returns the metallicity dependent yields of SN Ia, is implemented using these yields. By reducing the initial amount of ^{22}Ne , the production rate of ^{56}Ni decreases. This tendency is preferable because overproduction is observed in the canonical models (See details in section 3.2 in Seitenzahl et al. 2013).

In all yields tables, the ejecta mass of each element, Y_i , is listed. We use it when SN Ia takes place in an SSP particle.

Figure 9 displays the distributions of metals in the ejecta of a single SN Ia. Four representative models are selected from the implemented yields tables. In these four models, the Fe and Ni production rates are almost identical. These models reproduce or are close to the observed amount of ^{56}Ni production. Three models (models from Iwamoto et al. 1999; Maeda et al. 2010; Seitenzahl et al. 2013) are almost identical even in the light elements. For light elements (C, N, O, Ne), the

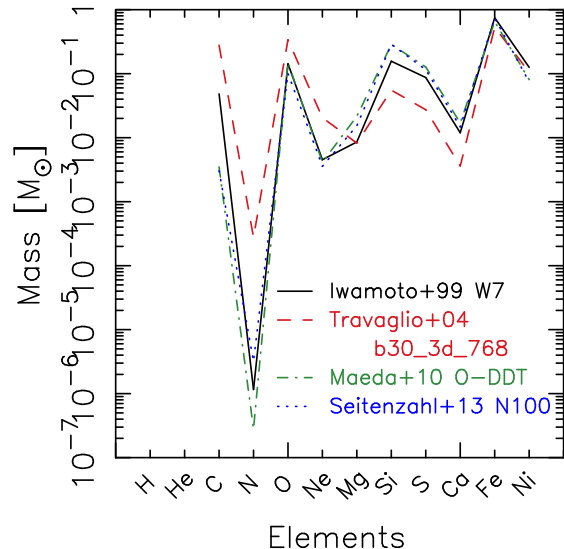


FIG. 9.— Stellar yields of SN Ia. Four representative models, the W7 model from Iwamoto et al. (1999), the b30_3d_768 model from Travaglio et al. (2004), the O-DDT model from Maeda et al. (2010), and the N100 model from Seitenzahl et al. (2013), are shown.

model of Travaglio et al. (2004) has more leftovers. It is mentioned in Travaglio et al. (2004) that the amount of the leftovers increases when increasing the resolution and changing the dimensions from two to three. We need to keep in mind that there are fluctuations from model to model.

Multidimensionality can remove a free parameter (the flame velocity). Thus, such models are more realistic. As fiducial models, we chose the N100 model of Seitenzahl et al. (2013). The metallicity dependent yields we made from models of Seitenzahl et al. (2013) are also one of the fiducial models. Differences due to the adopted SN Ia yields are studied in §7.

The metallicity dependencies of the yields in Seitenzahl et al. (2013) are shown in figure 10. Here we show the quantities of

$$Y_{\text{diff},i}(Z) = Y_i(Z) - Y_i(Z_{\odot}), \quad (23)$$

where Z_{\odot} is the solar metallicity and we adopt the value of Asplund et al. (2009) ($Z = 0.0134$). There is a tendency for the amounts of O and Ni to decrease with decreasing metallicity, whereas those of Mg, Si, Ca and Fe increase with increasing metallicity. It is noted by Seitenzahl et al. (2013) that the metallicity dependent yields are favorable because it reduces the overproduction of ^{58}Ni and ^{54}Fe .

4.6. Yields for AGBs

For the AGB yields table, we combine four yields tables of AGBs given by the Monash group (Campbell & Lattanzio 2008; Karakas 2010; Gil-Pons et al. 2013; Doherty et al. 2014) so that we can cover wide mass and metallicity ranges.

We refer to Karakas (2010) for the yields from low- and intermediate-mass AGB stars. These yields are the successor to those obtained by their previous study (Karakas & Lattanzio 2007) with an improved reaction rate network. The covering range of this yields table in both mass and metallicity is the broadest (see table 2

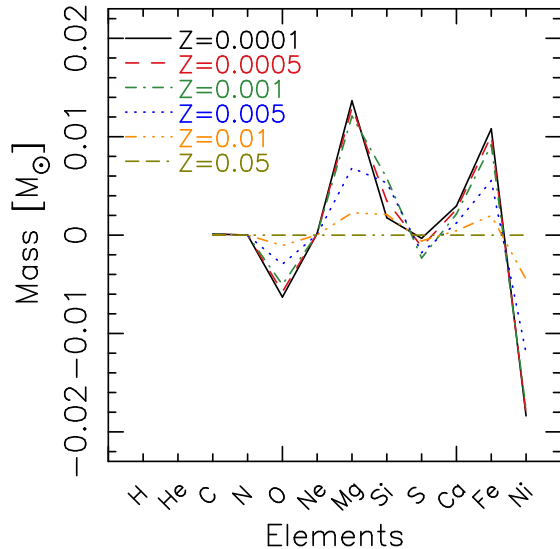


FIG. 10.— Mass difference of each element from the SN Ia yields of the solar metallicity. Metallicity dependent yields are based on Seitenzahl et al. (2013).

in Karakas & Lattanzio 2014). It covers the metallicity range of $Z = 0.0001, 0.004, 0.008$ and 0.02 and the mass range of $1-6 M_{\odot}$.

The yields table provided by Karakas (2010) does not include the yields from super-AGB stars ($> 6 M_{\odot}$). Therefore, there is a gap between SNe II and AGBs (‘super-AGB star gap’ Romano et al. 2010; Kobayashi et al. 2011a). In order to diminish this gap, we combine the Karakas’s yields table with the yields table of super-AGB stars given by Doherty et al. (2014). In Doherty et al. (2014), they tested different mass-loss rate models and gave two of them in the electric form. Here we adopted their VM93 model where the mass loss rate follows the model of Vassiliadis & Wood (1993) and which was regarded as the standard model in their study. The yields table of Doherty et al. (2014) covers $Z = 0.004, 0.008$ and 0.02 and $6.5-9 M_{\odot}$. The maximum mass listed on the table changes depending on the metallicity from $8 M_{\odot}$ at $Z = 0.004$ to $9 M_{\odot}$ at $Z = 0.02$. We adopt the data of $6.5-8 M_{\odot}$ with the three metallicities. In order to fit the Karakas (2010)’s table, we use the yields at $Z = 0.004$ to the yields at $Z = 0.0001$ because the Doherty et al. (2014)’s yields table did not provide data at $Z = 0.0001$. Since both the yields tables of Karakas (2010) and Doherty et al. (2014) were generated by the Monash University stellar evolution program (MONSTER) (Frost & Lattanzio 1996), they would have a high affinity.

These two yields tables did not cover the extremely low-metallicity AGBs. In CELib, the yields at $Z = 0$ in Campbell & Lattanzio (2008) and those at $Z = 10^{-5}$ in Gil-Pons et al. (2013) are used for this metallicity range. The yields table of Campbell & Lattanzio (2008) covers a mass range $\leq 3 M_{\odot}$ and a metallicity range $Z = 0-10^{-3}$. On the other hand, the yields table of Gil-Pons et al. (2013) gives yields of low-metallicity AGB stars ($Z = 10^{-5}$) in the mass range of $4-9 M_{\odot}$. We connect these two yields tables and then generate a single AGB yields for extremely low-metallicity AGB stars of $1-8 M_{\odot}$. Again, these two yields tables were com-

puted by MONSTER. We regard these low-metallicity AGB yields as the AGB yields of $Z = 0$, for simplicity. Since the adopted metallicity of tables is slightly different, this seems to be inconsistent. However, the difference is not so large compared to the other factors in the chemical evolution model, such as the form of the IMF.

Overall, the covered range of the combined AGB yields is $1-8 M_{\odot}$ and $Z = 0-0.02$. Practically, when the metallicity of an SSP particle is below Z_{popIII} , CELib returns the yields of the Pop III AGBs. On the other hand, when the metallicity of an SSP particle is above 0.02 , CELib returns yields of $Z = 0.02$.

The two yields tables (Karakas 2010; Doherty et al. 2014) include yields of 40–80 elements and their isotopes. CELib adopts 11 elements (H, He, C, O, N, Ne, Mg, Si, S, Fe, and Ni) from them. All isotopes of each element are summed up. Since Ca and its isotopes are not included in their models, the zero yield is assumed for Ca. The Pop III AGB tables did not contain elements heavier than S (Campbell & Lattanzio 2008) and Ne (Gil-Pons et al. 2013). We hence assumed zero yields for the unlisted elements.

Although the yields tables of Karakas (2010) and Doherty et al. (2014) provide the net yields y_s , the other two yields tables do not give net yields y_s but stellar yields Y_s . Therefore, as a preprocess, we converted these table data to the net yields using Eq. (3).

Figure 11 shows the IMF weighted yields (Eq. 4) of 11 elements considered in AGBs in this library. Only AGBs from $1-6 M_{\odot}$ are taken into account. We can see that the elements of H, O, S and Fe are destroyed while those of the others are synthesized. When we compare the IMF weighted AGB yields to those obtained by SNe II (figures 6 and 8), we find that the C and N yields of AGBs are greater than those of SNe II. Hence, lighter elements are strongly affected by AGBs.

The IMF weighted yields of AGBs from $1-8 M_{\odot}$ are displayed in figure 12. Here the super-AGB yields provided by Doherty et al. (2014) are taken into account as well as the yields provided by Karakas (2010). The differences between figures 11 and 12 are non-negligible. The reason is simply that the return mass fraction of the massive AGBs is larger than those of less massive AGBs, regardless of the relatively small number of the super-AGBs. Depending on the elements, the increase in yields is about several times larger, when we adopt the effects of super AGBs. This effect can be seen in simulations of chemical evolution (see §7) while it is not significant.

The yields of Pop III AGBs are shown in figure 13. They have their own characteristic abundance pattern among C, N and O. This is due to the effect of the thermal pulsation in relatively massive stars (Gil-Pons et al. 2013). The contributions of the Pop III AGBs are, however, rather limited because of a very low chance of this feedback due to the limited metallicity range.

There are other commonly used yields tables of AGBs (van den Hoek & Groenewegen 1997; Marigo 2001; Izzard et al. 2004). These tables are compared in Wiersma et al. (2009b). They found that these agreed with each other on solar metallicity. However, they also found that there are large gaps among them in the low- Z regime. In the current version of CELib these tables are not implemented.

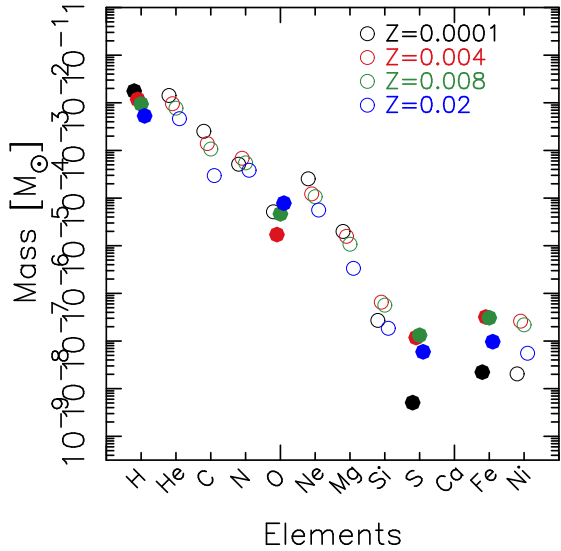


FIG. 11.— AGB yields per $1 M_{\odot}$ SSP particle. The Chabrier IMF with a mass range of $0.1\text{--}100 M_{\odot}$ is adopted and AGB stars of $1\text{--}6 M_{\odot}$ are considered. Open circles indicate the positive yields whereas filled circles show the negative yields and the absolute values are used.

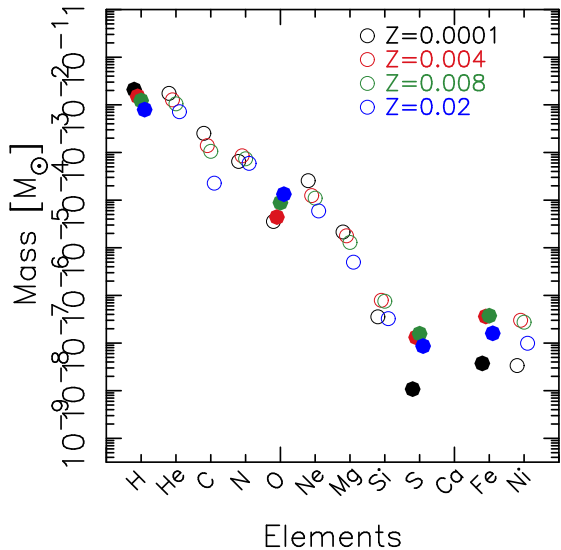


FIG. 12.— Same as figure 11, but for AGB stars of $1\text{--}8 M_{\odot}$. The contributions from the yields of super-AGB stars (Doherty et al. 2014) are taken into account.

4.7. Yields for NSMs

NSMs have gained considerable attention as the potential sites of r -process elements synthesis (e.g., Lattimer & Schramm 1976; Lattimer et al. 1977; Eichler et al. 1989). Recent numerical simulations (Goriely et al. 2011; Wanajo et al. 2014) imply that NSMs are a potential synthesis site of r -process elements. Thus, it would be desirable to take them into account in numerical simulations in order to get a comprehensive understanding of the stellar feedback in regards to galaxy formation.

This library adopts Eu as a tracer of the NSMs in which the massive r -process elements are synthesized. Following the argument in Ishimaru et al. (2015), we fix the Eu yield at $2 \times 10^{-5} M_{\odot}$ per NSM. This value is calibrated

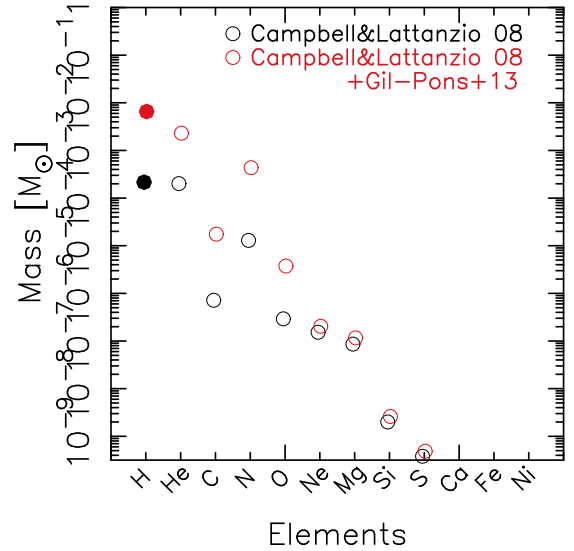


FIG. 13.— Same as figure 11, but for Pop III AGB stars of $1\text{--}3 M_{\odot}$ (Campbell & Lattanzio 2008) and $1\text{--}8 M_{\odot}$ (Campbell & Lattanzio 2008; Gil-Pons et al. 2013).

by the typical event rate of NSMs [2×10^{-3} times the event rate of SNe II (Dominik et al. 2012)] and the nucleosynthesis results of Wanajo et al. (2014); Goriely et al. (2011). The variation of the Eu yield is rather insensitive to the configuration of mergers (Goriely et al. 2011).

Although many heavy elements are synthesized in NSMs, the current version of CELib ignores other elements. Their contributions are negligible for the whole chemical evolution because of a relatively low event rate of NSMs (see the next section for the argument regarding the NSM rate).

4.8. Released energy and return mass fraction

The amount of released energy and return mass from individual events are also described in the yields tables. Here we summarize these quantities.

For SNe II, the released energy of each SN is set to 10^{51} erg when the yields table of Portinari et al. (1998) is selected. When the yields table of Nomoto et al. (2013) is selected, the released energy listed in the table is used. The normal SNe release 10^{51} erg per SN whereas the Pop III SNe and HNe release more than 10 times more energy than the normal SNe and the released energy depends on the progenitor mass.

Table 4 shows IMF weighted released energy from SNe II. These quantities are calculated by using Eq. 7. The integrated mass ranges for the yields table of Nomoto et al. (2013) are $13\text{--}40 M_{\odot}$ for $Z > 0$ and $11\text{--}300 M_{\odot}$ for $Z = 0$, whereas that of Portinari et al. (1998) is $9\text{--}120 M_{\odot}$. When we compare the released energies evaluated with the yields tables of Nomoto et al. (2013) with $f_{\text{HN}} = 0$ and Portinari et al. (1998) we find that the case with Portinari et al. (1998) releases about twice as much energy as that with Nomoto et al. (2013), reflecting the narrow mass range for SNe II in Nomoto et al. (2013).

An SSP particle with the Pop III IMF releases a significant amount of energy because they have a lot of massive stars. The released energy from Pop III stars is two to five times greater than those with IMFs for Pop I/II. In the case with $f_{\text{HN}} = 0.05$, the increase of the released

energy is only $\sim 25\%$. If we adopt $f_{\text{HN}} = 0.5$, the integrated released energy increases 3-4 times depending on the adopted IMF. Hence, significant impacts from these modes are expected for galaxy formation.

By dividing the released energy listed in table 4 by 10^{51} erg, we can obtain the typical number of SNe II from a $1 M_{\odot}$ SSP particle. For IMFs of Pop I/II, typical numbers of SNe II are $0.0023\text{--}0.0058 M_{\odot}^{-1}$ for the yields table of Nomoto et al. (2013) with $f_{\text{HN}} = 0.0$ and $0.0043\text{--}0.01 M_{\odot}^{-1}$ for that of Portinari et al. (1998). These are comparable to those used in the previous galaxy formation simulations.

Table 5 summarizes the return mass fraction of each IMF by SNe II with the yields of Nomoto et al. (2013). To evaluate these values, we used Eq. (5). Here, we assumed $f_{\text{HN}} = 0.0$. We note that the return mass fractions with $f_{\text{HN}} = 0.5$ are almost identical to those with $f_{\text{HN}} = 0.0$. The IMF to IMF variation is about a factor of 2 and generally, the return mass fraction increases with increasing metallicity. When we adopt the Pop III IMF, the return mass fraction reaches 89% which is about 10 to 20 times larger than those with IMFs for Pop I/II.

The return mass fraction of SNe II with the yields table of Portinari et al. (1998) is shown in table 6. Typically, the return mass fraction increases $\sim 60\%$ when we compare it to that summarized in table 5. This is because the yields table of Nomoto et al. (2013) covers a narrow mass range ($13 M_{\odot} \leq m \leq 40 M_{\odot}$).

For SNe Ia, a 10^{51} erg per SN is assumed for simplicity, although the typical energy of a SN Ia in models is slightly larger than 10^{51} erg. The return mass of each event is typically $1 M_{\odot}$. As is expected, the amount of the return mass from SNe Ia is insignificant.

The return mass fraction due to AGBs is shown in table 7. This quantity is also evaluated by using Eq. (5). Reflecting the shape of the IMF in the lower mass regime, the return mass fraction changes when we change the adopted IMF. However, the variation is less than a factor of 2. The return mass fraction of AGBs is 1.5–2.5 times as much as those of SNe II. On the other hand, since the net yields in AGBs are smaller than those in SNe II (figures 6, 8, 11 and 12), the contribution from AGBs to chemical evolution is not necessarily greater than that from SNe II. We confirm this in §7.

For AGBs and NSMs, we assume that they do not release energy for simplicity, although the energy and momentum release via stellar winds and jets might affect the evolution of galaxies.

Figures 14 and 15 show the evolutions of cumulative return mass fractions of 12 primary elements as a function of age. In these figures, the amounts of return masses from SNe II, SNe Ia, and AGBs are taken into account. For SNe II and AGBs, the mass release occurs at the end of progenitors' lifetimes whereas, for SNe Ia, the mass release follows a power-law type event rate (see §5.2). The evolution of the return mass fractions is characterized by two phases: the early phase (~ 10 Myr) is due to SNe II and the late phase ($t > 4 \times 10^7$ yr) is due to both SNe Ia and AGBs.

In the zero-metallicity case (figure 14), we can see the evolution return masses, except for N, are characterized only by SNe II because of their specific IMF and high return mass fraction. On the other hand, in the $Z = Z_{\odot}$

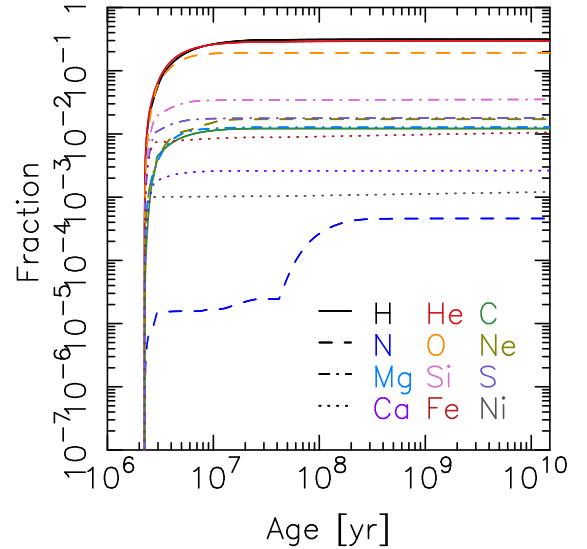


FIG. 14.— Cumulative return mass fractions of 12 primary elements as a function of SSP particle age. Solid, dashed, dot-dashed and dotted curves correspond to groups of (H, He, C), (N, O, Ne), (Mg, Si, S) and (Ca, Fe, Ni), respectively. $Z = 0$ is assumed, and thus the Susa IMF ($0.7\text{--}300 M_{\odot}$) is used. SNe II, SNe Ia, and AGBs are taken into account. For SNe II, we use the yields table of Nomoto et al. (2013), while for SNe Ia, we use that of Seitenzahl et al. (2013) (N100). The AGB yields are the combination of Campbell & Lattanzio (2008) and Gil-Pons et al. (2013). We assume that the amount of mass loss in each massive star is released at the same time as its SN explosion.

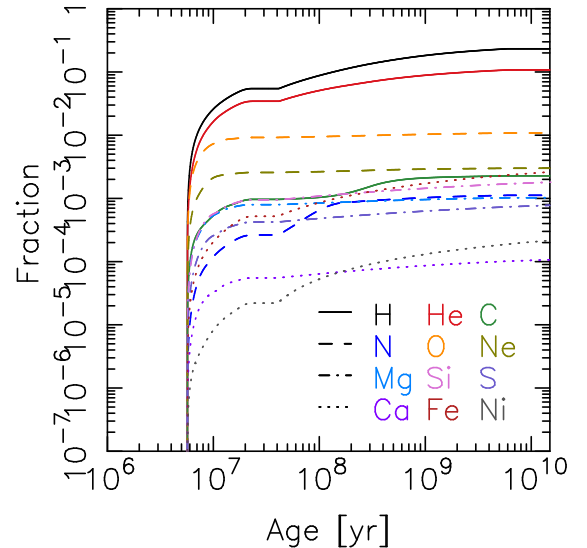


FIG. 15.— Same as figure 14, but with $Z = 0.0134$. The Chabrier IMF with the mass range of $0.1\text{--}100 M_{\odot}$ is assumed. Yields tables for SNe II and SNe Ia are the same as those used in figure 14. For AGBs, we use the combined yields table of Karakas (2010) and Doherty et al. (2014).

case (figure 15), we can clearly read the contributions of three different feedbacks. For instance, the evolutions of the return O, Mg and Si are almost unchanged after SNe II ($> 3 \times 10^7$ yr), since these α elements are mainly released from SNe II and others contributions are almost negligible. Those of Ca, Fe and Ni have two phases and the late phase is due to the SNe Ia. The late stage evolutions of H, He, C and N are owing to AGBs.

TABLE 4
RELEASE ENERGY OF SNE II PER A UNIT MASS (erg M_{\odot}^{-1}).

| | Salpeter | Diet Salpeter | Miller-Scalo | Kroupa | Kroupa1993 | Kennicutt | Chabrier | Susa |
|-----------------------------------|-----------------------|-----------------------|-----------------------|-----------------------|-----------------------|-----------------------|-----------------------|-----------------------|
| Nomoto et al. (2013) ^a | 3.56×10^{48} | 5.38×10^{48} | 3.00×10^{48} | 5.37×10^{48} | 2.34×10^{48} | 4.40×10^{48} | 5.75×10^{48} | 5.64×10^{49} |
| Nomoto et al. (2013) ^b | 4.44×10^{48} | 6.71×10^{48} | 3.51×10^{48} | 6.72×10^{48} | 2.84×10^{48} | 5.42×10^{48} | 7.19×10^{48} | 7.63×10^{49} |
| Nomoto et al. (2013) ^c | 1.23×10^{49} | 1.86×10^{49} | 8.08×10^{48} | 1.88×10^{49} | 7.37×10^{48} | 1.46×10^{49} | 2.02×10^{49} | 2.55×10^{50} |
| Portinari et al. (1998) | 6.31×10^{48} | 9.54×10^{48} | 6.08×10^{48} | 9.45×10^{48} | 4.29×10^{48} | 7.89×10^{48} | 1.02×10^{49} | N/A |

^a $f_{\text{HN}} = 0$, ^b $f_{\text{HN}} = 0.05$, and ^c $f_{\text{HN}} = 0.5$.

TABLE 5
RETURN MASS FRACTION OF SNE II PER UNIT MASS WITH THE YIELDS TABLE OF NOMOTO ET AL. (2013). $f_{\text{HN}} = 0$ IS ASSUMED.

| | Salpeter | Diet Salpeter | Miller-Scalo | Kroupa | Kroupa1993 | Kennicutt | Chabrier | Susa |
|-------------|----------|---------------|--------------|--------|------------|-----------|----------|-------|
| $Z = 0.0$ | N/A | N/A | N/A | N/A | N/A | N/A | N/A | 0.892 |
| $Z = 0.001$ | 0.0643 | 0.0971 | 0.0487 | 0.0975 | 0.0404 | 0.0779 | 0.104 | N/A |
| $Z = 0.004$ | 0.0641 | 0.0970 | 0.0486 | 0.0972 | 0.0403 | 0.0777 | 0.104 | N/A |
| $Z = 0.02$ | 0.0647 | 0.0978 | 0.0490 | 0.0892 | 0.0407 | 0.0785 | 0.105 | N/A |
| $Z = 0.05$ | 0.0646 | 0.0976 | 0.0490 | 0.0980 | 0.0406 | 0.0783 | 0.105 | N/A |

TABLE 6
RETURN MASS FRACTION OF SNE II PER UNIT MASS WITH THE YIELDS TABLE OF PORTINARI ET AL. (1998).

| | Salpeter | Diet Salpeter | Miller-Scalo | Kroupa | Kroupa1993 | Kennicutt | Chabrier |
|--------------|----------|---------------|--------------|--------|------------|-----------|----------|
| $Z = 0.0004$ | 0.104 | 0.157 | 0.0778 | 0.160 | 0.0632 | 0.124 | 0.170 |
| $Z = 0.004$ | 0.105 | 0.159 | 0.0783 | 0.161 | 0.0640 | 0.125 | 0.173 |
| $Z = 0.008$ | 0.114 | 0.173 | 0.0804 | 0.176 | 0.0676 | 0.134 | 0.188 |
| $Z = 0.02$ | 0.120 | 0.182 | 0.0824 | 0.185 | 0.0704 | 0.141 | 0.199 |
| $Z = 0.05$ | 0.124 | 0.187 | 0.0839 | 0.190 | 0.0720 | 0.144 | 0.204 |

TABLE 7
RETURN MASS FRACTION OF AGBS PER UNIT MASS.

| | Salpeter | Diet Salpeter | Miller-Scalo | Kroupa | Kroupa1993 | Kennicutt | Chabrier | Susa |
|--------------|----------|---------------|--------------|--------|------------|-----------|----------|--------|
| $Z = 0.0$ | N/A | N/A | N/A | N/A | N/A | N/A | N/A | 0.0186 |
| $Z = 0.0001$ | 0.165 | 0.250 | 0.292 | 0.227 | 0.212 | 0.271 | 0.243 | N/A |
| $Z = 0.004$ | 0.171 | 0.258 | 0.303 | 0.235 | 0.221 | 0.281 | 0.251 | N/A |
| $Z = 0.008$ | 0.174 | 0.262 | 0.307 | 0.238 | 0.225 | 0.286 | 0.255 | N/A |
| $Z = 0.02$ | 0.176 | 0.266 | 0.312 | 0.241 | 0.228 | 0.290 | 0.258 | N/A |

4.9. Solar abundance patterns

CELib equips three popular solar abundance patterns. These are provided by Anders & Grevesse (1989), Grevesse & Sauval (1998), and Asplund et al. (2009). In the three solar abundance patterns above, that of Asplund et al. (2009) is regarded as the fiducial one. The fiducial value of Z_{\odot} is 0.0134 in CELib. Users can choose the other two if necessary by changing a control flag.

5. REFERENCE MODELS OF STELLAR FEEDBACK

In this library, feedback models are also implemented which utilize CELib yields tables. We describe these “reference” feedback models in this section. These are optional functions of this library, and thus, it does not necessarily use them. However, these are good references for using this library in one’s own code. The models we described here give the time of events and return mass of each element, and the released energy, depending on feedback types. How to redistribute these quantities is left to the user code. The summary of our reference feed-

back models is shown in figure 16.

5.1. Feedback Model of Type II SNe

The reference model of the feedback from SNe II follows the SNe II model of Okamoto et al. (2008). In this model, all of the SNe in an SSP particle are assumed to have exploded at the same time. Therefore, the number of explosion events of SNe II is only one (see figure 16). We implement this model with a slight modification to determine the explosion time.

In order to obtain the explosion time of an SSP particle, we use the following equation:

$$\mathcal{P}_{\text{SNII}}(m_*) = \frac{1}{N_{\text{SNII}}(m_{\text{SNII,L}}; m_{\text{SNII,U}})} \times \int_{m_*}^{m_{\text{SNII,U}}} \frac{\xi(\log_{10} m)}{m} dm, \quad (24)$$

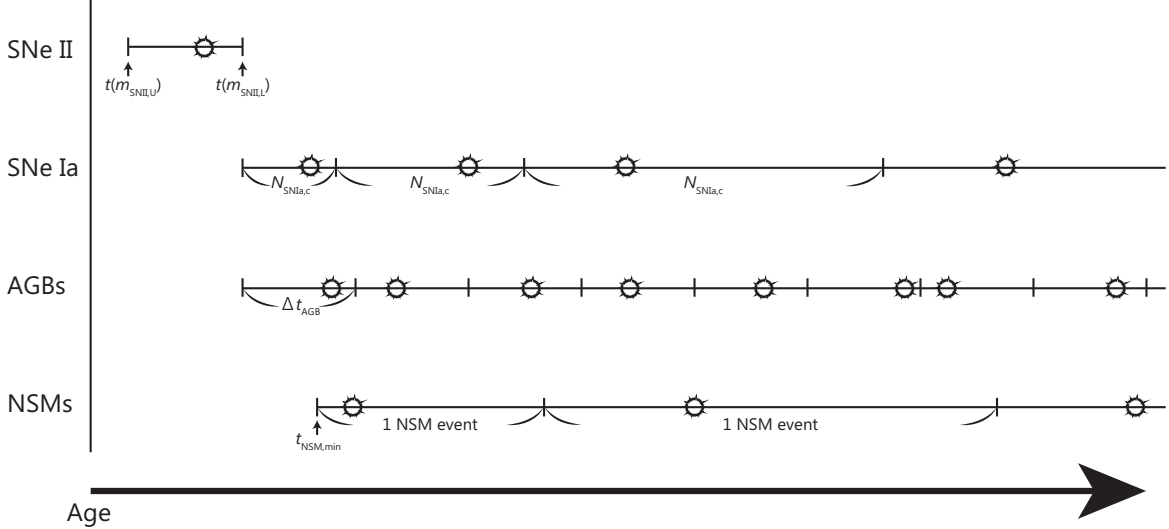


FIG. 16.— The schematic picture of our reference feedback models. From top to bottom, we describe feedbacks of SNe II, SNe Ia, AGBs, and NSMs for a single SSP particle. Time passes from left to right. Explosion marks indicate time of feedback. These times are evaluated by using random numbers. The functional form of the adopted IMF is used for the weight to determine the time. Further details are described in the text.

and

$$N_{\text{SNII}}(m_{\text{SNII,L}}; m_{\text{SNII,U}}) = \int_{m_{\text{SNII,L}}}^{m_{\text{SNII,U}}} \frac{\xi(\log_{10} m)}{m} dm, \quad (25)$$

where $m_{\text{SNII,L}}$ and $m_{\text{SNII,U}}$ are the lower and upper mass for the SNe II, respectively, and these quantities are defined by the adopted yields table. The value of $\mathcal{P}_{\text{SNII}}(m_*)$ ranges from zero to unity, since $m_{\text{SNII,L}} \leq m \leq m_{\text{SNII,U}}$. When an SSP particle is born, we generate a random real number with a domain of $[0, 1)$, $A_{\mathcal{R}}$. We then find the mass m_* which satisfies $A_{\mathcal{R}} = \mathcal{P}_{\text{SNII}}(m_*)$, and then we compute the lifetime of the star whose mass is m_* using Eq. (21). We adopt this lifetime as the explosion time of the SSP particle. The explosion time depends on both the IMF and the metallicity, and it is automatically taken care of in this library. Practically, CELib generates lookup tables at the initialization phase to reduce the evaluation cost of Eq. (24).

This model can obtain the explosion time in one trial. Thus, this implementation can reduce the number of evaluations of explosion time greatly, compared to the original implementation in Okamoto et al. (2008). As a trade-off, we need to prepare an argument in a simulation code to store the explosion time.

Figures 17 and 18 show the time distributions of our SNe II feedback model. When we set a random real number $A_{\mathcal{R}}$ of $[0, 1)$ and the metallicity of an SSP particle Z , we can obtain the corresponding explosion time. Since less massive stars dominate in the Pop I/II IMFs, the explosion time is weighted by the lifetimes of the less massive stars. The distribution of the explosion time of Pop III stars has a different shape if we compare it with those of Pop I/II stars. This is because the functional forms of IMFs are different.

5.2. Feedback Model of Type Ia SNe

The SN Ia is usually considered to be an explosion that occurs in low-mass binary systems. The candidates of the progenitors are (1) white dwarf-giant binaries (the SD scenario; Whelan & Iben 1973; Nomoto 1982) and

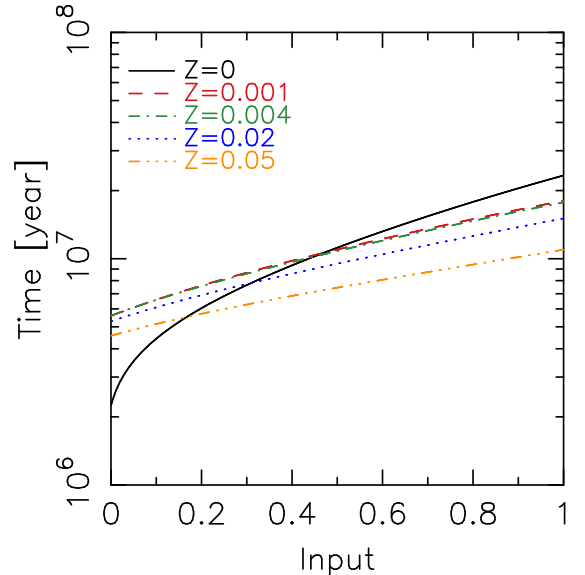


FIG. 17.— Explosion time of SNe II in our SNe II feedback model as a function of input parameter, $A_{\mathcal{R}}$. The yields table of Nomoto et al. (2013) is used. The Chabrier IMF is adopted for SSPs with $Z \geq 0.001$, whereas the Susa IMF is employed for SSPs with $Z = 0$.

(2) white dwarf-white dwarf binaries (the DD scenario; Iben & Tutukov 1984; Webbink 1984). In both cases, the explosion occurs when the white dwarf's mass exceeds the Chandrasekhar limit. They each have their own advantages/disadvantages and there is no consensus (For those who are interested in the details regarding SNe Ia, see recent reviews: Parrent et al. 2014; Maoz et al. 2014). Thus, an empirical modeling of the SN rate would currently be the best solution.

Here, we implemented two types of feedback models for SNe Ia. One is an analytical model based on the SD scenario. The implementation is identical to that of Greggio & Renzini (1983) with updated parameters by Portinari et al. (1998).

The rate function of Greggio & Renzini (1983) is based

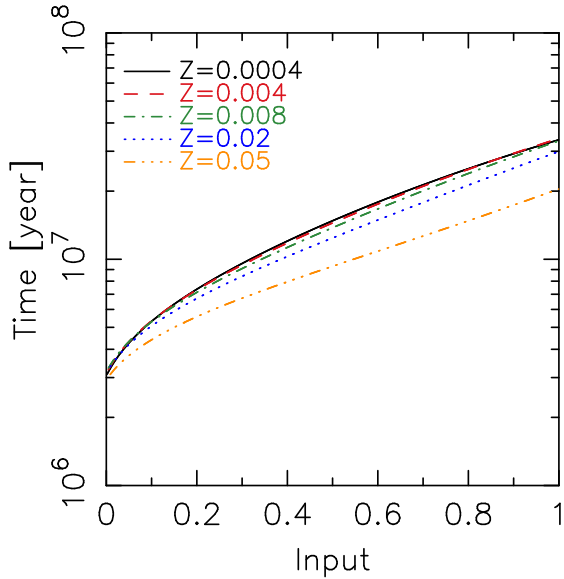


FIG. 18.— Same as figure 17, but with the yields table of Portinari et al. (1998).

on the evolution of binary systems. Assume that m_B is the total mass of a binary system and it is $m_B = m_1 + m_2$ where m_1 and m_2 are masses of the primary and secondary stars, respectively. The functional form of the SNe Ia rate (the cumulative number of SNe Ia explosions) up to time t is

$$\mathcal{R}_{\text{SNIa}}(\leq t) = b \int_{m_{B,L}}^{m_{B,U}} \frac{\xi(\log_{10} m_B)}{m_B} \left[\int_{\mu_{\min}(t)}^{0.5} f(\mu) d\mu \right] dm_B, \quad (26)$$

where $m_{B,L}$ and $m_{B,U}$ are the minimum and maximum mass of a binary system, respectively, $\mu_{\min}(t)$ is the minimum mass fraction which contributes to SNe Ia:

$$\mu_{\min}(t) = \max \left[\frac{m_2(t)}{m_B}, \frac{m_B - 0.5m_{B,U}}{m_B} \right], \quad (27)$$

and $f(\mu) = 24\mu^2$ is the distribution function of the functional mass of the secondary star. According to Portinari et al. (1998), we assume that $m_{B,L} = 3 M_\odot$, $m_{B,U} = 12 M_\odot$, and $b = 0.05$. Note that the value of b is determined in order to make the number of SNe Ia ~ 0.2 times that of SNe II (van den Bergh & Tammann 1991; Cappellaro et al. 1997). Apparently, it is necessary to recalibrate this value when one changes the assumed IMF shape, mass range, and/or the values of $m_{B,L}$ and $m_{B,U}$. However, we only use the fixed value for simplicity.

There are other analytical formulations of the SNe Ia rate for different scenarios. For instance, Hachisu et al. (1996, 1999) gave the extended model for the SD scenario where both white dwarf-main sequence and white dwarf-red giant binary systems are taken into account, and this is used in chemical evolution studies (e.g., Kobayashi et al. 1998, 2000). For the DD scenario, Greggio (2005) showed the analytical formulations. Note that the DD scenario based rate of Greggio (2005) is similar to that of the SD scenario (Greggio & Renzini 1983), as it is shown in Matteucci et al. (2009). Here, we do not implement further analytical models. We move to the empirical model.

The other model we implemented is the empirical model based on recent observations of SNe Ia. Observations imply that the delay time distribution (DTD) function of SNe Ia follows the power law of t^{-1} (e.g., Totani et al. 2008; Maoz & Mannucci 2012). The power law DTD we employed here is expressed as

$$\frac{dN_{\text{SNIa}}}{dt} = \epsilon_{\text{SNIa}} \left(\frac{t}{10^9 \text{ yr}} \right)^{p_{\text{SNIa}}}, \quad (t > 4 \times 10^7 \text{ yr}) \quad (28)$$

where $\epsilon_{\text{SNIa}} = 4 \times 10^{-13}$ and $p_{\text{SNIa}} = -1$ according to Maoz & Mannucci (2012). The time offset of 4×10^7 yr comes from the typical lifetime of a $8 M_\odot$ star (we ignore the metallicity dependence of the stellar lifetime because of its weak dependence). The integrated SNe Ia number per $1 M_\odot$ during the first 10 Gyr is 2.2×10^{-3} (Maoz & Mannucci 2012). This even rate is $1/5 \sim 1/2$ of those of the SNe II. By multiplying the mass of an SSP particle, we can obtain the event number of SNe Ia in the SSP particle.

By integrating Eq. (28), we can obtain the cumulative numbers of the SNe Ia up to time t for this model and it is expressed as

$$\mathcal{R}_{\text{SNIa}}(\leq t) = \int_0^t \frac{dN_{\text{SNIa}}}{dt'} dt'. \quad (29)$$

The event rate of the SNe Ia is very low (0.002 event per $1 M_\odot$ per 10 Gyr) and the duration time is very long (~ 10 Gyr). For instance, an SSP particle of $10^4 M_\odot$ has only 20 events in the time span of 10 Gyr. Thus, in the current feedback model of SNe Ia, either an individual event or a cluster of events follows. The explosion time of SN Ia is evaluated by the probabilistic manner which is described below.

First, we calculate the cumulative event rate of the SNe Ia as a function of time (Eqs. 26 or 29). Inversely solving this relation, we obtain

$$t_{\text{SNIa}}(N_{\text{SNIa}}) = \mathcal{R}_{\text{SNIa}}^{-1}(N_{\text{SNIa}}). \quad (30)$$

This function returns the time where the cumulative number of SNe Ia becomes N_{SNIa} . Using this equation, we obtain two epochs, $t_{\text{SNIa}}(N_{\text{SNIa}})$ and $t_{\text{SNIa}}(N_{\text{SNIa}} + N_{\text{SNIa},c})$, where N_{SNIa} is the cumulative SNe Ia event count which is finished before this step in an SSP particle. The number, $N_{\text{SNIa},c}$, is the ‘‘size of SNe Ia cluster’’. If the value is larger than unity, a SN Ia event in a simulation makes an association of $N_{\text{SNIa},c}$ SNe Ia. This can reduce the number of evaluation times of SNe Ia and can also reduce the computation time. Then, we find the next explosion time between these two epochs using a random real number and the cumulative SNe Ia rate. This is also implemented as lookup tables.

We show the cumulative event numbers of SNe Ia in figure 19. The difference in event starting times of the three models is due to the differences in lifetime between $8 M_\odot$ and $6 M_\odot$ stars and the metallicity dependence of stellar lifetime. This effect can be observed in the distribution of chemical composition (see §7.1). In this case, the final event numbers of these two models are almost comparable. As noted above, it is necessary to recalibrate the normalization value b in Eq. 26 if one wants to fit the observational value more closely. As is expected from figure 19, since we assume a constant

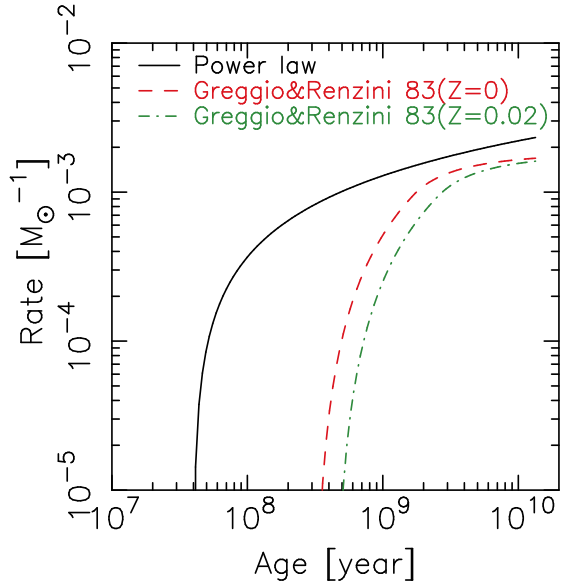


FIG. 19.— Cumulative event number of SNe Ia per a $1 M_{\odot}$ SSP particle as a function of time. Solid curve is based on the power-law type DTD (Eq. 28). Dashed and dot-dashed curves are derived from the models of Greggio & Renzini (1983) with $Z = 0$ and $Z = 0.02$, respectively.

number interval of SNe Ia, $N_{\text{SNe Ia},c}$, the time between two neighboring SNe Ia feedback events becomes longer with increasing age (see figure 16).

Here we only implemented two models while there are a lot of models of DTDs. We refer the readers to Matteucci et al. (2009) for further detailed comparison among DTD functions.

5.3. Feedback Model of AGBs

For the modeling of the AGB mass loss from an SSP particle, we assume the following conditions: (1) the AGB mass loss takes place at the end of their lifetime, (2) all AGB mass losses, which take place in a given time interval ($t \rightarrow t + \Delta t_{\text{AGB}}$), occur once in the time interval, and (3) the time is selected randomly from the time interval. The schematic picture of this feedback model is shown in figure 16.

Using Eq. (12), the number of AGB mass loss events per $1 M_{\odot}$ at a given time interval ($t \rightarrow t + \Delta t_{\text{AGB}}$) is

$$N_{\text{AGB}}(t; t + \Delta t_{\text{AGB}}) = \int_{m(t)}^{m(t+\Delta t_{\text{AGB}})} \frac{\xi(\log_{10} m)}{m} dm, \quad (31)$$

where $m(t)$ is the mass of star whose lifetime is t . In order to evaluate the time of the AGB mass loss from an SSP particle, we generate a random real number $A_{\mathcal{R}}$ with a range of $[0, 1)$ and solve the following equation for t_{AGB} ,

$$A_{\mathcal{R}} = \mathcal{P}_{\text{AGB}}(t_{\text{AGB}}; t; t + \Delta t_{\text{AGB}}), \quad (32)$$

where

$$\mathcal{P}_{\text{AGB}}(t_{\text{AGB}}; t; t + \Delta t_{\text{AGB}}) = \frac{1}{N_{\text{AGB}}(t; t + \Delta t_{\text{AGB}})} \times \int_{m(t)}^{m(t+t_{\text{AGB}})} \frac{\xi(\log_{10} m)}{m} dm. \quad (33)$$

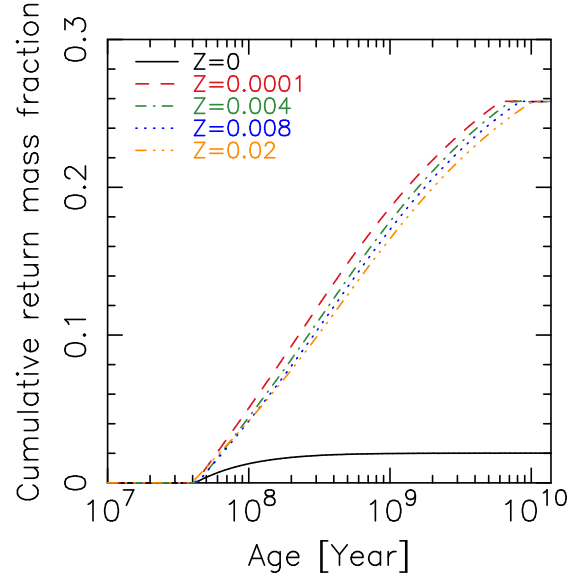


FIG. 20.— Cumulative return mass fractions of AGBs as a function of the age of the SSP particle are shown. The Chabrier IMF is assumed for the case with $Z > 0$ while the Susa IMF is employed for the case with $Z = 0$.

This $t + t_{\text{AGB}}$ is the next event time and $0 \leq t_{\text{AGB}} \leq \Delta t_{\text{AGB}}$. Practically, we prepare the lookup table of the cumulative number of N_{AGB} from $t = 0$ to $t = t_H$ with a constant time interval, Δt_{AGB} . Note that t_H is the current age of the Universe (Planck Collaboration et al. 2014) and we adopt $\Delta t_{\text{AGB}} = 3 \times 10^8$ yr as a fiducial value so that it can follow the AGB mass loss time scale (see below and figure 20).

The evaluation of the event time using Eq. (32) is carried out just after star formation and every time after the AGB mass loss event.

Within our reference AGB feedback model, we assume that there is no energy release, although it has been pointed out that stellar winds of AGB stars would have a large impact on galaxy formation, in massive galaxies in particular (Conroy et al. 2015).

The cumulative return mass fractions with different metallicities as a function of time are shown in figure 20. It is evident that for the case with $Z > 0$ the release timescale of the AGBs is very long. It starts at 4×10^6 yr and continues up to $5-9 \times 10^9$ yr. The end time depends on the metallicity. Contrary to this, the return mass of the zero metal AGBs is very small, and the release timescale is very short. The mass release stops $\sim 10^8$ yr, reflecting the IMF with a peak at $\sim 20 M_{\odot}$ for Pop III stars.

5.4. Feedback Model of NSMs

Here, we adopt a power-law type DTD (Dominik et al. 2012; Shen et al. 2015). The event rate of the NSMs, ϵ_{NSM} , is set to be proportional to the event number of the core-collapse SNe in the mass range of $20-40 M_{\odot}$ with the proportional factor of 0.01 at 10 Gyr (Ishimaru et al. 2015; Hirai et al. 2015). Since this value changes in accordance with the IMF type, it is calculated at the time of initialization. The method of evaluation of the event time is the same as that used in SNe Ia.

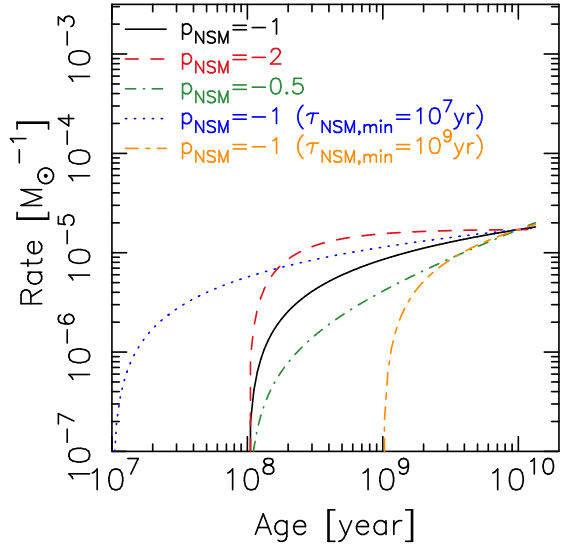


FIG. 21.— Cumulative number of NSMs as a function of the age of an SSP particle. The Chabrier IMF is assumed in order to evaluate the normalization.

The functional form of the DTD of NSMs is

$$\frac{dN_{\text{NSM}}}{dt} = \epsilon_{\text{NSM}} \times \left(\frac{t}{1 \text{ yr}} \right)^{p_{\text{NSM}}}, \quad \text{for } t > t_{\text{NSM,min}} \quad (34)$$

where $p_{\text{NSM}} = -1$ is the fiducial value but we deal with it as a parameter. $t_{\text{NSM,min}}$ is the delay-time and is also a parameter. The fiducial value is set to 10^8 yr. This is comparable to the averaged binary lifetime of the NSMs obtained through observation (Lorimer 2008) and the binary population synthesis model (Dominik et al. 2012). The parameter dependencies are studied in §7. The cumulative number of NSMs is

$$\mathcal{R}_{\text{NSM}}(\leq t) = \int_0^t \frac{dN_{\text{NSM}}}{dt'} dt'. \quad (35)$$

Figure 21 shows the cumulative numbers of NSMs as a function of the age of an SSP particle with different power-law indexes, p_{NSM} . When the power-law index decreases from -0.5 to -2 , the enrichment of Eu becomes faster. The minimum event time, $t_{\text{NSM,min}}$, is also expected to affect the enrichment history. We will show results of the parameter survey of the NSM feedback in §7.

The event time is evaluated in the same way as those of SNe Ia. We always deal with the individual events of NSM (see figure 16). In other words, the “cluster” model used in the SNe Ia model is not introduced in the NSM feedback model because of its very low event rate. As is the case with other models, CELib generates a lookup table to evaluate the event time.

6. IMPLEMENTATION

This library is written in C language. In particular, the standard of C99 is used. To guarantee the portability, this library does not require any external library. Thanks to “extern C”, C++ programs can also use this library.

This library consists of four parts: IMFs, stellar lifetimes, yields, and the reference feedback models. When the subroutine for the initialization is called by a simulation code, the library computes normalizations of

the IMFs, lookup tables of stellar lifetimes for different metallicities and their inverse lookup tables, IMF weighted yields for SNe II and AGBs, and lookup tables used for the reference feedback models. If a user changes control flags and parameters, the subroutine for initialization should be re-called. After initialization, all functions are ready to use. See appendix A where we explain the usage of the primary functions of CELib.

7. APPLICATIONS

In this section, we show the results of numerical simulations using CELib. First, we apply this library to the one-zone calculation. It is a good demonstration and benchmark test. We then show the chemical evolution of a disk galaxy which is evolving in a static Navarro-Frenk-White (NFW) halo (Navarro et al. 1997). The results of these tests prove that this library is a powerful tool for studying the chemical evolution of galaxies.

We here emphasize that the primary purpose of these tests is to demonstrate the ability of CELib. We do not carry out the detailed comparison between the numerical results and observations.

7.1. One-zone model

As an initial demonstration of this library, we use it to evaluate the metal enrichment of a one-zone model. There is a long history of the one-zone model and there are many variants (e.g., Tinsley 1980; for reviews, see Matteucci 2003 and Prantzos 2008). Since the aim of this test is only to check the capability of this library and to know the typical differences which come from the adopted yields and parameters, we carry out a closed-box simulation which does not take into account both the inflow and outflow. Thus, the history of metal enrichment that we show here has some inconsistency with observations (e.g., the G-dwarf problem). We do not investigate this discrepancy thoroughly. Since we assume a closed system, we ignore the energy releases from feedback.

A closed system with an initial gas mass of $10^{11} M_{\odot}$ is considered. The governing equation of this system is

$$M_{\text{gas}}^{n+1} = M_{\text{gas}}^n - M_*^n + M_{\text{ej}}^n \quad (36)$$

where n is the time step, M_{gas}^n is the gas mass, M_*^n is the stellar mass formed in this step, and M_{ej}^n the ejecta mass released from stars formed until this step. We integrate the system governed by this equation through 13 Gyr. The total number of steps is 10000 and a constant time interval of $\Delta t_{\text{oz}} = 1.3$ Myr is adopted. This time-interval is sufficient to resolve the time delay of SNe from the epoch of the formation of the progenitor stars. The initial mass of the stellar component is set to zero.

The gas component, whose mass is M_{gas} , consists of thirteen elements and the following relation is held for every step:

$$M_{\text{gas}}^n = \sum_i M_{\text{el},i}^n, \quad (37)$$

where the mass of i -th element at the n -th step is expressed as $M_{\text{el},i}^n$.

The second term on the right-hand side of Eq. (36) is the stellar mass formed in this step. In order to evaluate the stellar mass formed in a given step, we assumed for simplicity that the star formation rate of this system

follows an exponential form function with a timescale of $\tau_{\text{sf}} = 8$ Gyr. This timescale is comparable to the prediction from other studies for the solar neighborhood (e.g., Chiappini et al. 2001). The normalization of star formation, N_* , is evaluated by the following equation

$$M_{*,\text{total}} = N_* \int_{t=0}^{t=13 \text{ Gyr}} \exp(-t/\tau_{\text{sf}}) dt, \quad (38)$$

where $M_{*,\text{total}}$ is the stellar mass formed by star formation until the end of the simulation and it is set to half of the initial gas mass, i.e., $5 \times 10^{10} M_{\odot}$. Thus, the stellar mass formed during $n \rightarrow n+1$ is

$$M_*^n = N_* \int_{t_{\text{oz}}(n)}^{t_{\text{oz}}(n+1)} \exp(-t/\tau_{\text{sf}}) dt, \quad (39)$$

where $t_{\text{oz}}(n) = n\Delta t_{\text{oz}}$. We regard these stars, M_*^n , as the SSP with the Chabrier IMF. If we turn on the Pop III mode, the Susa IMF is used for $Z < Z_{\text{popIII}}$. Note that if the IMF (for Pop I/II stars) changes it alters the evolution of the system. However, its typical contribution would be small (Romano et al. 2005). As described below, the stellar mass at n decreases when time passes because of SNe and stellar mass loss. We thus denote the initial mass of the stars formed at step n , $M_{*,\text{init}}^n$. The metal distribution in newly born stars at a given step n is the same as that of the progenitor gas.

The third term on the right-hand side of Eq. (36) is the total return mass due to feedback, namely SNe II/Ia, AGBs, and NSMs. The return mass at step n is

$$M_{\text{ej}}^n = \sum_{k=1}^{k < n} M_{\text{ret},n}^k, \quad (40)$$

where $M_{\text{ret},n}^k$ expresses the total return mass which is released in step n from the stellar component formed in step k . We adopt the reference models of feedback described in §5. The event time and the amount of the released mass (and composition of the released mass) are evaluated through the CELib APIs (see appendix A). The important parameters regarding feedback we fixed are $N_{\text{SNIa,c}} = 3$ and $\Delta t_{\text{AGB}} = 130$ Myr.

From here we show several results obtained by our one-zone model. As mentioned above, the aim of this section is to demonstrate the capability of this library and thus not to compare the details with observational results. We compare results obtained by different yields tables for SNe II and study the contribution of SNe Ia, AGBs, and NSMs by turning on/off the feedback.

First, we compare the evolution of the stellar mass in four different models in figure 22. We adopted the yields of Nomoto et al. (2013) for SNe II, those of the model N100 in Seitzzahl et al. (2013) for SNe Ia, and those obtained by the combination of yields of Karakas (2010), Doherty et al. (2014), Campbell & Lattanzio (2008), and Gil-Pons et al. (2013). Note that HNe are not taken into account in this figure (i.e., $f_{\text{HN}} = 0$). From this figure, we can see that the SNe II and AGBs have significant effects on the long-term evolution of stellar mass of the galaxy, whereas the SNe Ia have less of an effect on galactic mass evolution. This can be understood from the tables of return mass fractions for SNe

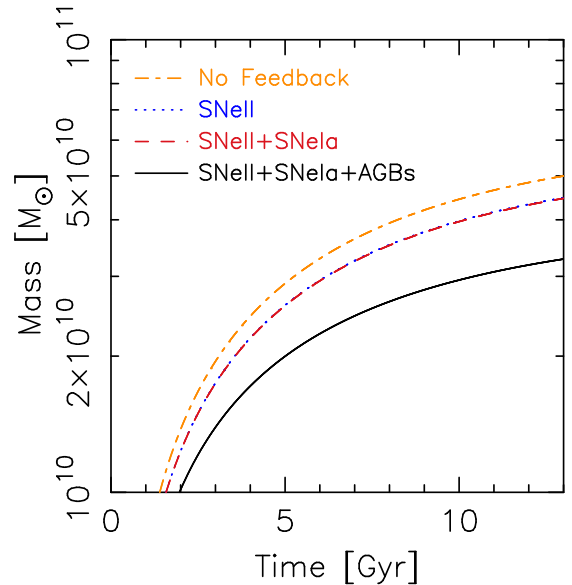


FIG. 22.— Stellar mass evolution for four different models. The yields table of Nomoto et al. (2013) is used for SNe II. The N100 model in the yields table of Seitzzahl et al. (2013) is used for SNe Ia. Both the normal and super AGB yields are adopted.

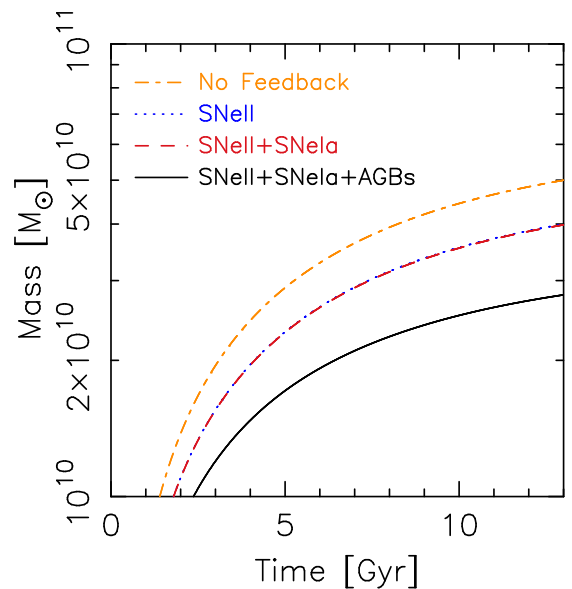


FIG. 23.— Same as figure 22, but with the yields table of Portinari et al. (1998) used for SNe II.

II/Ia and AGBs. This is crucial to understanding the baryon recycling process in galaxies.

Figure 23 shows the stellar mass evolution using the yields table of Portinari et al. (1998). The effect of SNe II is more prominent since the return mass of the Portinari et al. (1998)'s yields table is larger than that of the Nomoto et al. (2013)'s yields table (recall tables 5 and 6). This increase changes the total metallicity of the system.

Figure 24 compares the metallicity distributions of the closed system with two different yields for SNe II at $t = 13$ Gyr. The two results with the Nomoto et al. (2013)'s yields table and the Portinari et al. (1998)'s yields table with the yields modifications is almost comparable, al-

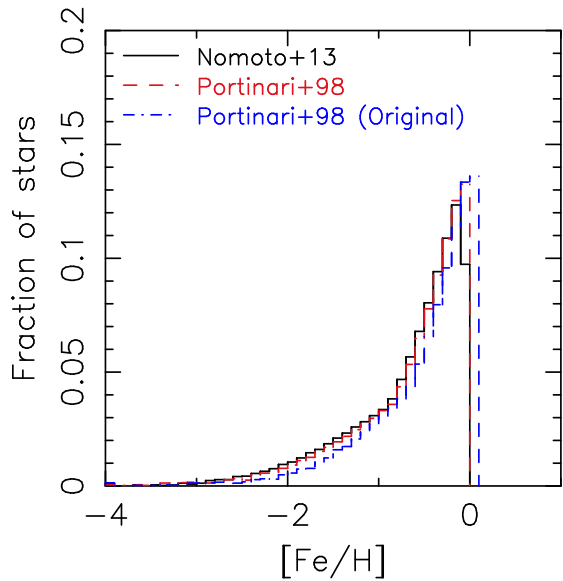


FIG. 24.— Metallicity distribution functions. The histogram with black solid lines shows the metallicity distribution function with Nomoto et al. (2013) for SNe II, whereas that with red dashed lines indicates that with Portinari et al. (1998). The model with the Portinari et al. (1998) yields table without the modifications is also shown with the blue dotted histogram. Type Ia SNe and the mass loss due to AGB are also included and model parameters are unchanged in both runs.

though the latter is slightly enriched because of the larger return mass fraction. The result that adopted the yield table of Portinari et al. (1998) without the modifications is more enriched, reflecting the fact that Fe is overproduced in the yield of Portinari et al. (1998). Nonetheless, the overall features, i.e., shapes, are not so different from each other because they are dependent on the adopted star formation history in this case.

We then show $[X/Fe]$ - $[Fe/H]$ relations, where X denotes an arbitrary element. Figures 25 and 26 display the $[X/Fe]$ - $[Fe/H]$ relations for ten primary elements. The blue, red, black, orange and purple sequences in figure 25 are the distributions of stars in $[X/Fe]$ - $[Fe/H]$ relations with different combinations of feedback. By comparing the blue sequence (the model with only SNe II) with the red sequence (that with SNe II and Ia), we see that (1) the amount of Fe is increased by SNe Ia and thus (2) the relative fraction of the other elements to Fe, i.e., $[X/Fe]$, is decreased. In this configuration, the offset between the two models starts at $[Fe/H] \sim -2.5$. This is owing to the adopted star formation history and the starting time of SNe Ia (see below).

The contributions of the AGB stars are limited in the relatively lighter elements such as C and N. This is because the AGB yields are smaller than the SNe II yields, even though the return mass fraction of AGBs is larger than that of SNe II (recall figures 22 and 23, and tables 5, 6, and 7).

When the feedback from Pop III stars is taken into account, the evolution track of the low metallicity regime changes. Slight increases are observed in C, O, Si, S and Ca while slight decreases are found in N in the low metallicity regime. Changes in others are almost negligible. Their contributions are insignificant in the high metallicity regime. These changes are reduced when we

introduce HNe, because of HNe’s high Fe yields.

It is worth noting that the overall features are similar to the figure 10 in Nomoto et al. (2013), even though we adopted a different solar abundance pattern [we adopted that of Asplund et al. (2009) whereas they used that of Anders & Grevesse (1989)] and a different one-zone model. We note that they did not show the results with the Pop III IMF case.

We see clear differences between results with Nomoto et al. (2013) and Portinari et al. (1998). In particular, the positions of plateaus of $[X/Fe]$ where the contribution of SNe II dominates are different, even with the modifications of (Wiersma et al. 2009b). On the other hand, the transitions of the $[X/Fe]$ - $[Fe/H]$ relations with SNe Ia in these two models are almost comparable. Typical differences are ~ 0.2 dex. When we turn off the modifications of Wiersma et al. (2009b), the transitions of the $[X/Fe]$ - $[Fe/H]$ relations due to SNe Ia are shifted about 1 dex and the values of $[X/Fe]$ in low metallicity regimes with flat distributions ($[Fe/H] < -1.5$) are shifted lower due to the overproduction of Fe in the yields of Portinari et al. (1998).

Here, we study the effects of SN Ia yields using the $[Ni/Fe]$ - $[Fe/H]$ diagram. Figure 27 shows results with four different models. The four models are W7 in Iwamoto et al. (1999), b_30_3d_768 in Travaglio et al. (2004), O-DDT in Maeda et al. (2010), and N100 in Seitzzahl et al. (2013). The variation of the final $[Ni/Fe]$ is ~ 0.3 dex. Models of O-DDT in Maeda et al. (2010) and N100 in Seitzzahl et al. (2013) are characterized by the off-center ignition points, resulting in the relatively low efficiency of Ni production.

In figure 28, we show the $[Ni/Fe]$ - $[Fe/H]$ relations of four different models based on Seitzzahl et al. (2013). As is expected from their yields tables, the Ni production rate increases with an increasing number of ignition points. When the metal-dependent model is used, the rise becomes more moderate compared to those found in the model with N100. This tendency would be preferable if we would like to reproduce the local $[Ni/Fe]$ - $[Fe/H]$ relation (e.g., Gratton et al. 2003). This implies it is important to take into account the metallicity dependence of SNe Ia yields.

The differences induced by different SNe Ia rates found in the $[Ni/Fe]$ - $[Fe/H]$ relation are shown in figure 29. The most crucial difference between the two models, the theoretical model based on the binary synthesis and the observation based empirical model, is the starting time of the enrichment by SNe Ia (see figure 19). The SNe Ia feedback which ignites relatively earlier leads to an earlier increase of $[Ni/Fe]$. This effect is observed in this figure. Note that the time at which the effect of SNe Ia becomes prominent is adjustable by changing the offset in DTD (Eq. 28).

The introduction of the super-AGB yields is rather limited. Since AGBs mainly affect the light elements, such as C and N, the effects of the super AGBs are found in these elements. Here, in figure 30, we show the $[N/Fe]$ - $[Fe/H]$ relation which shows the difference most clearly and we see that the increase is only 0.1 dex in $[N/Fe]$.

We close this section discussing the evolution of r -process element, Eu. Figure 31 shows the $[Eu/Fe]$ - $[Fe/H]$ relations for three different power-law indexes, $p_{NSM} = -1, -2, \text{ and } -0.5$. When the index becomes

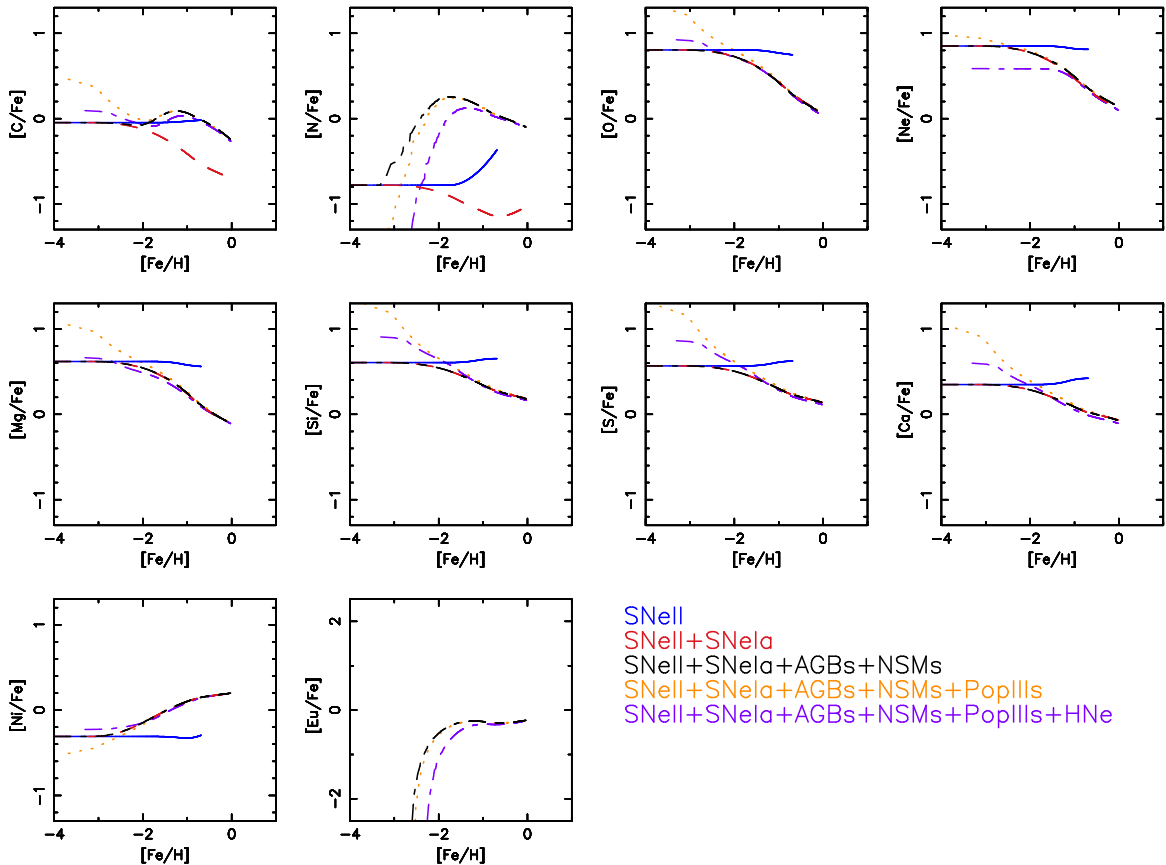


FIG. 25.— $[X/Fe]$ - $[Fe/H]$ relations. Red sequences are results with only SNe II, whereas blue sequences indicate those with both SNe II and Ia. Black sequences express results which include SNe II and Ia and the effect of the AGB mass loss. The contribution of NSM is also involved. Orange sequences indicate the results taking into account the effect of Pop IIIs, while purple ones do both the results of effect of Pop IIIs and HNe ($f_{\text{HN}} = 0.5$) to the model described with black sequences. Nomoto et al. (2013)’s yields table is used for SNe II, whereas Seitenzahl et al. (2013)’s yields table is adopted for SNe Ia (N100). The solar abundance pattern of Asplund et al. (2009) is assumed.

shallower, the evolution track moves lower. This is because a shallower index leads to a slower Eu release to the ISM and, as a result, the enrichment of Fe due to SNe Ia progresses at the time of Eu release. Since our model is too simple, it might be difficult to make a concrete conclusion.

There is a slight offset that $[Eu/Fe] \sim -0.3$ at $[Fe/H] = 0$ in our models, when we refer to observations (Suda et al. 2011, references therein). The offset at $[Fe/H] = 0$ comes from our model parameters of the Eu yield and the fraction parameter of the event number of NSMs over that of core-collapse SNe. These parameters are not observationally fixed yet and thus, it is adjustable. As long as the normalization at $[Fe/H] = 0$, it can be done by multiplying a factor so that it fits observations since here we adopt the time and metallicity independent Eu yields and the contribution of Eu to dynamics is negligible.

When we change $\tau_{\text{NSM},\text{min}}$, the evolution track also changes. For the model with $\tau_{\text{NSM},\text{min}} = 10$ Myr the extremely low metal Eu polluted stellar component appears and the evolution track follows that of the fiducial model at the late epoch. On the other hand, for the model with $\tau_{\text{NSM},\text{min}} = 1$ Gyr, the low metal Eu polluted component disappears and the evolution track is far away from the observations. It seems that such a long duration model is unfavorable. However, it is again difficult to mention

the details of metal distribution because this model assumed an instantaneous mixing model and did not take into account the mass inflow and outflow.

The tendency obtained by changing $\tau_{\text{NSM},\text{min}}$ is comparable to that reported by Matteucci et al. (2014); shorter delay-time models give a Eu enhanced stellar component with lower metallicity. The clear difference between ours and theirs is the raising point of $[Fe/H]$. We believe the difference comes from the modeling (i.e., accretion, star formation, inflow, outflow, etc) and would not be serious. Self-consistent modeling is important to understand the whole distribution of Eu. For instance, Hirai et al. (2015) can successfully reproduce both the scatter of the Eu enhanced stars distribution in the low $[Fe/H]$ regime and the raising point of $[Fe/H]$ in their three-dimensional N -body/SPH simulations with a delay-time of ~ 100 Myr.

7.2. Chemical evolution in a NFW halo

7.2.1. Initial setup

For this test, we adopt a Milky Way size galaxy using a public code `dice`⁸ (Perret et al. 2014). Here we use a system consisting of gas and dark matter. The virial

⁸ `dice` is a public code which can generate particle realizations of galaxy models and galaxy-galaxy merger configurations, as well as these for mesh codes. The distribution site is <https://bitbucket.org/vperret/dice/>.

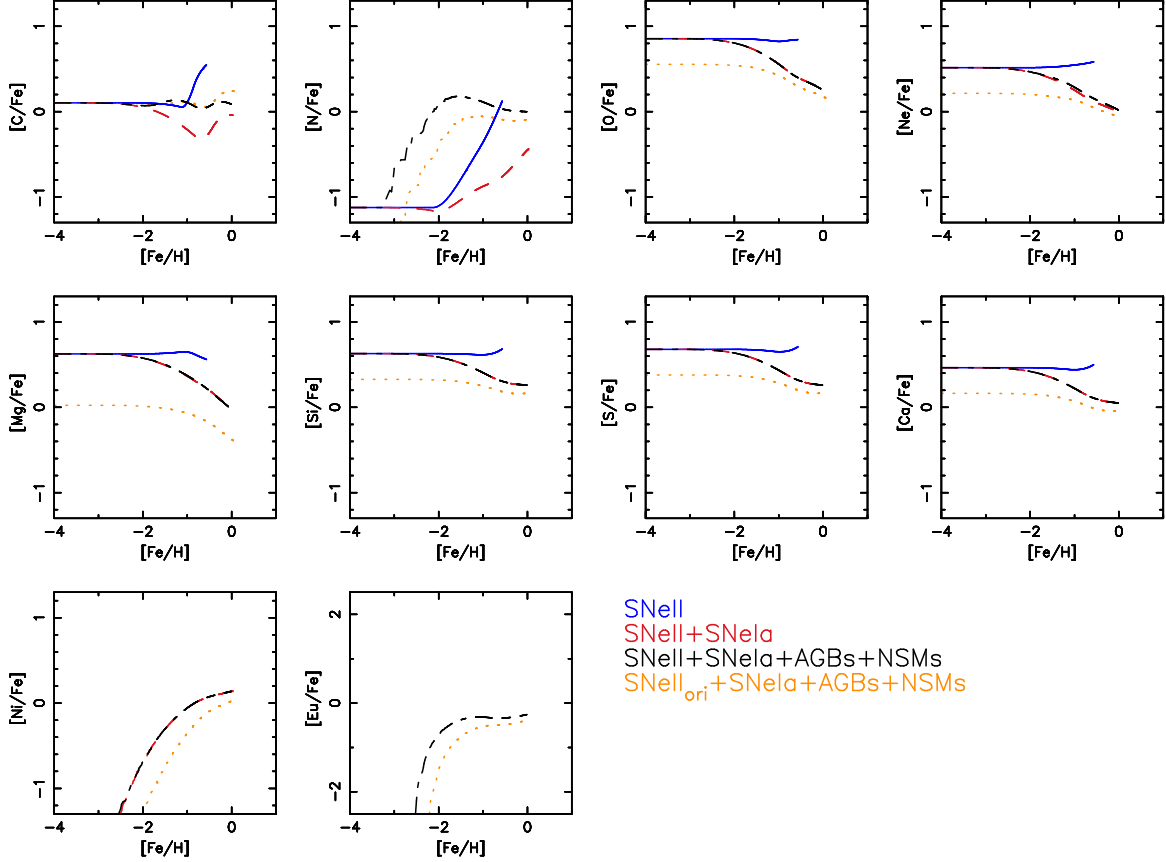


FIG. 26.— Same as figure 25, but Portinari et al. (1998)’s yields table is used for SNe II. The orange sequence is in the case that ad hoc factors for C, Mg, and Fe are not multiplied.

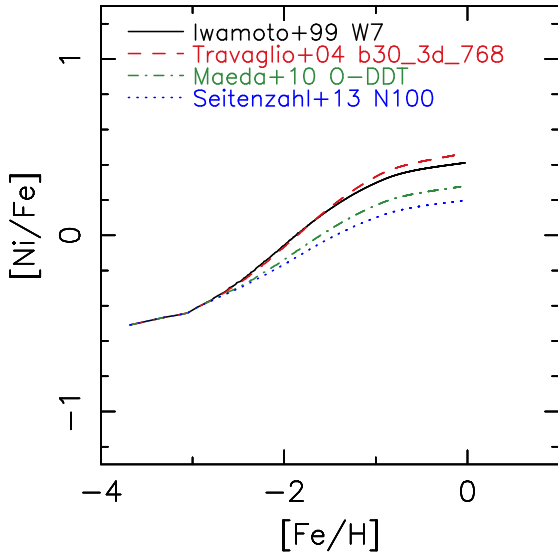


FIG. 27.— $[\text{Ni}/\text{Fe}]-[\text{Fe}/\text{H}]$ for different SN Ia yields. Blue, green, red and black sequences are results with yields of Iwamoto et al. (1999) (W7), Maeda et al. (2010) (W7), Maeda et al. (2010) (O-DDT), and Seitzzahl et al. (2013) (N100), respectively.

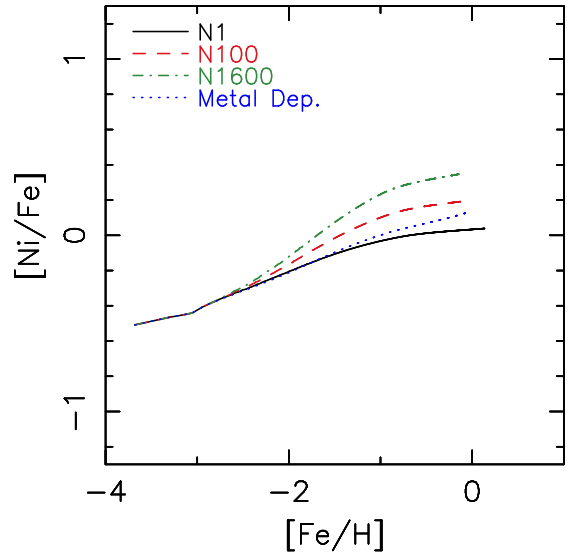


FIG. 28.— Same as figure 27, but for different ignition models of Seitzzahl et al. (2013). Blue, green and red sequences are results adopting N1, N100, and N1600, respectively. Black sequence is the result using our metallicity dependent yields with models N100, N100_Z0.5, N100_Z0.1, and N100_Z0.01.

velocity of the system is set to 200 km s^{-1} . Both gas and dark matter components initially follow the NFW profile in which the concentration parameter is 13 and spin parameter is 0.04. We adopt a truncation radius of 150 kpc. There are no particles outside of the truncation radius. The masses of gas and dark matter particles are

$8.5 \times 10^4 M_{\odot}$ and $1.6 \times 10^6 M_{\odot}$, respectively. The numbers of particles for gas and dark matter components are 10^6 and 3×10^6 . The softening lengths of gas and DM particles are set to 25 pc and 50 pc, respectively. We follow the system up to 5 Gyr.

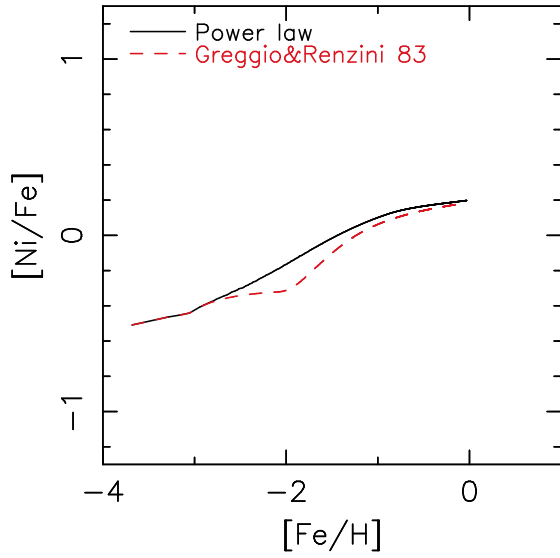


FIG. 29.— Same as figure 27, but for different DTD models. The yields of N100 in Seitzzahl et al. (2013) are adopted for SNe Ia. Red and black sequences are results with the binary synthesis model and the empirical power-law model, respectively.

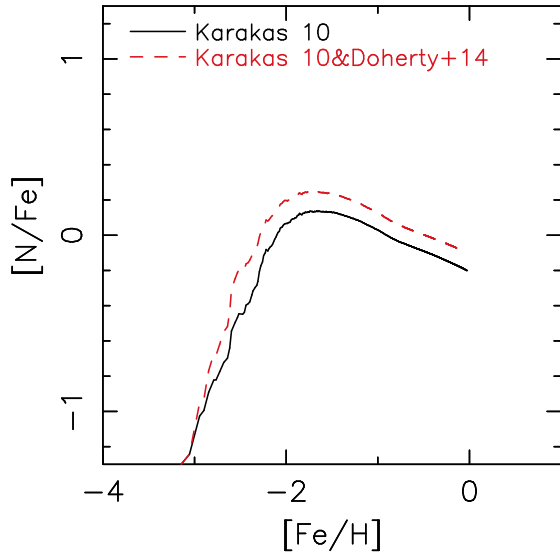


FIG. 30.— $[N/Fe]$ as a function of $[Fe/H]$.

7.2.2. Numerical techniques

We use **ASURA** (Saitoh et al. 2008, 2009) for simulations. We take into account the gravitational and hydrodynamical interactions, as well as the radiative cooling, star formation, and stellar feedback. The stellar feedback is dealt with by **CELib**. We use the reference models described in section 5.

The gravitational interactions are solved by using the tree method (Barnes & Hut 1986). The parallelization strategy of the tree method is the same as Makino (2004). In order to deal with different gravitational softening for different particle species, the symmetrized Plummer potential and its multipole expansion are used (Saitoh & Makino 2012). The opening angles for the ordinary three dimensional spaces and the gravitational softening lengths are 0.5 and 0.5, respectively.

The smoothed particle hydrodynamics (SPH) method

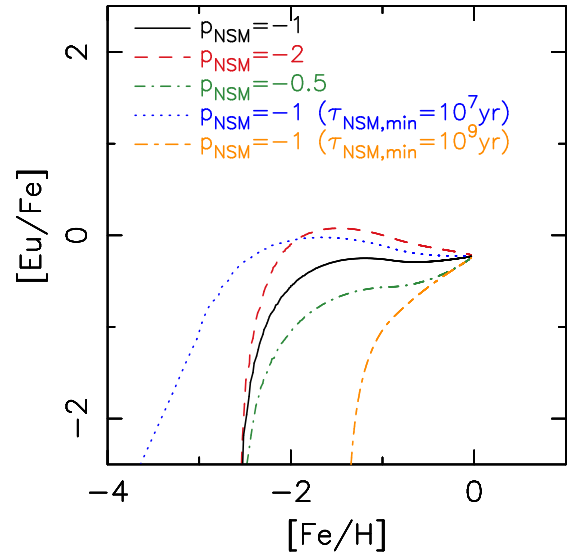


FIG. 31.— $[Eu/Fe]$ as a function of $[Fe/H]$. Three different power-law indexes, p_{NSM} , with $\tau_{NSM,min} = 100$ Myr are depicted as well as the models with the fiducial power law index $p_{NSM} = -1$ and different $\tau_{NSM,min}$ (10 Myr and 1 Gyr).

(Lucy 1977; Gingold & Monaghan 1977) is used to solve the evolution of the gas component. There are many variants. Here we use the density independent formulation of the SPH (DISPH) (Saitoh & Makino 2013) which adopts pressure instead of density for the fundamental smoothed quantity for the formulation. This formulation of SPH drastically improves the treatment of the contact discontinuities. In order to handle shocks, we use an artificial viscosity term with a functional form which is the same as that proposed in Monaghan (1997). The number of neighbor particles, N_{nb} , for each SPH particle is kept in $N_{nb} = 128 \pm 8$ and the Wendland C4 kernel (Wendland 1995) is used.

Time integration is carried out by the second-order scheme (see section A1 in Saitoh & Makino 2016). The individual, block time step method is used (McMillan 1986; Makino 1991). In order to accelerate the hydro simulation involving strong shocks and SNe, the FAST method (Saitoh & Makino 2010) is adopted for the time integration of SPH particles which allows SPH particles to have different time steps for the hydrodynamical and gravitational interactions. We also use the time-step limiter which keeps the time-step difference among neighboring particles small enough to follow strong shocks (Saitoh & Makino 2009).

The radiative cooling is dealt with using a cooling function generated by **Cloudy** (Ferland et al. 1998, 2013). The UV background heating of Haardt & Madau (2012) is taken into account. The self-shielding model of Rahmati et al. (2013), which reduces the intrusion of the UV background flux to the ISM, is also adopted. For radiative cooling, heating, and the self-shielding, we use the models at the redshift zero. Figure 32 shows the cooling/heating time obtained using our cooling/heating function. The red narrow region in $\rho > 10^{-3} n_H \text{ cm}^{-3}$ and $T \leq 10^4$ K corresponds to the equilibrium part of our cooling/heating function. Above this region, the radiative cooling dominates over the heating, whereas below this, the heating overcomes the cooling.

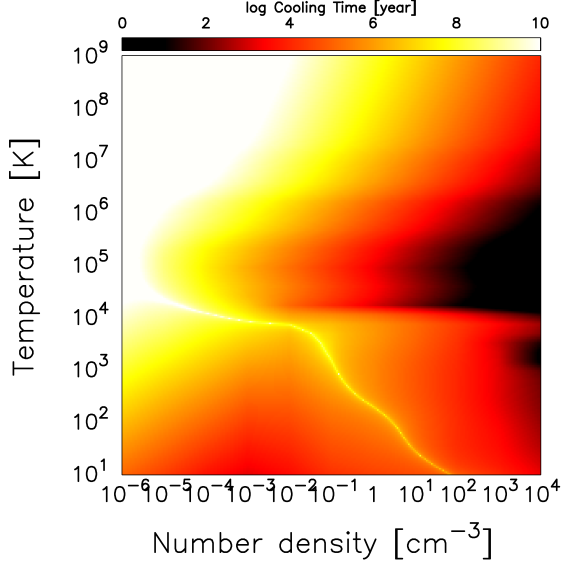


FIG. 32.— Cooling/Heating time in the density-temperature plane. The definition is $E_{\text{th}}(T)/\dot{E}_{\text{CH}}(\rho, T, Z)$, where $E_{\text{th}}(T)$ is the thermal energy at a given temperature and $\dot{E}_{\text{CH}}(\rho, T, Z)$ is the absolute value of the net energy change due to the radiative cooling and heating. The solar metallicity of Asplund et al. (2009) is assumed. The redshift is set to zero for this figure.

We set the high density ($> n_{\text{th}}$) and low temperature ($< T_{\text{th}}$) regions as the star forming regions. According to Saitoh et al. (2008, 2009), here we employ the following three conditions: (1) $\nabla \cdot v < 0$, (1) $n_{\text{th}} = 100 \text{ cc}$, and (1) $T_{\text{th}} = 100 \text{ K}$. When a gas particle satisfies all of the above conditions, the gas particle spawns a collisionless star particle with a mass of 1/3 of the initial gas particle mass. When the gas particle mass is less than 1/3 of the initial gas mass, the gas particle is converted into a star particle. The SSP approximation is applied to the star particle.

Here, we adopt the Chabrier IMF with a mass range of $0.1 M_{\odot} < M < 100 M_{\odot}$. Feedback energy from SNe II is calculated using adopted yields tables. We adopted the power law type DTD for SNe Ia. The power-law index is -1 and the normalization of Maoz & Mannucci (2012) is used. We used the cluster mode for the SNe Ia and regarded ten SNe Ia exploding at the same time. For the SNe Ia yields, we always use the N100 model in Seitzzahl et al. (2013). Two simulations do not use the AGB feedback while others take it into account. The time interval of this event, Δt_{AGB} , is set to 10^8 yr . NSMs are considered. Here we use $p_{\text{NSM}} = -1$ and $t_{\text{NSM, min}} = 10^8 \text{ yr}$.

As long as we use the SSP approximation and we put the released energy via thermal energy, the feedback from SNe II is inefficient and this is a long standing issue of galaxy formation (Dalla Vecchia & Schaye 2012). Therefore, we here implemented a stochastic model. This model is not the same as that proposed by Dalla Vecchia & Schaye (2012), while the philosophy is the same.

According to the argument in section 2 of Saitoh & Makino (2010), if we use all released energy from an SSP particle to the surrounding ISM, the typical temperature of a heated region is impossible to exceed that of the thermal instability region

($10^4 \text{ K} < T < 10^7 \text{ K}$) at the density of the typical star forming regions (see figure 32). The averaged increase of the internal energy surrounding exploded SNe II, U_{SN} , is

$$U_{\text{SN}} = \frac{\epsilon_{\text{SN}} m_* E_{\text{SN}}}{N_{\text{NB}} m_{\text{SPH}}} \quad (41)$$

$$\simeq 5 \times 10^{48} \times \frac{m_*}{N_{\text{NB}} m_{\text{SPH}}} [\text{ergs } M_{\odot}^{-1}] \quad (42)$$

$$\simeq \frac{2.5 \times 10^{15}}{N_{\text{NB}}} [\text{ergs } \text{g}^{-1}], \quad (43)$$

where ϵ_{SN} , m_* and m_{SPH} are the SNe II fraction per $1 M_{\odot}$ SSP particle, masses of star and gas particles, respectively. N_{NB} is the number of neighboring particles and the feedback energy is injected to the particles. From Eq (41) to Eq. (42), we assume that $\epsilon_{\text{SN}} = 0.005$ as a typical value⁹ with the standard IMF and the mass range of SNe II (see §4.8). In addition, we assume that the typical mass of a single star particle is identical to that of a single gas particle. When we assume an ideal gas with the specific heat ratio of 5/3 and the mean molecular weight is ~ 0.6 , Eq. (43) finally becomes

$$T_{\text{SN}} \sim 3.78 \times 10^5 (N_{\text{NB}}/32) [\text{K}]. \quad (44)$$

This clearly tells us that the thermal feedback is inefficient and this comes from the limitation of the numerical resolution that $m_{\text{gas}} \sim m_*$. For mesh codes, this problem does not occur intrinsically. However, in the mesh cases, there is no limitation for the gas temperature and thus, it is possible to reach unreasonably high temperatures by accident.

Here, for the feedback of SNe II, we adopt a probabilistic injection model so that the temperature of a heated region can reach a threshold temperature $T_{\text{SN, th}}$. First of all, the total energy release from SSP particles is

$$E_{\text{SN, tot}} = \sum_i \epsilon_{\text{SN}} E_{\text{SN}} m_{*, i}, \quad (45)$$

where the index i runs all star particles, and $m_{*, i}$ is the mass of the i -th SSP particle. We should construct a stochastic model which recovers this total energy even in a probabilistic manner. The temperature increase induced by the energy released from a SSP particle is written as

$$T_i = \frac{2\mu m_{\text{P}} \epsilon_{\text{SN}} E_{\text{SN}} m_{*, i}}{3k_{\text{B}} M_{\text{gas}, i}}, \quad (46)$$

where μ , m_{P} , and k_{B} are the mean molecular weight, the proton mass, and the Boltzmann constant, respectively, and $M_{\text{gas}, i}$ is the typical gas mass surrounding the SSP particles and it is typically $N_{\text{NB}} \times m_{\text{gas}}$, where m_{gas} indicates the mass of the gas particle. Here we introduce a new quantity $\mathcal{P}_{\text{SN}, i}$ and $\mathcal{P}_{\text{SN}, i} \equiv T_i/T_{\text{SN, th}}$. If we assume a sufficiently high $T_{\text{SN, th}}$, $\mathcal{P}_{\text{SN}, i} < 1$ and it can be regarded as a probability, as we show below. We use the acceptance-rejection method to evaluate the probability $\mathcal{P}_{\text{SN}, i}$:

$$E_{\text{SN}, i} = \begin{cases} E_{\text{SN, th}, i} & (A_{\mathcal{R}} \leq \mathcal{P}_{\text{SN}, i}), \\ 0 & (A_{\mathcal{R}} > \mathcal{P}_{\text{SN}, i}), \end{cases} \quad (47)$$

⁹ In Saitoh & Makino (2010), $\epsilon_{\text{SN}} = 0.0074$ is used. The values obtained here are slightly different from those in Saitoh & Makino (2010).

where $A_{\mathcal{R}}$ is a random real number in $[0, 1)$ and $E_{\text{SN,th}}$ is the energy where the averaged temperature reaches $T_{\text{SN,th}}$ and its functional form is

$$E_{\text{SN,th},i} = U_{\text{SN,th},i} M_{\text{gas},i}, \quad (48)$$

$$= \frac{3k_{\text{B}} T_{\text{SN,th}}}{2\mu m_{\text{p}}} M_{\text{gas},i}. \quad (49)$$

The total injection energy using this model is

$$E_{\text{SN,tot,new}} = \sum_i E_{\text{SN,th},i} \mathcal{P}_{\text{SN},i} \quad (50)$$

$$= \sum_i \frac{3k_{\text{B}} T_{\text{SN,th}}}{2\mu m_{\text{p}}} M_{\text{gas},i} T_i / T_{\text{SN,th}} \quad (51)$$

$$= \sum_i \epsilon_{\text{SN}} E_{\text{SN}m_{*},i} \quad (52)$$

This is the same as Eq. (45). In the following, we assume $T_{\text{SN,th}} = 5 \times 10^7$ K. Even though a failed case, $E_{\text{SN},i}$, the metal redistribution takes place in our model (see below). Only released energy is probabilistically redistributed.

When a star reaches the feedback time, the metallicity and energy released from the star are distributed to the surrounding ISM. Here we follow the implementation of Mosconi et al. (2001). We distribute the metals to the neighboring particles of the star particles of $N_{\text{nb}} = 128$ with the weight of the SPH kernel.

Metal diffusion is taken into account. Our implementation is based on that of Shen et al. (2010), in which the sub-grid turbulence model is used. The diffusion equation for k -th element we use is

$$\frac{dZ_{k,i}}{dt} = - \sum_j \frac{m_i}{(\rho_i + \rho_j)/2} \frac{4D_i D_j}{D_i + D_j} \frac{(Z_{k,i} - Z_{k,j})}{|r_{ij}|^2} \mathbf{r}_{ij} \cdot \nabla W_{ij} \quad (53)$$

where

$$\hat{S}_{ab,i} = \frac{1}{q_i} \sum_j U_j (v_{b,i} - v_{a,j}) \nabla_a W_{ij}, \quad (54)$$

$$S_{ab,i} = \frac{1}{2} (\hat{S}_{ab,i} + \hat{S}_{ba,i}) - \delta_{ab} \frac{1}{3} \text{Trace } \hat{S}_{ab,i}, \quad (55)$$

$$D_i = C_{\text{diff}} |S_{ab,i}| h_i^2. \quad (56)$$

Here, i and j are particle indexes, a and b denote x , y , and z directions, h is the kernel size, and δ_{ab} is the Kronecker's delta. W_{ij} is the kernel function. The diffusion coefficient, C_{diff} , depends on the structure of flow (typically ~ 0.1). It is set to 0.1 in this study. The mass exchange of k -th element using this equation has an antisymmetric form for particles i and j ;

$$\frac{dM_{k,i}}{dt} = m_i \frac{dZ_{k,i}}{dt} = -m_j \frac{dZ_{k,i}}{dt} = -\frac{dM_{k,i}}{dt}, \quad (57)$$

and thus this formulation can conserve the gas mass.

We carry out eleven runs with the different combinations of yields and models (with and without the Pop III IMF and metal mixing). The models are summarized in table 8.

7.2.3. General features of galaxies

Figure 33 displays the face-on and edge-on maps of the surface stellar density of runs A, B, C and D at $t = 5$ Gyr. When we compare the results with the yields tables of Nomoto et al. (2013) and Portinari et al. (1998) and without AGBs, i.e., runs A and B, we see that the stellar disk of run A is more compact and thicker than that of run B. The reason for this difference is that there is a relatively smaller amount of energy release from SNe II in run A compared to run B, as is expected from table 4. With this less efficient feedback, a dissipation-less nature is emphasized further.

To clarify the contribution of AGBs, we turn on the AGB feedback, which is mainly the mass recycling processes involving newly synthesized metals (runs C and D). We see from figure 33 that the stellar disk becomes larger in the radial direction. The return mass via AGBs enhances the late epoch star formation, resulting in the extended disk. Reflecting the fact that run C forms more stars, the contribution of AGBs is also more prominent, resulting in a larger disk compared to that in run D.

The impacts of the Pop III IMF (run E) and HNe (runs F and G) on galactic structures are found in figure 34. With the Pop III IMF and Nomoto et al. (2013)'s yields table, the released energy due to SNe II increases ~ 9 times larger than that without the Pop III IMF (see table 4). Thus there are striking effects on the galactic structure. When we use the Pop III IMF, the initial burst of star formation is suppressed significantly (we argue it below). In this case, the stellar disk becomes smaller because the initial burst induced by the Pop III feedback removes the gas component from the galaxy.

As is expected, the model with HNe ($f_{\text{HNe}} = 0.05$) is almost no difference from the run without HNe (run C). The model with HNe ($f_{\text{HNe}} = 0.5$), on the other hand, has large impacts on the galactic structure since the amount of the released energy with $f_{\text{HNe}} = 0.5$ is about four times larger than that with $f_{\text{HNe}} = 0$ (see table 4). This larger feedback energy results in the strong suppression of star formation and the removal of the log-angular momentum gas (e.g., Brook et al. 2012). The disk becomes much smaller compared to runs C and F.

Figure 35 shows the runs involving both HNe ($f_{\text{HNe}} = 0.05$ and 0.5) and the Pop III IMF, without and with metal mixing (runs H, I, J, and K). In the model with the metal mixing (run J), metals spread to the surrounding ISM and the radiative cooling becomes more efficient compared to that without mixing (run H). Thus, the star formation is significantly enhanced and the disk size becomes larger when the metal mixing is involved. In the models with $f_{\text{HNe}} = 0.5$ (runs I and K), the difference is hard to see because of their strong feedback. Note that these models are not models of a realistic galaxy formation through hierarchical mergers and hence, the contribution of metal mixing might be more complicated in the realistic model. We will study this in the future.

7.2.4. Star formation histories

Star formation rates (SFRs) as a function of time for all runs are shown in figure 36. All of the models shown the upper panel have strong initial bursts of star formation and then they rapidly quench. The duration of the initial starburst depends on the adopted yields tables and model

TABLE 8
MODELS FOR CHEMODYNAMICAL SIMULATIONS.

| | SNIi yields | SNIa yields | AGB yields | NSM yields | Pop III | Mixing |
|-------|--|------------------------------------|---|----------------------|---------|--------|
| Run A | Nomoto et al. (2013) ($f_{\text{HN}} = 0.0$) | Seitenzahl et al. (2013) (N100) | × | × | × | × |
| Run B | Portinari et al. (1998) ^a | Seitenzahl et al. (2013) (N100) | × | × | × | × |
| Run C | Nomoto et al. (2013) ($f_{\text{HN}} = 0.0$) | Seitenzahl et al. (2013) (N100) | Karakas (2010)+Doherty et al. (2014) | × | × | × |
| Run D | Portinari et al. (1998) ^a | Seitenzahl et al. (2013) (N100) | Karakas (2010) +Doherty et al. (2014) | × | × | × |
| Run E | Nomoto et al. (2013) ($f_{\text{HN}} = 0$) | Seitenzahl et al. (2013) (N100) | Karakas (2010)+Doherty et al. (2014) +Campbell & Lattanzio (2008) +Gil-Pons et al. (2013) | × | ✓ | × |
| Run F | Nomoto et al. (2013) ($f_{\text{HN}} = 0.05$) | Seitenzahl et al. (2013) (N100) | Karakas (2010)+Doherty et al. (2014) +Campbell & Lattanzio (2008) +Gil-Pons et al. (2013) | × | × | × |
| Run G | Nomoto et al. (2013) ($f_{\text{HN}} = 0.5$) | Seitenzahl et al. (2013) (N100) | Karakas (2010)+Doherty et al. (2014) +Campbell & Lattanzio (2008) +Gil-Pons et al. (2013) | × | × | × |
| Run H | Nomoto et al. (2013) ($f_{\text{HN}} = 0.05$) | Seitenzahl et al. (2013) (N100) | Karakas (2010)+Doherty et al. (2014) +Campbell & Lattanzio (2008) +Gil-Pons et al. (2013) | Wanajo et al. (2014) | ✓ | × |
| Run I | Nomoto et al. (2013) ($f_{\text{HN}} = 0.5$) | Seitenzahl et al. (2013) (N100) | Karakas (2010)+Doherty et al. (2014) +Campbell & Lattanzio (2008) +Gil-Pons et al. (2013) | Wanajo et al. (2014) | ✓ | × |
| Run J | Nomoto et al. (2013) ($f_{\text{HN}} = 0.05$) | Seitenzahl et al. (2013) (N100) | Karakas (2010)+Doherty et al. (2014) +Campbell & Lattanzio (2008) +Gil-Pons et al. (2013) | Wanajo et al. (2014) | ✓ | ✓ |
| Run K | Nomoto et al. (2013) ($f_{\text{HN}} = 0.5$) | Seitenzahl et al. (2013) (N100) | Karakas (2010)+Doherty et al. (2014) +Campbell & Lattanzio (2008) +Gil-Pons et al. (2013) | Wanajo et al. (2014) | ✓ | ✓ |

^a Note that the modifications for the yields of C, Mg, and Fe are applied. See also section 4.4.

parameters. Models whose released energy are large have shorter duration times: the duration time of the initial starburst of run B (D) is shorter than that of run A (C). We find the contribution of AGBs is easily seen in run C while not in run D. The reason why the run D does not show the enhancement of star formation at the late stage would be non-linear effects.

The bottom panel of figure 36 summarizes star formation histories with Pop III/HNe/metal mixing. We see that the initial burst of the star formation in the model with Pop III (run E) is strongly enhanced: this enhancement of star formation is due to a large amount of return mass and metals. When the released energy reaches the typical potential energy of the central region, the gas component leaks from the galaxy and thus the star formation quenches. This effect is also found in the models involving both Pop III and HNe (for instance, runs H and J). When we turn on the HN mode (runs F and G), the peaks of SFRs decrease. In the case with $f_{\text{HN}} = 0.5$, the star formation is strongly suppressed and the peak of the SFR becomes less than $20 M_{\odot} \text{ yr}^{-1}$, because of an extremely large release energy.

The metal mixing model enhances star formation in the whole time. The peak SFR increases from $140 M_{\odot} \text{ yr}^{-1}$ (run H, without mixing) to $170 M_{\odot} \text{ yr}^{-1}$ (run J, with mixing). The star formation in the late stage is kept a slightly higher SFR of $\sim 10 M_{\odot} \text{ yr}^{-1}$ if the metal mixing model is used. For the models with $f_{\text{HN}} = 0.5$, the contribution of metal mixing is hard to see.

7.2.5. Distributions of Elements

Figures 37 and 38 show $[X/\text{Fe}]$ - $[\text{Fe}/\text{H}]$ relations of nine elements for runs A, B, C, and D. We draw the median and 10% and 90% values as a function of $[\text{Fe}/\text{H}]$ in these figures. The evolution of $[X/\text{Fe}]$ in these figures is basically similar to those obtained by our one-zone models (see figures 25 and 26), although the metal redistribution scale is completely different. Initially, there are plateaus consisting of the SNe II yields. Then the values of $[X/\text{Fe}]$ become mixtures of SNe II, SNe Ia and AGBs yields. In the cases with AGBs in 3-dimensional simulations, the contribution of AGBs are more prominent compared to the one-zone models and they are not only limited in light elements. This effect is more prominent in the run with the Nomoto et al. (2013)'s yields table. This is because of the localization effect. The breaking points are shifted to +0.5 dex from those of one-zone models due to the rapid evolution of SFR (See figure 36). When the AGBs are taken into account, not only the median but also the scatter has changed. In particular in the low metal stars, the scatter increases because of the early AGBs (recall figure 20).

Figure 39 displays the $[X/\text{Fe}]$ - $[\text{Fe}/\text{H}]$ relations with the Pop III stars (run E) and with HNe (runs F and G). In these runs, the Nomoto et al. (2013)'s yields table is used. The impact of the Pop III stars on $[X/\text{Fe}]$ - $[\text{Fe}/\text{H}]$ relations are significant. The effect of the Pop III stars is observed up to $[\text{Fe}/\text{H}] = -2.5$ (Note that $Z_{\text{popIII}} = 10^{-5}$). With the Pop III stars, the amounts of $[\alpha/\text{Fe}]$ increase (see figure 6) and thus, $[\alpha/\text{Fe}]$ s at $[\text{Fe}/\text{H}] < -2.5$ shift upward. This behavior is comparable to that found in the one-zone model in figure 25. However, these rapid changes in $[X/\text{Fe}]$ - $[\text{Fe}/\text{H}]$ relations are not ob-

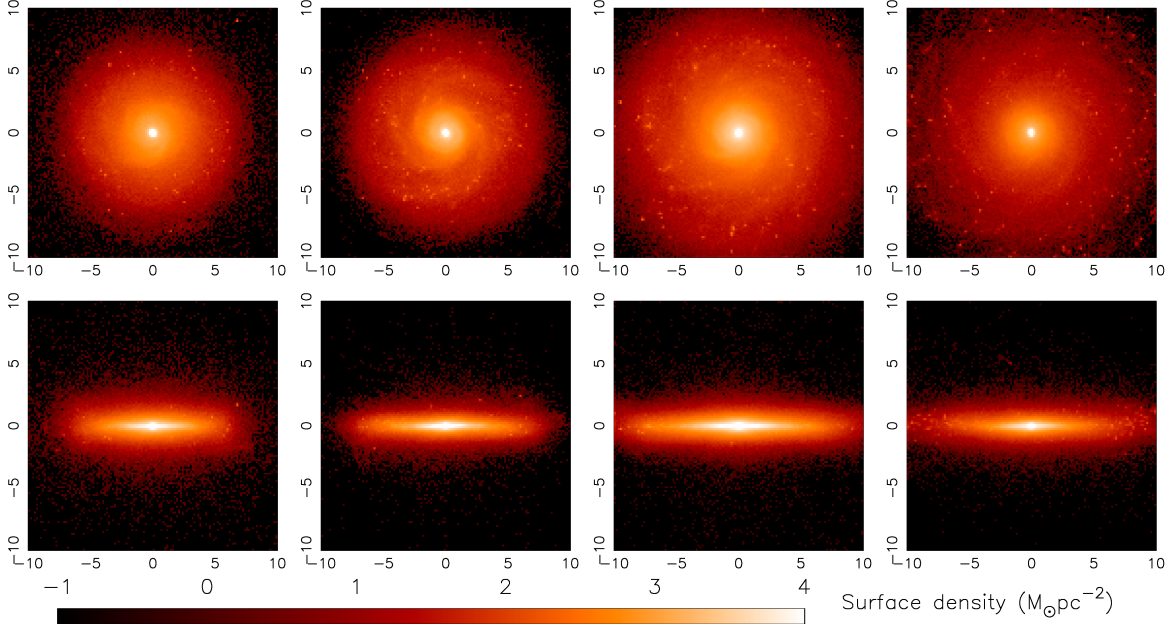


FIG. 33.— Face-on and edge-on maps of the stellar disks at 5 Gyr. From left to right columns, we show the maps of runs A, B, C, and D. Each panel shows the 20 kpc \times 20 kpc region.

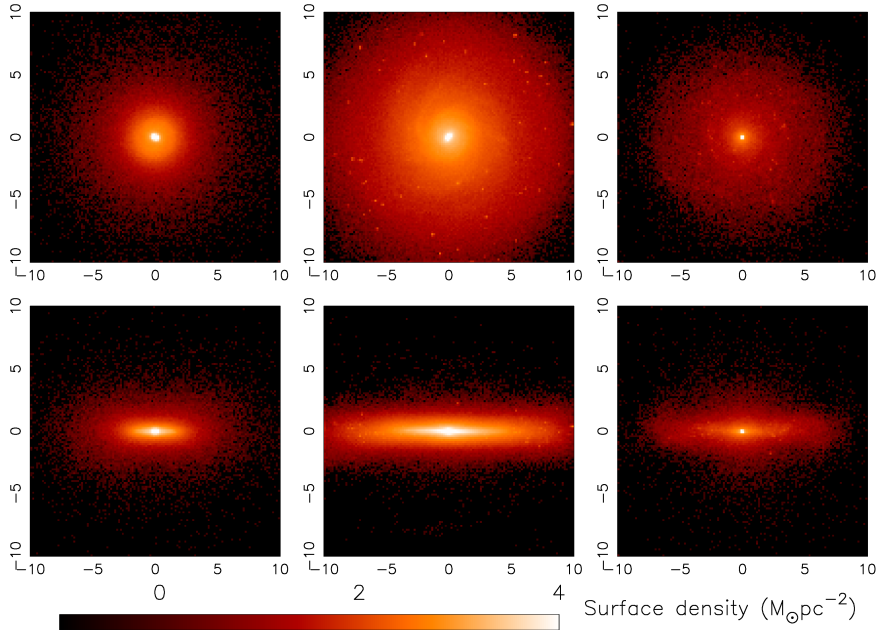


FIG. 34.— Same as figure 33, but for runs E, F, G.

servationally confirmed. We will see in the next figures, figures 40 and 41, that these gaps diminish/disappear when we adopt both the Pop III IMF and HNe.

The contributions of HNe to $[X/Fe]$ - $[Fe/H]$ relations can be seen as the timescale of the Fe pollution. Comparing $[X/Fe]$ - $[Fe/H]$ relations of runs F and G to those of run C, we find that the breaking points of $[X/Fe]$ - $[Fe/H]$ relations change from ~ -2 (run C) to ~ -1 (runs F and G). This is because the larger Fe yield of HNe (recall figure 7). In the case with $f_{\text{HN}} = 0.5$, the values of $[X/Fe]$ at SNe II plateaus decrease ~ 0.2 dex in $[O/Fe]$, $[Ne/Fe]$, $[Mg/Fe]$, $[Si/Fe]$, $[S/Fe]$ and $[Ca/Fe]$, while that increases ~ 0.2 dex in $[Ni/Fe]$. We can see similar tendencies in

the case with $f_{\text{HN}} = 0.05$, although the changes are much smaller than the case with $f_{\text{HN}} = 0.5$.

From figure 40, we can see the impact of metal mixing on the $[X/Fe]$ - $[Fe/H]$ relations. As is expected, the metal mixing greatly reduces scatters, which is identical to the result obtained in Shen et al. (2015). The transition points from the Pop III SNe to the normal SNe II and the breaking points of SNe II/Ia are slightly moved toward high $[Fe/H]$ regions when the mixing is adopted. This is because that the self-enrichment is more efficient in the run with the mixing model. With a small amount of HNe, the values of $[X/Fe]$ of the most metal-rich stars are almost identical to those without HNe (runs A and

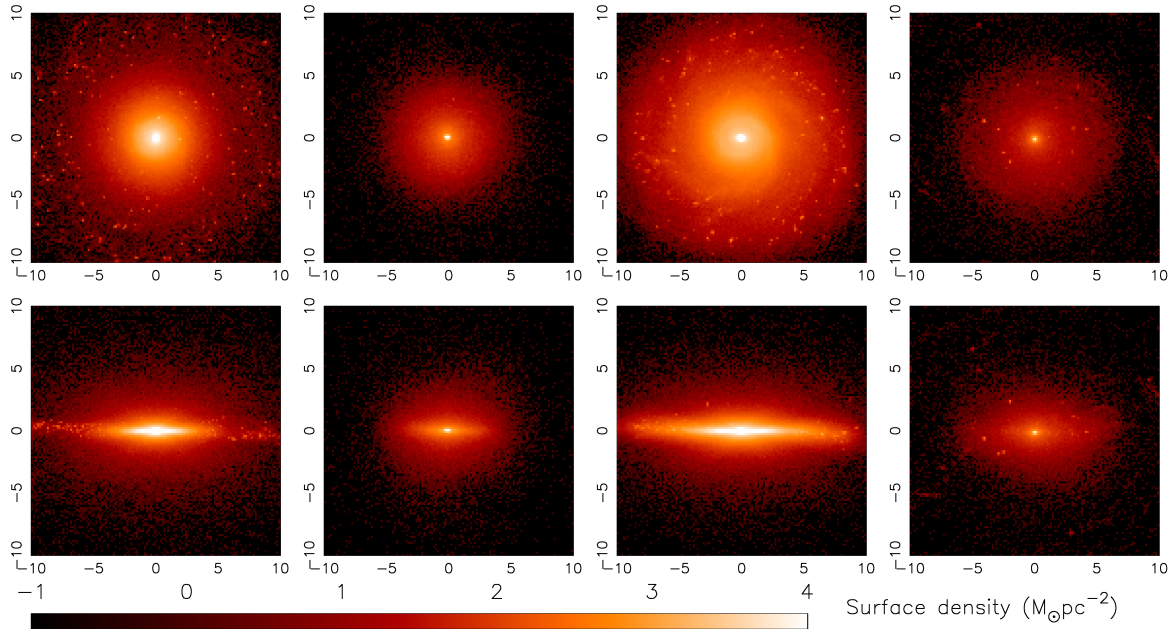


FIG. 35.— Same as figure 33, but for runs H, I, J, and K.

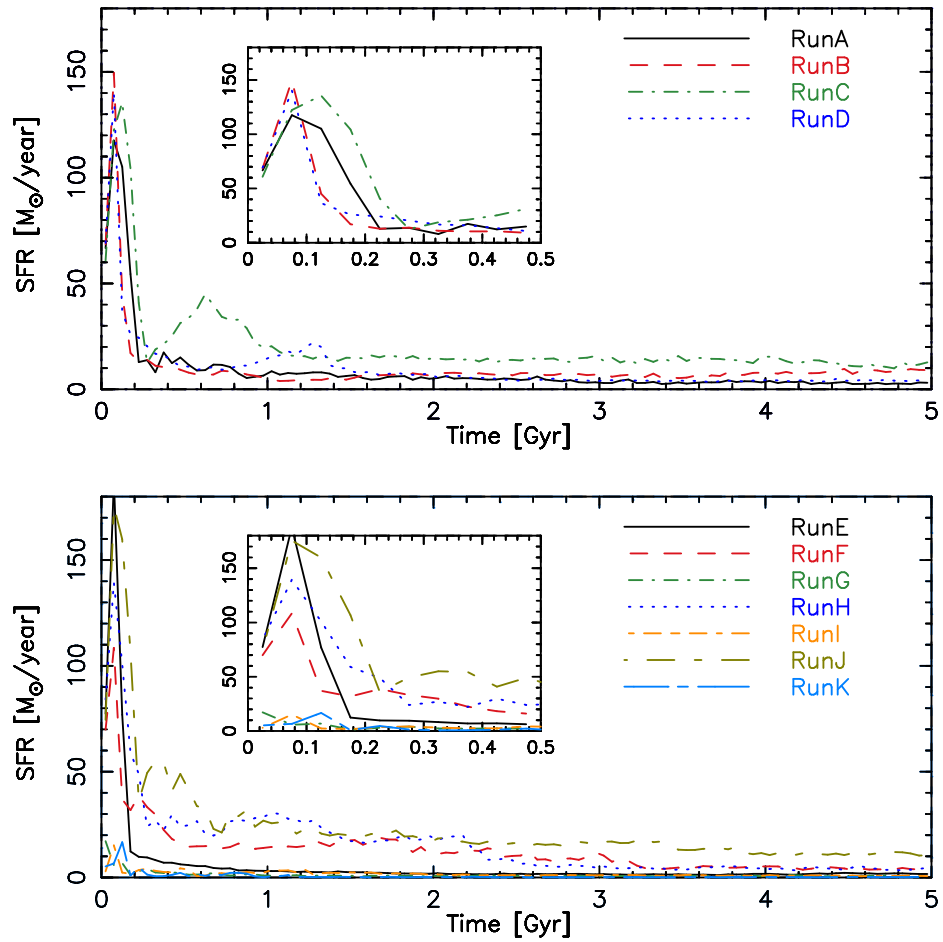


FIG. 36.— Star formation rate as a function of time. The close up of SFRs until $t = 0.5$ Gyr is shown in the inset.

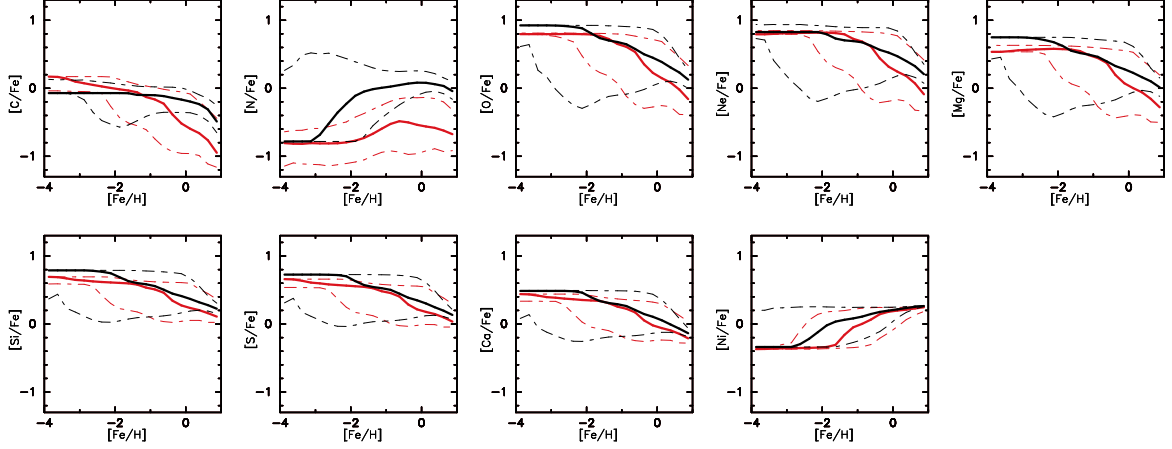


FIG. 37.— $[X/Fe]$ - $[Fe/H]$ relations of nine elements with Nomoto et al. (2013)’s yields table (for runs A and C). The data at 5 Gyr is used. Thick curves indicate the median value whereas thin dashed curves show the 10% and 90% values of each $[Fe/H]$ bin. Red and black curves are for runs A and C, respectively.

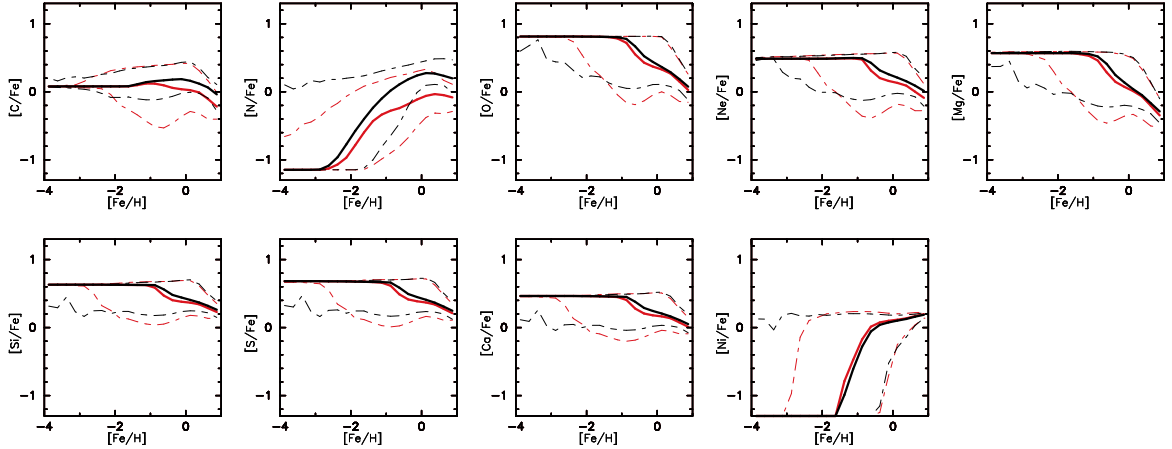


FIG. 38.— Same as figure 37, but with Portinari et al. (1998)’s yields table. Red and black curves are for runs B and D, respectively.

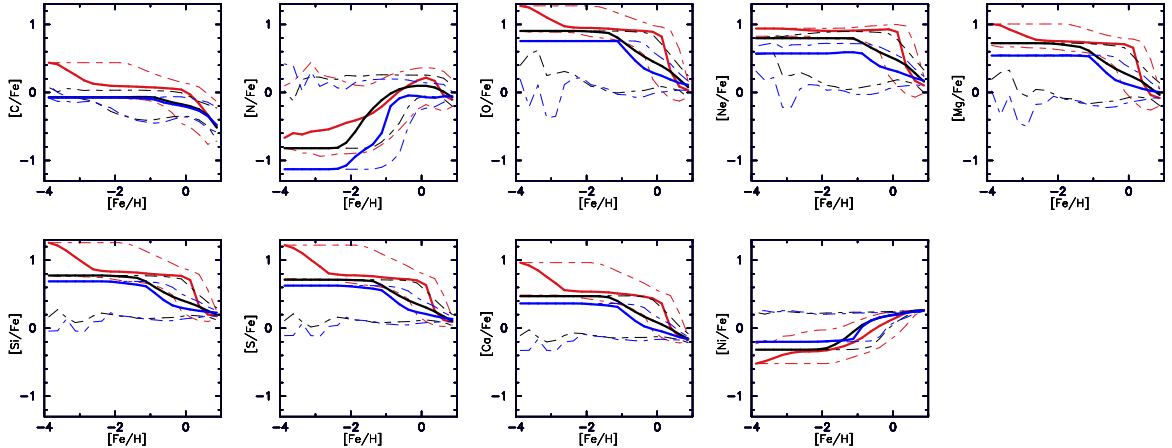


FIG. 39.— Same as figure 37, but with the Pop III IMF (run E), HNe ($f_{\text{HN}} = 0.05$: run F), and HNe ($f_{\text{HN}} = 0.5$: run G). For the Pop III IMF case, the corresponding yields table of Nomoto et al. (2013) is used. Red, black, and blue curves are for runs E, F, and G, respectively.

C).

Figure 41 shows the $[X/Fe]$ - Fe/H relations with $f_{HN} = 0.5$ and with/without the metal mixing. Although the star formation histories are completely different between cases with $f_{HN} = 0.5$ and $f_{HN} = 0.05$, the positions of breaking points with $f_{HN} = 0.5$ are comparable to those found in the case with $f_{HN} = 0.05$. The scatters in the run I are much wider than those in the run H. This would be that stars in the run I distribute farther from the galactic center and AGBs affect more in the outer fresh gas, due to the more energetic feedback. When the metal mixing turns on, the scatters become narrow (run K). The black curves (run K) have sudden rises at $Z > 0.5$. Their values of $[X/Fe]$ s are identical to those expected by yields of SNe II. Hence, the contribution of SNe II dominates in stars at the metallicity range. This might be an accidental case.

The $[Eu/Fe]$ - $[Fe/H]$ relations are shown in figures 40 and 41. The median values of $[Eu/Fe]$ rise at $[Fe/H] \sim -1$ and they saturate $[Eu/Fe] \sim -0.2$ at $[Fe/H] \sim +1$. These evolution tracks are expected by one-zone simulations. While we adopted $p_{NSM} = -1$ and $\tau_{NSM, \min} = 10^8$ yr, the evolution tracks on the plane in figures 40 and 41 are similar to the case with $p_{NSM} = -1$ and $\tau_{NSM, \min} = 10^9$ yr in figure 31. This is because star-formation time scales in our three-dimensional simulations are shorter than those used in one-zone simulations. As a result, stars with low- Z and high $[Eu/Fe]$ are hard to see in our model, whereas stars with $[Eu/Fe] > 0$ and $[Fe/H] < -3$ are found in observations (see Suda et al. 2011).

The gap between our results and observations originate from the models we used in this paper. Our models are too simple to express detailed distributions of chemical composition generated by rare events. We expect that the scatter will revert in a cosmological simulation because of its hierarchical nature. We will investigate the evolution of r-process elements in the cosmological context elsewhere in the near future.

8. SUMMARY AND FUTURE PROSPECTS

We developed a software library for the chemical evolution simulation of galaxy formation, named ‘‘CELlib’’. This library adopts the SSP approximation and, under this approximation, it provides the return mass of each element and released energy from an SSP particle depending on feedback type. How these quantities are redistributed is left to the user’s simulation code.

All of the necessary data, such as IMFs, stellar lifetime data, and yields are implemented in CELlib, as well as reference feedback models. The data is obtained from the literature. Most functions are selectable at the run-time, and hence it is easy to compare the contribution of each model. The use of CELlib is easy if users follow the standard way because it consists of a limited number of APIs. Since CELlib is a simple software library, it is easy to carry out simulations of chemical evolution even for a beginner of this field. Using internal functions, it is also possible to construct one’s favorite model of chemical evolution.

As demonstrations of CELlib, we showed the results of our simple one-zone models and three-dimensional chemodynamical simulations in a dark matter halo. The yields for SNe II have a large impact on chemical evolution, as is pointed out in previous studies. When we

compare the results with the yields table of Nomoto et al. (2013) and that of Portinari et al. (1998) with slight modifications, these two results are almost comparable except for the light elements, C and N. On the other hand, if we use the original yields of Portinari et al. (1998), the $[X/Fe]$ - $[Fe/H]$ relations become inconsistent with other results.

SNe Ia affect the position of the breaking point of the plateau. A different yields table gives different final amounts of metals released by SNe Ia. This implies that we need to be careful with models and yields of SNe Ia when we compare results with observations.

AGBs affect the evolutions of relatively light elements, such as C and N. These effects can be seen in both one-zone and three-dimensional simulations. The feedback from AGBs is sometimes not taken into account even in current simulations of galaxy formation. However, they cannot be ignored since they are very common in the ISM.

We provide the community with this library (<https://bitbucket.org/tsaitoh/celib>) and it is also archived on Zenodo (10.5281/zenodo.190830). We believe that this library will accelerate the understanding of galaxy formation from the perspective of chemical evolution.

Following are the future prospects of this library.

- Further flexibility would be necessary for IMF shapes. It is more convenient if each stellar particle can have its own IMF and mass range. The importance of the top-heavy IMF in galaxy formation is well understood (e.g., Baugh et al. 2005; Nagashima et al. 2005).
- Further extension of yields tables is desirable. For instance, recently, the NuGrid collaboration published their yields tables (Pignatari et al. 2016) which are based on the MESA and GENEC codes (Paxton et al. 2011; Eggenberger et al. 2008). The published yields are $Z = 0.01$ and 0.02 . We will take their yields when all data is published. In the current version of this library, all yields tables are obtained from models without stellar rotations. It is pointed out that stellar rotation changes yields (e.g., Heger et al. 2000; Meynet & Maeder 2002). The effect of the rotating zero metal stars was studied in Kobayashi et al. (2011a) and they showed these stars have significant effects on $[C/Fe]$ - $[Fe/H]$ and $[N/Fe]$ - $[Fe/H]$ relations and a moderate effect on the $[O/Fe]$ - $[Fe/H]$ relation.
- Further sophisticated treatment of the chemical enrichment might be important. Strictly speaking, the yield of each element depends on the abundance of other elements. However, the current formulation implemented on CELlib ignores this effect. As such, the Q_{ij} formalism has been proposed (Talbot & Arnett 1973; Ferrini et al. 1992; Portinari et al. 1998). With and without this formulation, there might be certain differences in chemical enrichment (Martínez-Serrano et al. 2008). Note, however, that they assumed the solar proportions, which is not ideal for understanding the Q_{ij} formulation.

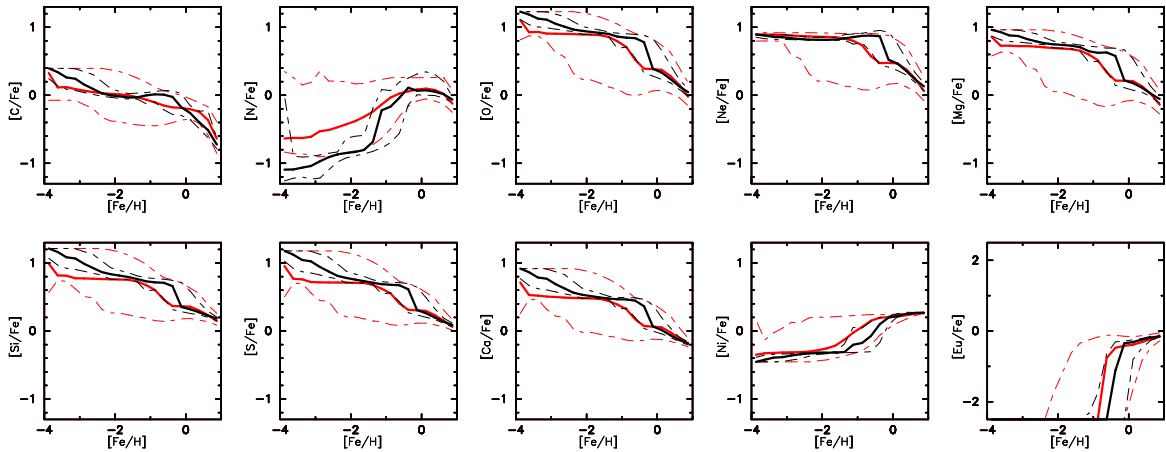


FIG. 40.— Same as figure 37, but with HNe ($f_{\text{HN}} = 0.05$), the Pop III IMF and NSMs. Red and black curves are for runs H and J, respectively. Run J adopts the metal diffusion model of Eq (53).

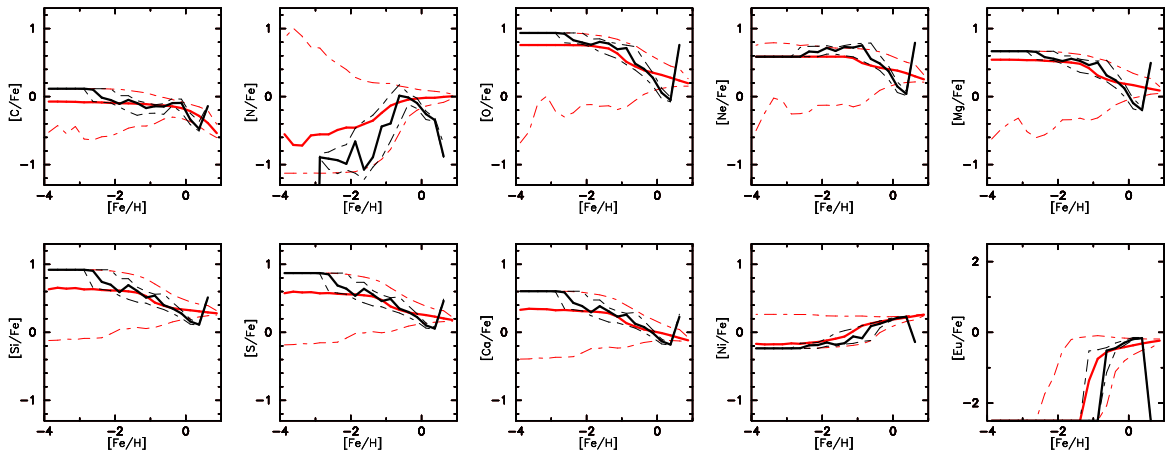


FIG. 41.— Same as figure 37, but with HNe ($f_{\text{HN}} = 0.5$), the Pop III IMF and NSMs. Red and black curves are for runs I and K, respectively. Run K adopts the metal diffusion model of Eq (53).

- Further extension of available yields and isotopes are important to connect studies of galaxy formation and planet formation. In the current version of CELib, the distributions of isotopes are not considered. It is also important to distinguish the contributions from different types of feedback. Generally, only the data of long lived isotopes are provided.¹⁰ This data is sufficient for galactic chemical evolution studies. However, in the case that the distributions of the short lived isotopes are important, the current treatment of the isotopes is insufficient. For example, it is pointed out that the radio isotope of aluminum, ^{26}Al , is abundant during the early age of the solar system (e.g., Lee et al. 1976; Russell et al. 1996; Jacobsen et al. 2008; Bouvier & Wadhwa 2010; Larsen et al. 2011) and the decay heat of ^{26}Al , whose half-time period is 0.72 Myr, is considered to be a primary source of the Earth’s early evolution (e.g., Urey 1955; Castillo-Rogez et al. 2009; Elkins-Tanton et al. 2011), as well as these of ^{235}U , ^{238}U , ^{232}Th , and ^{40}K . To deal with the decays of

all of radioactive isotopes is unrealistic. At least it is necessary to deal with the decays of some of the important radioactive isotopes to understand the formation history of stars and planets from the perspective of galactic chemodynamical simulations.

It is certain that star-by-star simulations are the next breakthrough of galaxy formation simulation since there are an enormous amount of evidence that massive stars have crucial impacts on the galaxy formation and evolution. In some first star and first galaxy simulations, Pop III stars are dealt with discrete stars sampled from a Pop III IMF instead of using the SSP approximation (e.g., Wise & Abel 2008; Greif et al. 2010; Wise et al. 2012, 2014; Ritter et al. 2015; O’Shea et al. 2015; Smith et al. 2015) or its formation is directly followed (e.g., Hirano et al. 2014; Hosokawa et al. 2016). While such treatment of stars is beyond the original scope of CELib, the all necessary data used for the chemical evolution of star-by-star simulations have been implemented. Hence, CELib provides APIs which can be used by star-by-star simulation (see appendix B).

¹⁰ The yields tables of SNe Ia usually provides not only the amounts of stable elements but also those of short-lived elements.

The author thanks the anonymous referee who gave constructive and helpful comments that improved this

study. The author also thanks Yutaka Hirai, Takashi Okamoto, Junichi Baba, Daisuke Kawata, Ko Nakamura, Takuma Suda and Yutaka Katsuta who gave important input for this study. A part of numerical simulations was carried out on the Cray XC30 system in the Center for Computational Astrophysics at the National Astronom-

ical Observatory of Japan. This work is supported by a Grant-in-Aid for Scientific Research (26707007) of Japan Society for the Promotion of Science and Strategic Programs for Innovative Research of the Ministry of Education, Culture, Sports, Science and Technology (SPIRE).

APPENDIX

A. APPLICATION INTERFACES

Here we describe the major functions of CELib. All available functions are defined in `CELib.h`.

A.1. *Initialize CELib*

This library is initialized by just calling this function;

```
void CELibInit(void);
```

When this function is called, the IMF and its mass range are fixed. Then under these conditions, the IMF weighted yields of the adopted yield tables are computed. The smoothed lifetime functions and necessary data for reference feedback models are also computed.

This function should be called at the beginning of a simulation using this library. Every model's parameters are fixed at this time. If a user wants to use different model parameters, the user needs to call this function again after resetting new parameters.

A.2. *Get event time*

With reference feedback models, the user can easily obtain event times. In order to obtain an event time of an SSP particle, the user has to use the following function;

```
double CELibGetNextEventTime(struct CELibStructNextEventTimeInput Input, const int Type);
```

This function returns the event time of a target event in units of year.

This function requires two arguments. The first argument is a structure defined in `CELib.h` and the definition of it is

```
struct CELibStructNextEventTimeInput{
    double R; // A random real number in [0,1)
    double InitialMass_in_Msun; // An initial mass of the target SSP particle
    // in units of the solar mass
    double Metallicity; // A metallicity of the target SSP particle
    int Count; // A counter for a target event
    // This is used in SNe Ia/AGBs/NSMs
    // Count should start zero.
};
```

The second argument of this reference API is used to specify the feedback type. Feedback types are defined as `enum` and the user should select one out of four;

```
enum {
    CELibFeedbackType_SNII,
    CELibFeedbackType_SNIa,
    CELibFeedbackType_AGB,
    CELibFeedbackType_NSM,
    CELibFeedbackType_Number,
};
```

For example, we consider a case in which the user wants to obtain the explosion time of SNe II using the reference model. In this case, the user has to call the reference API like this;

```
struct CELibStructNextEventTimeInput Input = {
    .R = A_r, // A random real number in [0,1)
    .InitialMass_in_Msun = M_ssp, // The initial mass of the target SSP particle
    .Metallicity = Z_ssp, // The metallicity of the target SSP particle
};
double t_snII = CELibGetNextEventTime(Input, CELibFeedbackType_SNII);
```

`Count` is not used to obtain the feedback time of SNe II and thus it is ignored in this case. The return value `t_snII` is the explosion time which follows figures 17 or 18. If the simulation time is t_{sim} , the feedback event takes place at $t_{\text{sim}} + t_{\text{snII}}$.

A.3. Get released masses of metals and energy

The released masses of metals and energy are also easily obtained by using a reference API. When the time in a simulation reaches the event time, we need to call the following function;

```
struct CELibStructFeedbackOutput
    CELibGetFeedback(struct CELibStructFeedbackInput Input, const int Type);
```

The first argument is the structure defined in `CELib.h` and it holds all the necessary data to evaluate the feedback event. The structure is

```
struct CELibStructFeedbackInput{
    double Mass;                // The mass of the target SSP particle in simulation unit
    double Metallicity;        // The metallicity of the target SSP particle
    double MassConversionFactor; // A factor to convert Elements[] from
                                // the simulation mass unit to the solar mass
    double *Elements;          // The pointer to the array of elements for
                                // the target SSP particle in the simulation mass unit
    int Count;                 // A counter of the target event
};
```

The second argument is the type of feedback and it is the same as that used to obtain the feedback time.

The results are loaded to a structure whose type is `struct CELibStructFeedbackOutput`. The definition of it is as follows:

```
struct CELibStructFeedbackOutput{
    double Energy;              // The released energy in units of erg
    double EjectaMass;         // The ejecta mass in units of the solar mass
    double RemnantMass;        // The remnant mass in units of the solar mass
    double Elements[CELibYield_Number]; // The mass of released metals in units of the solar mass
};
```

Note that `CELibYield_Number` is defined in `CELib.h` and is thirteen in the current version.

For example, we show the way to obtain the results of SNe II feedback. First the user needs to put all necessary data to the structure `struct CELibStructFeedbackInput` and then call `CELibGetFeedback` with `CELibFeedbackType_SNII`.

```
struct CELibStructFeedbackInput Input = {
    .Mass = M_ssp,
    .Metallicity = Z_ssp,
    .MassConversionFactor = Mass_solar_mass/Mass_sim_unit,
    .Elements = Elements_ssp,
}
struct CELibStructFeedbackOutput SNII =
    CELibGetFeedback(Input,CELibFeedbackType_SNII);
```

Units of energy and mass in SNII are erg for energy and M_{\odot} . If the simulation units are different from these units, the user needs to convert them into the simulation units.

A.4. Select models and set model parameters

All of the control parameters are stored in the structure `struct CELibStructRunParameters`. `CELib` prepares a structure `CELibRunParameters` and it is used to manage this library. The fiducial model is the same as that used in §7.2 as run F (see table 8). When the values in `CELibRunParameters` are changed and the initializer is called, `CELib` recomputes all data and thus a new simulation is ready to start.

B. APPLICATION INTERFACES FOR STAR BY A STAR SIMULATION

`CELib` provides APIs for star-by-star simulations. So far, `CELib` supports only feedback from massive stars.

B.1. Get event time for star by star simulations

The function shown below is used in order to get the event time of a star:

```
double CELibGetNextEventTimeStarbyStar
    (struct CELibStructNextEventTimeStarbyStarInput Input, const int Type);
```

This function returns the lifetime of a star in units of year, referring the lifetime tables built in §4.2. The structure of the first argument, which is also defined in `CELib.h`, is as follows:

```

struct CELibStructNextEventTimeStarbyStarInput{
    double InitialMass_in_Msun; // Mass of the star
    double Metallicity;        // Metallicity of the star, Z
};

```

The second argument is the type of feedback. Although only feedback from massive stars is supported in the current version of CELib, we prepare this argument for the future extension. In the current version, `Type` should be `CELibFeedbackType_SNII`.

B.2. Get released masses of metals and energy for star by star simulations

Mass, metals, and energy released from a single event can be obtained by using the following function:

```

struct CELibStructFeedbackStarbyStarOutput
    CELibGetFeedbackStarbyStar(struct CELibStructFeedbackStarbyStarInput Input, const int Type);

```

Again, the first argument is the structure defined in `CELib.h`. This structure holds all the necessary data to evaluate the feedback event. Here is the members of the structure:

```

struct CELibStructFeedbackStarbyStarInput{
    double Mass; // Mass of the star in simulation unit.
    double Metallicity; // Metallicity of the star Z
    double MassConversionFactor; // A factor to convert Elements[] from
    // the simulation mass unit to Msun.
    double *Elements; // Star particle's elements composition in simulation unit.
};

```

The second argument used in `CELibStructFeedbackStarbyStarOutput` is the feedback type and is also reserved for the future extension.

The results are stored to a structure, `struct CELibStructFeedbackStarbyStarOutput`, of which definition is

```

struct CELibStructFeedbackStarbyStarOutput{
    double Energy; // The released energy in units of erg
    double EjectaMass; // The ejecta mass in units of the solar mass
    double RemnantMass; // The remnant mass in units of the solar mass
    double Elements[CELibYield_Number]; // The mass of released metals in units of the solar mass
};

```

REFERENCES

- Abel, T., Bryan, G. L., & Norman, M. L. 2002, *Science*, 295, 93
- Anders, E., & Grevesse, N. 1989, *Geochim. Cosmochim. Acta*, 53, 197
- Arrighi, M., Trager, S. C., Somerville, R. S., & Gibson, B. K. 2010, *MNRAS*, 402, 173
- Asplund, M., Grevesse, N., Sauval, A. J., & Scott, P. 2009, *ARA&A*, 47, 481
- Barkat, Z., Rakavy, G., & Sack, N. 1967, *Physical Review Letters*, 18, 379
- Barnes, J., & Hut, P. 1986, *Nature*, 324, 446
- Baugh, C. M., Lacey, C. G., Frenk, C. S., et al. 2005, *MNRAS*, 356, 1191
- Becker, S. A. 1979, PhD thesis, Illinois Univ., Urbana-Champaign.
- Bell, E. F., & de Jong, R. S. 2001, *ApJ*, 550, 212
- Bouvier, A., & Wadhwa, M. 2010, *Nature Geoscience*, 3, 637
- Bromm, V. 2013, *Reports on Progress in Physics*, 76, 112901
- Bromm, V., Coppi, P. S., & Larson, R. B. 2002, *ApJ*, 564, 23
- Brook, C. B., Stinson, G., Gibson, B. K., et al. 2012, *MNRAS*, 419, 771
- . 2014, *MNRAS*, 443, 3809
- Burris, D. L., Pilachowski, C. A., Armandroff, T. E., et al. 2000, *ApJ*, 544, 302
- Campbell, S. W., & Lattanzio, J. C. 2008, *A&A*, 490, 769
- Cappellaro, E., Turatto, M., Tsvetkov, D. Y., et al. 1997, *A&A*, 322, 431
- Castillo-Rogez, J., Johnson, T. V., Lee, M. H., et al. 2009, *Icarus*, 204, 658
- Chabrier, G. 2003, *PASP*, 115, 763
- Chiappini, C., Matteucci, F., & Romano, D. 2001, *ApJ*, 554, 1044
- Conroy, C., & van Dokkum, P. G. 2012, *ApJ*, 760, 71
- Conroy, C., van Dokkum, P. G., & Kravtsov, A. 2015, *ApJ*, 803, 77
- Cora, S. A. 2006, *MNRAS*, 368, 1540
- Côté, B., O'Shea, B. W., Ritter, C., Herwig, F., & Venn, K. A. 2016, *ArXiv e-prints*, arXiv:1604.07824
- Dalla Vecchia, C., & Schaye, J. 2012, *MNRAS*, 426, 140
- De Silva, G. M., Freeman, K. C., Bland-Hawthorn, J., et al. 2015, *MNRAS*, 449, 2604
- Doherty, C. L., Gil-Pons, P., Lau, H. H. B., Lattanzio, J. C., & Siess, L. 2014, *MNRAS*, 437, 195
- Dominik, M., Belczynski, K., Fryer, C., et al. 2012, *ApJ*, 759, 52
- Eggenberger, P., Meynet, G., Maeder, A., et al. 2008, *Ap&SS*, 316, 43
- Eichler, D., Livio, M., Piran, T., & Schramm, D. N. 1989, *Nature*, 340, 126
- Elkins-Tanton, L. T., Weiss, B. P., & Zuber, M. T. 2011, *Earth and Planetary Science Letters*, 305, 1
- Ferland, G. J., Korista, K. T., Verner, D. A., et al. 1998, *PASP*, 110, 761
- Ferland, G. J., Porter, R. L., van Hoof, P. A. M., et al. 2013, *Revista Mexicana de Astronomia y Astrofisica*, 49, 137
- Ferrini, F., Matteucci, F., Pardi, C., & Penco, U. 1992, *ApJ*, 387, 138
- Few, C. G., Courty, S., Gibson, B. K., et al. 2012, *MNRAS*, 424, L11
- Few, C. G., Courty, S., Gibson, B. K., Michel-Dansac, L., & Calura, F. 2014, *MNRAS*, 444, 3845
- François, P., Matteucci, F., Cayrel, R., et al. 2004, *A&A*, 421, 613
- Fraser, M., Casey, A. R., Gilmore, G., Heger, A., & Chan, C. 2015, *ArXiv e-prints*, arXiv:1511.03428
- Freiburghaus, C., Rosswog, S., & Thielemann, F.-K. 1999, *ApJL*, 525, L121
- Frost, C. A., & Lattanzio, J. C. 1996, *ApJ*, 473, 383
- Gargiulo, I. D., Cora, S. A., Padilla, N. D., et al. 2015, *MNRAS*, 446, 3820
- Gibson, B. K. 1997, *MNRAS*, 290, 471
- Gibson, B. K., Loewenstein, M., & Mushotzky, R. F. 1997, *MNRAS*, 290, 623
- Gil-Pons, P., Doherty, C. L., Lau, H., et al. 2013, *A&A*, 557, A106

- Gilmore, G., Randich, S., Asplund, M., et al. 2012, *The Messenger*, 147, 25
- Gingold, R. A., & Monaghan, J. J. 1977, *MNRAS*, 181, 375
- Glover, S. 2013, in *Astrophysics and Space Science Library*, Vol. 396, *The First Galaxies*, ed. T. Wiklund, B. Mobasher, & V. Bromm, 103
- Goriely, S., Bauswein, A., & Janka, H.-T. 2011, *ApJL*, 738, L32
- Gratton, R. G., Carretta, E., Claudi, R., Lucatello, S., & Barbieri, M. 2003, *A&A*, 404, 187
- Greggio, L. 2005, *A&A*, 441, 1055
- Greggio, L., & Renzini, A. 1983, *A&A*, 118, 217
- Greif, T. H., Glover, S. C. O., Bromm, V., & Klessen, R. S. 2009, *MNRAS*, 392, 1381
- 2010, *ApJ*, 716, 510
- Greif, T. H., Springel, V., White, S. D. M., et al. 2011, *ApJ*, 737, 75
- Grevesse, N., & Sauval, A. J. 1998, *Space Sci. Rev.*, 85, 161
- Guetta, D., & Della Valle, M. 2007, *ApJL*, 657, L73
- Haardt, F., & Madau, P. 2012, *ApJ*, 746, 125
- Hachisu, I., Kato, M., & Nomoto, K. 1996, *ApJL*, 470, L97
- 1999, *ApJ*, 522, 487
- Hartwig, T., Bromm, V., Klessen, R. S., & Glover, S. C. O. 2015, *MNRAS*, 447, 3892
- Hayden, M. R., Bovy, J., Holtzman, J. A., et al. 2015, *ApJ*, 808, 132
- Hayward, C. C., Narayanan, D., Kereš, D., et al. 2013, *MNRAS*, 428, 2529
- Heger, A., Langer, N., & Woosley, S. E. 2000, *ApJ*, 528, 368
- Hirai, Y., Ishimaru, Y., Saitoh, T. R., et al. 2015, *ApJ*, 814, 41
- Hirano, S., Hosokawa, T., Yoshida, N., Omukai, K., & Yorke, H. W. 2015, *MNRAS*, 448, 568
- Hirano, S., Hosokawa, T., Yoshida, N., et al. 2014, *ApJ*, 781, 60
- Hirschi, R., Meynet, G., & Maeder, A. 2005, *A&A*, 433, 1013
- Hosokawa, T., Hirano, S., Kuiper, R., et al. 2016, *ApJ*, 824, 119
- Hosokawa, T., Omukai, K., Yoshida, N., & Yorke, H. W. 2011, *Science*, 334, 1250
- Hurley, J. R., Pols, O. R., & Tout, C. A. 2000, *MNRAS*, 315, 543
- Iben, Jr., I., & Tutukov, A. V. 1984, *ApJS*, 54, 335
- Ishimaru, Y., Wanajo, S., & Prantzos, N. 2015, *ApJL*, 804, L35
- Iwamoto, K., Brachwitz, F., Nomoto, K., et al. 1999, *ApJS*, 125, 439
- Izzard, R. G., Tout, C. A., Karakas, A. I., & Pols, O. R. 2004, *MNRAS*, 350, 407
- Jacobson, B., Yin, Q.-z., Moynier, F., et al. 2008, *Earth and Planetary Science Letters*, 272, 353
- Kalirai, J. S., Anderson, J., Dotter, A., et al. 2013, *ApJ*, 763, 110
- Karakas, A., & Lattanzio, J. C. 2007, *PASA*, 24, 103
- Karakas, A. I. 2010, *MNRAS*, 403, 1413
- Karakas, A. I., & Lattanzio, J. C. 2014, *PASA*, 31, 30
- Kawata, D., & Gibson, B. K. 2003, *MNRAS*, 340, 908
- Kennicutt, Jr., R. C. 1983, *ApJ*, 272, 54
- Kobayashi, C., Karakas, A. I., & Umeda, H. 2011a, *MNRAS*, 414, 3231
- Kobayashi, C., & Nakasato, N. 2011, *ApJ*, 729, 16
- Kobayashi, C., Tominaga, N., & Nomoto, K. 2011b, *ApJL*, 730, L14
- Kobayashi, C., Tsujimoto, T., & Nomoto, K. 2000, *ApJ*, 539, 26
- Kobayashi, C., Tsujimoto, T., Nomoto, K., Hachisu, I., & Kato, M. 1998, *ApJL*, 503, L155
- Kobayashi, C., Umeda, H., Nomoto, K., Tominaga, N., & Ohkubo, T. 2006, *ApJ*, 653, 1145
- Komiya, Y., Suda, T., Minaguchi, H., et al. 2007, *ApJ*, 658, 367
- Kroupa, P. 2001, *MNRAS*, 322, 231
- Kroupa, P., Tout, C. A., & Gilmore, G. 1993, *MNRAS*, 262, 545
- Larsen, K. K., Trinquier, A., Paton, C., et al. 2011, *ApJL*, 735, L37
- Lattimer, J. M., Mackie, F., Ravenhall, D. G., & Schramm, D. N. 1977, *ApJ*, 213, 225
- Lattimer, J. M., & Schramm, D. N. 1976, *ApJ*, 210, 549
- Lee, T., Papanastassiou, D. A., & Wasserburg, G. J. 1976, *Geophys. Res. Lett.*, 3, 41
- Leitherer, C., Ekström, S., Meynet, G., et al. 2014, *ApJS*, 212, 14
- Leitherer, C., Ortiz Otálvaro, P. A., Bresolin, F., et al. 2010, *ApJS*, 189, 309
- Leitherer, C., Schaerer, D., Goldader, J. D., et al. 1999, *ApJS*, 123, 3
- Lorimer, D. R. 2008, *Living Reviews in Relativity*, 11, 8
- Lucy, L. B. 1977, *AJ*, 82, 1013
- Maeda, K., Röpke, F. K., Fink, M., et al. 2010, *ApJ*, 712, 624
- Maeder, A. 1992, *A&A*, 264, 105
- Maeder, A., & Meynet, G. 1989, *A&A*, 210, 155
- Majewski, S. R., APOGEE Team, & APOGEE-2 Team. 2016, *Astronomische Nachrichten*, 337, 863
- Makino, J. 1991, *PASJ*, 43, 859
- 2004, *PASJ*, 56, 521
- Maaz, D., & Mannucci, F. 2012, *PASA*, 29, 447
- Maaz, D., Mannucci, F., & Nelemans, G. 2014, *ARA&A*, 52, 107
- Marigo, P. 2001, *A&A*, 370, 194
- Martínez-Serrano, F. J., Serna, A., Domínguez-Tenreiro, R., & Mollá, M. 2008, *MNRAS*, 388, 39
- Matteucci, F. 2003, *The Chemical Evolution of the Galaxy*
- Matteucci, F., Romano, D., Arcones, A., Korobkin, O., & Rosswog, S. 2014, *MNRAS*, 438, 2177
- Matteucci, F., Spitoni, E., Recchi, S., & Valiante, R. 2009, *A&A*, 501, 531
- McMillan, S. L. W. 1986, in *Lecture Notes in Physics*, Berlin Springer Verlag, Vol. 267, *The Use of Supercomputers in Stellar Dynamics*, ed. P. Hut & S. L. W. McMillan, 156–
- Meynet, G., & Maeder, A. 2002, *A&A*, 390, 561
- Miller, G. E., & Scalo, J. M. 1979, *ApJS*, 41, 513
- Monaghan, J. J. 1997, *Journal of Computational Physics*, 136, 298
- Mosconi, M. B., Tissera, P. B., Lambas, D. G., & Cora, S. A. 2001, *MNRAS*, 325, 34
- Nagashima, M., Lacey, C. G., Baugh, C. M., Frenk, C. S., & Cole, S. 2005, *MNRAS*, 358, 1247
- Navarro, J. F., Frenk, C. S., & White, S. D. M. 1997, *ApJ*, 490, 493
- Nomoto, K. 1982, *ApJ*, 253, 798
- Nomoto, K., Iwamoto, K., Nakasato, N., et al. 1997, *Nuclear Physics A*, 621, 467
- Nomoto, K., Kobayashi, C., & Tominaga, N. 2013, *ARA&A*, 51, 457
- Nomoto, K., Tominaga, N., Umeda, H., Kobayashi, C., & Maeda, K. 2006, *Nuclear Physics A*, 777, 424
- Okamoto, T., Eke, V. R., Frenk, C. S., & Jenkins, A. 2005, *MNRAS*, 363, 1299
- Okamoto, T., Nemmen, R. S., & Bower, R. G. 2008, *MNRAS*, 385, 161
- Omukai, K., Hosokawa, T., & Yoshida, N. 2010, *ApJ*, 722, 1793
- Omukai, K., & Nishi, R. 1998, *ApJ*, 508, 141
- O’Shea, B. W., Wise, J. H., Xu, H., & Norman, M. L. 2015, *ApJL*, 807, L12
- Parrent, J., Friesen, B., & Parthasarathy, M. 2014, *Ap&SS*, 351, 1
- Paxton, B., Bildsten, L., Dotter, A., et al. 2011, *ApJS*, 192, 3
- Perret, V., Renaud, F., Epinat, B., et al. 2014, *A&A*, 562, A1
- Pignatari, M., Herwig, F., Hirschi, R., et al. 2016, *ApJS*, 225, 24
- Planck Collaboration, Ade, P. A. R., Aghanim, N., et al. 2014, *A&A*, 571, A16
- Podsiadlowski, P., Mazzali, P. A., Nomoto, K., Lazzati, D., & Cappellaro, E. 2004, *ApJL*, 607, L17
- Portinari, L., Chiosi, C., & Bressan, A. 1998, *A&A*, 334, 505
- Prantzos, N. 2008, in *EAS Publications Series*, Vol. 32, *EAS Publications Series*, ed. C. Charbonnel & J.-P. Zahn, 311–356
- Rahimi, A., Kawata, D., Allende Prieto, C., et al. 2011, *MNRAS*, 415, 1469
- Rahmati, A., Pawlik, A. H., Raicevic, M., & Schaye, J. 2013, *MNRAS*, 430, 2427
- Raiteri, C. M., Villata, M., & Navarro, J. F. 1996, *A&A*, 315, 105
- Rauscher, T., Heger, A., Hoffman, R. D., & Woosley, S. E. 2002, *ApJ*, 576, 323
- Ritter, J. S., Sluder, A., Safranek-Shrader, C., Milosavljević, M., & Bromm, V. 2015, *MNRAS*, 451, 1190
- Romano, D., Chiappini, C., Matteucci, F., & Tosi, M. 2005, *A&A*, 430, 491
- Romano, D., Karakas, A. I., Tosi, M., & Matteucci, F. 2010, *A&A*, 522, A32
- Rood, R. T. 1972, *ApJ*, 177, 681
- Russell, S. S., Srinivasan, G., Huss, G. R., Wasserburg, G. J., & MacPherson, G. J. 1996, *Science*, 273, 757
- Saitoh, T. R., Daisaka, H., Kokubo, E., et al. 2008, *PASJ*, 60, 667
- 2009, *PASJ*, 61, 481
- Saitoh, T. R., & Makino, J. 2009, *ApJL*, 697, L99
- 2010, *PASJ*, 62, 301
- 2012, *New Astronomy*, 17, 76
- 2013, *ApJ*, 768, 44
- 2016, *ApJ*, 823, 144
- Salpeter, E. E. 1955, *ApJ*, 121, 161
- Scannapieco, C., Tissera, P. B., White, S. D. M., & Springel, V. 2005, *MNRAS*, 364, 552
- Schaerer, D. 2002, *A&A*, 382, 28
- Schaller, G., Schaerer, D., Meynet, G., & Maeder, A. 1992, *A&AS*, 96, 269
- Seitzzahl, I. R., Ciaraldi-Schoolmann, F., Röpke, F. K., et al. 2013, *MNRAS*, 429, 1156
- Shen, S., Cooke, R. J., Ramirez-Ruiz, E., et al. 2015, *ApJ*, 807, 115
- Shen, S., Wadsley, J., & Stinson, G. 2010, *MNRAS*, 407, 1581
- Smith, B. D., Wise, J. H., O’Shea, B. W., Norman, M. L., & Khochfar, S. 2015, *MNRAS*, 452, 2822
- Snaith, O. N., Bailin, J., Gibson, B. K., et al. 2016, *MNRAS*, 456, 3119
- Spiniello, C., Trager, S., Koopmans, L. V. E., & Conroy, C. 2014, *MNRAS*, 438, 1483
- Stacy, A., Bromm, V., & Lee, A. T. 2016, *MNRAS*, 462, 1307

- Steinmetz, M., & Mueller, E. 1994, *A&A*, 281, L97
Steinmetz, M., & Muller, E. 1995, *MNRAS*, 276, 549
Steinmetz, M., Zwitter, T., Siebert, A., et al. 2006, *AJ*, 132, 1645
Stritzinger, M., Mazzali, P. A., Sollerman, J., & Benetti, S. 2006, *A&A*, 460, 793
Suda, T., Yamada, S., Katsuta, Y., et al. 2011, *MNRAS*, 412, 843
Suda, T., Komiya, Y., Yamada, S., et al. 2013, *MNRAS*, 432, 46
Susa, H., Hasegawa, K., & Tominaga, N. 2014, *ApJ*, 792, 32
Talbot, Jr., R. J., & Arnett, W. D. 1973, *ApJ*, 186, 51
Timmes, F. X., Woosley, S. E., & Weaver, T. A. 1995, *ApJS*, 98, 617
Tinsley, B. M. 1980, *Fund. Cosmic Phys.*, 5, 287
Tolstoy, E., Hill, V., & Tosi, M. 2009, *ARA&A*, 47, 371
Totani, T., Morokuma, T., Oda, T., Doi, M., & Yasuda, N. 2008, *PASJ*, 60, 1327
Travaglio, C., Hillebrandt, W., Reinecke, M., & Thielemann, F.-K. 2004, *A&A*, 425, 1029
Umeda, H., & Nomoto, K. 2002, *ApJ*, 565, 385
—. 2005, *ApJ*, 619, 427
Urey, H. C. 1955, *Proceedings of the National Academy of Science*, 41, 127
van den Bergh, S., & Tammann, G. A. 1991, *ARA&A*, 29, 363
van den Hoek, L. B., & Groenewegen, M. A. T. 1997, *A&AS*, 123, 305
Vassiliadis, E., & Wood, P. R. 1993, *ApJ*, 413, 641
Vázquez, G. A., & Leitherer, C. 2005, *ApJ*, 621, 695
Vogelsberger, M., Genel, S., Sijacki, D., et al. 2013, *MNRAS*, 436, 3031
Wanajo, S., Janka, H.-T., & Müller, B. 2011, *ApJL*, 726, L15
Wanajo, S., Sekiguchi, Y., Nishimura, N., et al. 2014, *ApJL*, 789, L39
Webbink, R. F. 1984, *ApJ*, 277, 355
Wendland, H. 1995, *Advances in computational Mathematics*, 4, 389
Whelan, J., & Iben, Jr., I. 1973, *ApJ*, 186, 1007
Wiersma, R. P. C., Schaye, J., & Smith, B. D. 2009a, *MNRAS*, 393, 99
Wiersma, R. P. C., Schaye, J., Theuns, T., Dalla Vecchia, C., & Tornatore, L. 2009b, *MNRAS*, 399, 574
Wise, J. H., & Abel, T. 2008, *ApJ*, 685, 40
Wise, J. H., Demchenko, V. G., Halicek, M. T., et al. 2014, *MNRAS*, 442, 2560
Wise, J. H., Turk, M. J., Norman, M. L., & Abel, T. 2012, *ApJ*, 745, 50
Woosley, S. E., & Weaver, T. A. 1995, *ApJS*, 101, 181
Yates, R. M., Henriques, B., Thomas, P. A., et al. 2013, *MNRAS*, 435, 3500
Yoshida, N., Omukai, K., & Hernquist, L. 2008, *Science*, 321, 669